Study of the diffusive properties of extracellular matrix gels used in 3D cultures

Roland Galgoczy

Tesi doctoral

Programa de Doctorat de Biomedicina

Study of the diffusive properties of extracellular matrix gels used in 3D cultures

Presentada per,

Roland Galgoczy

Per optar al grau de doctor

Treball dirigit pel Dr. Jordi Alcaraz

I per la Dra. Noemi Reguart

A la Unitat de Biofísica i Bioenginyeria

Del departament de Ciències Fisiològiques I;

Facultat de Medicina, Universitat de Barcelona.

To my family

"The saddest aspect of life right now is

that science gathers knowledge

faster than society gathers wisdom."

Isaac Asimov

Acknowledgements

"Ladies and Gentlemen, honored daughters,

while Mr. Kim by virtue of his youth and naiveté

has fallen prey to the inexplicable need for human contact,

let me assure you that my research will go on uninterrupted,

and that social relationships will continue to baffle and repulse me.

Thank you!"

Sheldon Lee Cooper, B.S, M.S, M.A, PhD, Sc.D

fictional character

A PhD thesis is a long journey, and the company you keep is strongly correlated with the probability of success (Would have Frodo made it without Sam and his other fellows? I doubt it.). During my thesis I have worked alongside people that made my journey not only possible, but also pleasant and rewarding. In gratitude to those people, I would like to address a few words.

To Jordi, my thesis director. thank you for believing in me and providing me with the confidence I needed to always find solutions when none seemed to arise. You have contributed tremendously to my formation as an investigator and I believe you were the best mentor I could have asked for. To Noemi, my codirector, thank you for all the help that you have provided me and all the means (scientific and economic) that you invested in my formation.

To all the people that make the UBB a state-of-the-art functioning unit: to Daniel for being a great leader and for caring for each and every member of the lab, to Ramon for always providing useful comments and advice, to Miguel Angel for his ability to build anything out of anything. Also, to Domenec and his group for their enjoyable presence.

To our collaborators: to Isabel for the help she provided and her dedication to our project, to Francesc for his patience and perseverance with finite diffusion models.

Also, to Dra. Eulalia Rius for providing access to the fluorescent plate reader, and to Dr. Maria Calvo for providing access to FRAP and useful advice.
To my fellow lab rats and faithful friends: to Roberto for his cheerful presence and his heroic ability to endure my bad jokes, to Alicia and Marta Puig for their patience while teaching me about the secrets of laboratory work, to Tomas for teaching me how to use the home-made AFM and for his insightful theories about everything, to Juanjo for always being supportive and helpful, to Noelia for the colorful discussion topics during lunch time and for being a sore loser at board games, to Valentina for her concern towards everyone, to Nonaka for lifting the overall mood of the lab, to Esther for her passion towards science, to Maeba, Ignasi and Adriana. I would also like to thank everyone in Dr. Xavier Trepat's and Dr. Pere Roca's groups for their insightful comments during our scientific meetings.
To those who have abandoned the lab: to Theodora for introducing me to the dark arts of AFM, to Rocio for the energy she invested in everyone else's work, to Adai for being an exceptional colleague, even from afar, to Jessica for that little bit of insanity that makes science fun, to Ion, to Isaac for sharing in the secrets of oxygen tension measurements, to Ferranda for her insight on plate reader measurements, to Elena, Marta Torres, German and Blai.
I would also like to thank Dr. Javier Buceta and his group (Oriol and Marc) for guiding my first steps in the world of science.

On a more personal level, I would like to thank my parents for the effort and sacrifice they made so that I could have a good education, for giving me the possibility to do something useful in life. To my brother for being supportive and for always carrying in a League of Legends game. To Irina for giving me the strength and the courage I need (Also for washing dishes and cooking for several months while this thesis was being written). I would also like to thank my mother-in-law for not protesting too much before letting me marry Irina.
I would also like to thank my friends, Victor, Nacho, Gabriela and César who have helped me maintain my mental sanity.

Contents

Preface

The roots of biological investigation can be traced back to Hippocrates (460 BC – 370 BC) and Aristotle (384 BC – 322 BC). Even in ancient times, people have tried to explain the functioning of the human body and the rules by which we were designed. Scientific investigation in biology peaked with the invention of the Petri dish and the culturing of cells. The ability to isolate cells and observe their behavior to a variety of stimuli was a giant step that has brought us closer to understanding the rules that govern our bodies.

The human body is built in a three dimensional architecture. Cells are joined with other cells in a 3D mesh. This mesh, the extracellular matrix (ECM), nurtures the cells, it provides communication between them, mechanical strength, it is the very scaffold where cells build organs and the human body itself. Accordingly, the use of a 3D architecture has been sough for cell culturing, a place where cells are no longer deprived of their beloved environment. A new step has been taken towards mimicking *in vivo* conditions. Moreover, the scaffold consists not only of a 3D space, but also of the natural mesh components that cells find inside the body. These 3D scaffolds based on natural ECM components have been used in a variety of studies over the years and have grown to be very successful. However, there are still characteristics of three dimensional cell cultures that are poorly understood and are currently limiting their applicability. Among them, it is worth noting the little understanding of the molecular transport within ECM scaffolds, and to what extent this transport approaches that of tissues. These unknowns include diffusion timescales, viscosity, tortuosity and 3D cell culture design rules in general. As an attempt to bridge this gap, the aim of my thesis was to study the characteristics of the most common three dimensional extracellular matrix cell cultures in terms of diffusion. This has been achieved by two different ways. First, the effective diffusion coefficients of soluble factors within the scaffolds were assessed using micro- and macroscopic techniques. Second, the oxygen partial pressure

has been measured and the subsequent diffusivity, cell oxygen consumption rates and proliferation were assessed.

The work presented here is the product of 3 and a half years of research at the Biophysics and Bioengineering Unit of the department of Physiological Sciences I at the School of Medicine of the University of Barcelona. The thesis is divided into 6 Chapters. In Chapter 1, the Introduction, I summarize the state-of-the-art of cell cultures and the extracellular matrix. Also, I review the importance of diffusion within three-dimensional cell cultures based on native ECM components, the shortcomings of 3D cultures in terms of diffusion and finally the current quantification techniques. The aims of the different studies are presented in Chapter 2. Chapter 3 is dedicated to the methodological techniques that were applied during this work. Chapter 4 represents the main core of the thesis and it contains all the results. Two lines of research work are described, one that considers diffusion of small fluorescent tracer molecules and another that consists of measuring oxygen pressure within the 3D cultures. In Chapter 5 I discuss on the main findings, the implications and the insights for designing relevant 3D cultures in terms of diffusion. Finally, in Chapter 6 I present the conclusion of the thesis. I also provide additional information through the Appendices A-C. In Appendix A I describe the preparation protocols of the gels, while in Appendix B I expose the most significant source codes that I used. It should be noted that most of the work presented here has been published or is in advanced revision state.

Abstract

The extracellular matrix (ECM) hinders diffusion in both tissues and hydrogels used in 3D cultures. However, how geometric and non-geometric ECM properties contribute to diffusion hindrance remains poorly understood. To address this question, the effective diffusivity D of FITC-dextrans with molecular weight (M_r, 4-70 kDa) spanning the physiological range of signaling factors was measured in a panel of acellular ECM gels with an optical macroscopic assay. Gels included reconstituted basement membrane/Matrigel, fibrin and type I collagen, and exhibited an average pore size much larger than any dextran size. Unexpectedly, a decay of D with M_r following a power-law with an exponent that matched that predicted by the Stokes-Einstein law in all gels ($D \sim M_r^{-1/3}$, r^2=0.99) was observed, revealing that hindered diffusion is dominated by non-geometric viscous factors. This law predicted that Matrigel and fibrin exhibited similar viscosities, which was confirmed with microrheology measurements by atomic force microscopy. Moreover, gels with the lowest D exhibited diffusion hindrance comparable to the extreme physiologic hindrance of brain tissue, which has a typical pore size much smaller than ECM gels. In contrast, diffusion hindrance in sparse (≤ 1 mg/ml) gels was very weak and below any reported tissue diffusivity data. These observations reveal a major role for the enhanced viscosity of the extracellular space in regulating the passive transport in both 3D culture and tissues, and indicate that dense ECM gels (≥ 3mg/ml) are suitable tissue surrogates in terms of macromolecular diffusion.

Another major limitation of 3D cultures in terms of transport arises from the fact that it remains unknown to what extent current 3D culture protocols provide physiologic oxygen tension conditions. To address this limitation, oxygen tension was measured within the acellular or cellularized ECM gels with A549 cells, and analyzed in terms of oxygen diffusion and consumption. Oxygen diffusivity in acellular gels was up to 40% smaller than that of water, and the lower values were observed in the denser gels. In 3D cultures, physiologic oxygen tension was achieved after 2 days in dense (≥ 3 mg/ml) but not sparse gels, revealing that the latter gels are not suitable tissue surrogates in terms of oxygen distribution. In dense gels, a dominant effect of ECM composition over density in oxygen consumption as observed. All diffusion and consumption data were used in a

simple model to estimate ranges for gel thickness, seeding density and time-window that may support physiologic oxygen tension. Thus, critical variables for oxygen tension in ECM gels were identified, and a model to assess initial values of these variables was introduced, which may short-cut the optimization step of 3D culture studies.

In summary, this thesis work examines in detail the passive transport of both macromolecules and oxygen within ECM gels used in 3D cultures, and analyses to what extent these ECM gels can be used as a tissue surrogate in terms of transport. In addition, quantitative guidelines for the design of experiments with 3D cultures are provided aiming to render more physiologic molecular transport.

1 Introduction

Chapter 1 Introduction

1.1 The impact of cell culture in life sciences

Cell culture could be defined as the process by which cells are grown under controlled conditions, outside of their natural environment. Cell culture is an integral part of cell biology and it represents the primary way in which cell biology reaches into related disciplines, since the maintenance and propagation of cells has become an important tool in biochemistry, biophysics, genetics, immunology, physiology, molecular biology, and neuroscience.

Cell cultures aim to maintain or expand a population of cells, and the single most important consideration is cell viability. Cell number quantification and viability testing are important steps in standardizing culture and experimental conditions. As cells replicate in culture, passaging allows their number to be expanded to meet experimental needs. The choice of the medium greatly influences the success of the cell culture. A medium needs to provide the nutritional requirements of the cells as well as any required growth factors, and maintain pH and osmolarity compatible with survival.

The types of cells that can be studied experimentally has been significantly influenced by the development of a wide variety of cell culture media, since cell lines that proliferate in a particular environment are always selected at the expense of those that do not [1].

1.2 The extracellular matrix and three-dimensional cell cultures

Following its invention, the Petri dish has significantly influenced the way cells are cultured and manipulated. Traditionally, cells have been cultured in a Petri dish, a two-dimensional plastic or glass substrate, for over a century. However, cells in a living

organism have a three-dimensional environment. Thus, all tissue cells are attached to a 3D extracellular matrix.

The extracellular matrix (ECM) is the noncellular component that can be found within all tissues and organs. The ECM is composed of glycoproteins and glycosaminoglycans(GAG's) [2]. However, each tissue has an ECM with a unique composition and topology. This diversity is generated during tissue development through a dynamic, biochemical and biophysical interaction between the various cellular components and the evolving cellular and protein microenvironment. Therefore, besides being tissue specific, the composition of the ECM is also markedly heterogeneous.

The ECM is highly dynamic and is constantly being remodeled and its molecular components are subjected to many modifications. It generates the biochemical and mechanical properties of each organ, such as its tensile and compressive strength and elasticity, and provides protection by maintaining extracellular homeostasis and water retention. In addition, the ECM directs essential morphological organization and physiological functions by binding growth factors (GFs) and interacting with cell-surface receptors to elicit signal transduction and regulate gene transcription. [3]

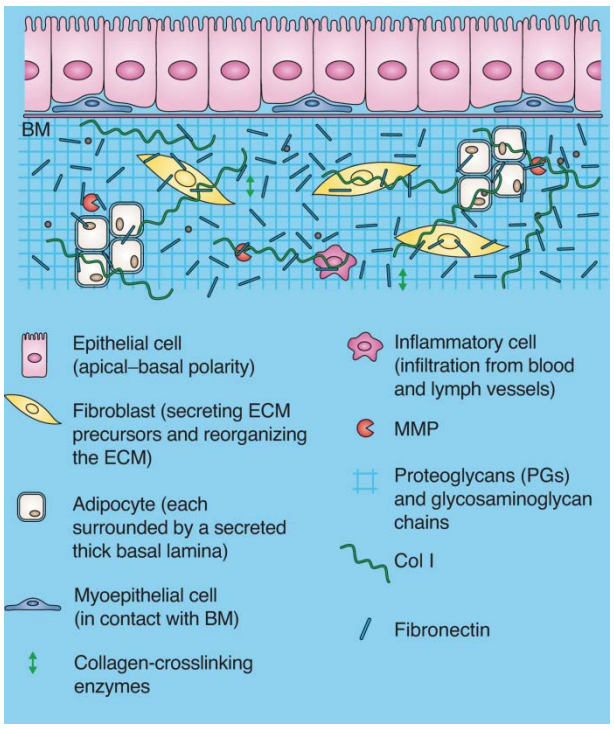

Fig. 1.1 Normal extracellular matrix structure, including different types of cells and some of the main ECM proteins, including collagen I and fibronectin. Adapted from [3]

The properties of the ECM in a given tissue can vary tremendously from one tissue to another (e.g. lungs versus skin versus bone) and even within one tissue (e.g. renal cortex versus renal medulla), as well as from one physiological state to another (normal versus cancerous).

The two main classes of macromolecules that make up the ECM are glycosaminoglycans (GAGs) and fibrous glycoproteins [4]. The main fibrous ECM proteins are collagens, elastins, fibronectins and laminins [3]. GAGs fill the majority of the extracellular interstitial space within the tissue in the form of a hydrated gel [4]. The polysaccharide gel has the ability to resist compressive forces on the matrix while allowing diffusion of nutrients, metabolites and hormones between the blood and the tissue cells. The collagen fibers strengthen and help organize the matrix and rubberlike elastin fibers give it resilience. Finally, many matrix proteins help cells attach in the appropriate places [5].

A large number of tissue culture models have been developed the past years in order to study the connection between the biochemical and biophysical properties of the extracellular matrix and the behavior of embedded cells. The field of 3D culture scaffolds can be divided in two categories: natural and synthetic.

While synthetic scaffolds provide an interesting proposition, they present certain limitations and challenges. Many of these scaffolds lack control over cell-adhesion sites, matrix viscoelasticity, porosity, growth-factor binding and matrix degradation and therefore do not mimic the organizational features of native gels [3, 6]. This work is centered on the study of natural ECM tissue cultures and is described in the following section.

1.3 Native ECM 3D scaffolds

The recognition of the important ECM regulatory role *in vivo* has extended the use of three-dimensional (3D) cultures based on growing cells embedded in gels of native ECM components [6, 7]. Thus, the availability of ECM macromolecules from major tissue types has enabled using 3D cultures to study different cell types in a variety of physiopathological processes. Natural ECM gels (Fig. 1.2), are readily accessible and

provide the spectrum of chemical and physical cues that are needed to induce morphogenesis from many cells.

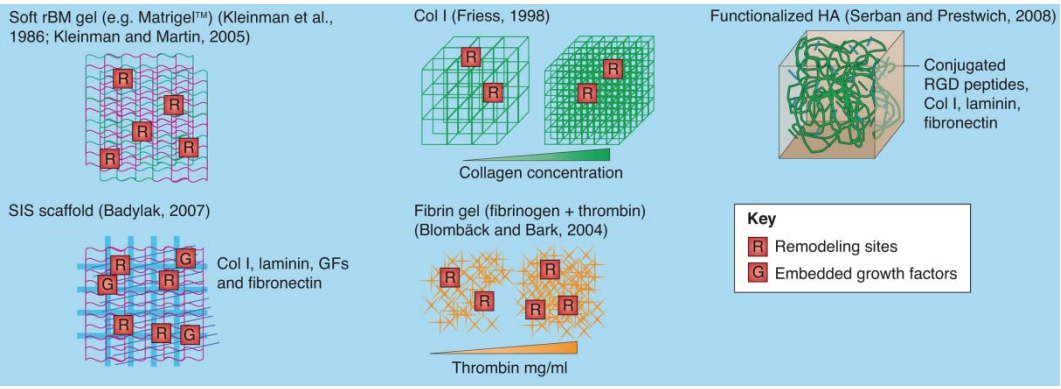

Fig. 1.2 Collection of the most common natural engineered ECM gels. Adapted from [3]

The most widely used ECM components in 3D cultures include **rBM, type I collagen and fibrin**. Reconstituted basement membrane, **rBM** (commercially known as Matrigel), is the extract of the basement membrane-like ECM that is secreted by the murine Engelbreth-Holm-Swarm (EHS) tumor. It is rich in laminin, type IV collagen, heparin sulphate proteoglycans and growth factors. It supports the in vitro formation of tubes from endothelial cells, as well as the in vitro differentiation of many epithelial cell types [6]. Accordingly, rBM has been used in physiopathological processes such as differentiation [8], branching morphogenesis [9, 10] and invasion [11, 12]. **Fibrin** is a natural structural matrix that occurs in wound healing. It forms gels by the enzymatic polymerization of fibrinogen at room temperature in the presence of thrombin. Fibrin has been successfully used in studies of capillary morphogenesis by endothelial cells [9, 13]. **Collagen** is the most abundant fibrous protein within the interstitial ECM. Collagens provide tensile strength, regulate cell adhesion, support chemotaxis, migration, and direct tissue development. Specifically, Collagen type I assembles into a network of fibrils that can be oriented, functionally modified, enzymatically or chemically crosslinked or stiffened. It has been extensively used in studies of tumor progression and invasion [3, 14, 15]. 3D culture studies have revealed that cells sense both the physical and biochemical properties of their surrounding ECM through specialized receptors [8, 16], and integrate ECM cues with soluble microenvironmental factors to regulate cellular fate [6, 17].

1.3.1 Mimicking the regulation of transport

One of the main functions that native ECM scaffolds look to mimic is the regulation of transport. The ECM provides biochemical cues that are critical for normal tissue homeostasis and for the progression of many pathological processes [3, 17]. In vivo, the movement of cells follows a chemical signal or molecular gradient in three dimensions that can not be replicated in two dimensions. Furthermore, diffusion and binding of many proteins, such as growth factors, is regulated by the 3D matrix. Likewise, the molecular gradients that are created due to diffusion play key roles in many biological processes and the extracellular matrix effectively acts as the "pool" where soluble factors may move towards cells. Accordingly, 3D cultures are considered to be more physiologically relevant than conventional two-dimensional (2D) cultures [3, 8] in terms of transport. The transport of oxygen and nutrients is provided to cells by diffusion, a process by which the population of particles is transported from regions of high concentration to regions of low concentration so as to decrease the concentration gradient.

1.4 Rationale: current limitations of 3D cultures in terms of transport

In this subchapter I will describe the current limitations of the quantification techniques regarding transport in 3D cultures. The dynamic that drives macromolecular diffusion is distinct from that of oxygen diffusion, mainly because of size and interaction with the ECM. Also, the quantification techniques are distinct. Due to these reasons, macromolecular diffusion and oxygen diffusion and consumption will be treated in separate subsections.

1.4.1 Macromolecular diffusion

A major role of ECM *in vivo* is to hinder the diffusion of soluble signaling factors involved in tissue homeostasis [18, 19]. The physiological relevance of diffusion hindrance is particularly clear in the regulation of extravascular transport and in the

formation of the chemical gradients that guide chemotaxis during development or wound healing [6, 20]. Diffusion hindrance *in vivo* is also relevant in biomedicine, since the transport of drug delivery particles is ultimately limited by diffusion [18, 21]. In addition to tissues, previous studies have indicated that diffusion hindrance occurs in ECM gels used in 3D cultures [9, 22], although to what extent gels mimic tissue hindrance is not well established. All these previous work support that hindered diffusion depends strongly on the geometrical obstacles posed by cells and the ECM [19, 23]. However, while diffusion hindrance caused by cellular obstacles has been extensively analyzed both experimentally and theoretically [19, 23-25], the physical basis underlying ECM-dependent hindrance remains poorly understood [19, 23].

Reduced diffusion depends not only on geometrical factors, but also on the physicochemical properties of the diffusing particle –i.e. size, shape and charge– and on the ECM-particle interactions [19, 26] and the contribution of geometrical and non-geometrical factors is unclear. A major consequence of this multi-factorial dependence of macromolecular transport is that the design and interpretation of 3D culture experiments require detailed knowledge of the diffusivity of the target signaling factor(s) within the specific ECM gel used in the 3D culture. Nonetheless, although the diffusivity of macromolecules in free solution and agarose gels have been extensively studied [16, 27, 28], quantitative analyses of their diffusivity in ECM gels are still scarce.

1.4.2 Oxygen diffusion and consumption

In terms of oxygen diffusion, a major challenge of 3D cultures is to reproduce oxygen tension values found in tissues, which are commonly expressed in terms of oxygen partial pressure (p). *In vivo*, oxygen is delivered to tissue cells through the microvasculature, which exhibits p levels ~40 mmHg [29]. Likewise, normoxic p values fall within the range of 20-50 mmHg in most tissues including liver, brain or bone marrow, and raise up to 75-100 mmHg specifically in arteries and alveoli [29-31]. In contrast, oxygen tension drops beyond 10 mmHg in hypoxic conditions including tissue injury, fibrotic lesions and solid tumors [29]. Thus, it is experimentally appealing to reproduce either normoxic or hypoxic microenvironments in 3D culture studies. However, it remains ill defined to what extent oxygen tension in 3D cultures approaches

the normoxic/hypoxic values found *in vivo*, or rather the hyperoxic *p* values (≥ 100 mmHg) of 2D cultures [6, 29]. Unlike tissues, oxygen delivery in 3D cultures is carried out by passive diffusion from ambient air throughout the gel. Consequently, the actual oxygen tension within the gel is ultimately determined by the balance between oxygen diffusion and consumption. Previous studies of oxygen distribution in hydrogels have been reported mostly in the context of tissue engineering, which seeks the production of thick tissues that are clinically valuable in terms of transplantation and/or regeneration [32]. Many of these studies have optimized oxygen delivery in the context of bioreactors and using cells cultured in either non-mammalian scaffolds like agarose or alginate, or in porous synthetic hydrogels with suitable biocompatibility and biodegradability properties [6, 32]. In contrast, previous studies of oxygen tension in ECM gels used in 3D cultures are scarce, particularly in rBM. As a consequence, the limitations of 3D cultures in terms of oxygen delivery still remain poorly defined. Moreover, quantitative criteria to help design 3D culture experiments in terms of optimizing oxygen distribution are currently lacking.

In the next chapter I will provide the theoretical framework of diffusion and consumption, highlighting the current existing paradigms that are used to analyze the limitations presented above.

1.5 Theoretical framework: diffusion and consumption

Diffusion of particles is expressed in terms of the concentration and flux of particles. In one dimension, C(x,t) is the concentration of particles at point *x* an time *t.* The flux of particles $\phi(x,t)$ is the net number of moles of particles crossing per unit time at time *t* through a unit area perpendicular to the *x*-axis and located at *x* [33].

1.5.1 Fick's first law

Fick's first law states that the flux of particles in the positive *x*-direction, $\phi(x,t)$, is proportional to the spatial gradient of particle concentration, C(x,t),

$$\phi(x,t) = -D\frac{\partial C(x,t)}{\delta x}, \qquad (1.1)$$

where D is called the diffusion coefficient or diffusivity (it is assumed that D≥0). The values of D depend on the characteristics of the diffusing particles and on the characteristics of the medium through which the particles diffuse. Fick's first law states that there is a flux of diffusible particles from regions of high concentration to regions of low concentration and that the flux is largest where the concentration gradient is largest. Therefore, the flux of particles is in a direction that reduces the particle concentration gradient.

1.5.2 Fick's second law: The diffusion equation

Considering the continuity equation,

$$\frac{\partial \phi(x,t)}{\partial x} = \frac{\partial C(x,t)}{\partial t} \tag{1.2}$$

, which expresses the conservation of particles in one dimension, and combining it with Eq. (1.1), you obtain:

$$\frac{\partial C}{\partial t} = D\frac{\partial^2 C}{\partial x^2} \tag{1.3}$$

,which is known as Fick's second law of diffusion.

1.5.3 Relationship between D and non-geometric factors: The Stokes-Einstein relation

The diffusion coefficient (*D*) determines the time it takes a solute to diffuse a given distance in a medium. Previous studies have identified that diffusivity within tissues and ECM has two major contributions. First, a geometrical contribution due to the space-filling obstacles such as cells and ECM filaments, which are expected to scale with cell and ECM density, respectively. Second, non-geometrical contributions such as the viscous interactions with cell walls and ECM macromolecules. Current models assume that the former effects are dominant. However, the actual relative contribution of geometrical and non-geometrical factors to diffusion hindrance are ill defined.

The simplest model that accounts for the non-geometrical contribution due to viscosity is described by the Stokes-Einstein law. If we assume a spherical solute particle, for which the molecular weight is proportional to the molecular volume, which is proportional to a^3, where a is the molecular radius, then $D \propto M_r^{-1/3}$, where M_r is the molecular weight which implies that $D \propto a^{-1}$. This relation is predicted by the Stokes-Einstein relation.

The force that is required to move a sphere of radius a through a viscous medium is described by

$$f_p = 6\pi a \eta v \tag{1.4}$$

,where η is the viscosity of the medium, and v is the velocity of the particle. Eq(1.4) is known as Stoke's law. The particle mobility, u_p, can be defined as the ratio of the particle velocity to the force on the particle:

$$u_p = \frac{v}{f_p} = \frac{1}{6\pi a \eta} \tag{1.5}$$

Considering the Einstein relation in terms of particle mobility:

$$D = u_p k_B T \tag{1.6}$$

, where D is the diffusion coefficient, k_B is the Boltzmann constant and T is the absolute temperature. Replacing Eq.(1.5) into Eq.(1.6), the Stokes-Einstein equation is finally obtained:

$$D = \frac{kT}{6\pi a \eta} \tag{1.7}$$

1.5.4 Solute in a polymer

For a solute in water, the dependence of the diffusion coefficient on the molecular weight can be expressed for a large number of solutes using the following approximation:

$D \propto M_r^{-1/3}$, for $M_r > 10^3$

$D \propto M_r^{-1/2}$, for $M_r < 10^3$

The first power-law relation ($D \propto M_r^{-1/3}$) can be derived from Stokes-Einstein law. In general, different power-law exponents are expected depending on the media the solute is moving in. A general equation has been established to encapsulate its use in other materials such as polymers. The expression:
$D \propto M_r^{-m}$ shows a power function relating the diffusion coefficient to the molecular weight while the exponent *m* varies from 0.5 to 4(for certain polymers such as polystyrene) [33].
In general, the contribution of ECM to interstitial viscosity remains an open question [19], and there are no standardized biophysical models for diffusion, but rather models that capture different physical effects in isolation.

1.5.5 Tortuosity

Tortuosity is the parameter commonly used to characterize diffusion hindrance in both tissues and hydrogels, and is defined as $\lambda = (D_{free}/D_{medium})^{1/2}$, where D_{free} and D_{medium} are the diffusivity of the particle in free aqueous solution and in the specific medium (tissue or hydrogel), respectively [19, 23, 26].

1.5.6 Michaelis-Menten dynamics

As far as oxygen diffusion and consumption go, the mass balance of oxygen in the gel can be described by using Fick's second law with a reaction term:

$$\frac{\partial C}{\partial t} = D\frac{\partial^2 C}{\partial x^2} + R \tag{1.8}$$

,where *R* indicates the oxygen consumption rate (OCR) per unit volume.
Accordingly, the rate of O2 consumption of cells follows the Michaelis-Menten kinetics. Previous studies in hydrogels indicate that this dynamic is well captured as [34, 35].

$$\frac{R}{k_{H,L}} = \rho_{cell} \frac{V_{max} p_G}{K_m/k_{H,L} + p_G} \tag{1.9}$$

Where $k_{H,L}$ is Henry's constant for oxygen in liquid, and p_G is the recorded pressure inside the sample. Henry's law of solubility is used to convert pressure to concentration and viceversa. It states that "At a constant temperature, the amount of a given gas dissolves in a given type and volume of liquid is directly proportional to the partial pressure of that gas in equilibrium with that liquid"
Put in mathematical terms, it is expressed as: $C = k_H p_G$.

1.5.7 The Thiele modulus

By non-dimensionalizing Eq. (1.8), a dimensionless parameter that captures many relevant dimensional parameters is obtained:

$$\phi^2 = h^2 \frac{\rho_{cell} V_{max}}{K_m D_G^*} \tag{1.10}$$

where h is the gel thickness, ρ_{cell} is the uniform volumetric cell density, V_{max} is the maximum oxygen consumption rate (OCR) per cell, K_m is the oxygen concentration at which OCR is half that of V_{max} and D_G^* is the diffusivity inside a sample containing cells that consume oxygen.
This parameter is defined as the Thiele modulus and it is increasingly used to quantify the relative importance of oxygen consumption over diffusion in engineered tissues [35]. If $\phi^2 < 1$, the system is considered to be diffusion dominated (i.e. rate of diffusion is fast compared to rate of consumption), whereas $\phi^2 > 1$ indicates otherwise.
In order to highlight the usefulness of the Thiele modulus, in (Fig 1.3), two different cell culture designs can be seen. Despite the fact they have different thicknesses and different cell densities, the two have the same Thiele modulus value.

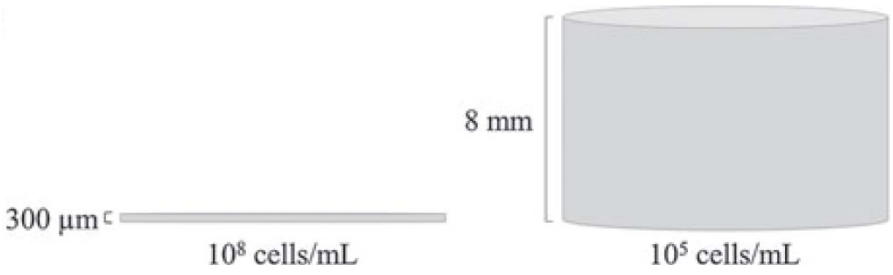

Fig 1.3 A gel with 300 µm thickness and 10^8 cells/mL density has the same Thiele modulus as a gel with 8mm thickness and 10^5 cells/mL density. Modified from [35].

In the following chapter I will describe the most common techniques that are used to quantify macromolecular diffusion and oxygen tension.

1.6 Measurements of diffusion coefficients and oxygen dynamics in 3D cultures

1.6.1 Macromolecular diffusivity quantification techniques

Naturally, in order to mimic in vivo conditions to the fullest, diffusion must be considered as a very important issue in 3D cultures. Within a tissue, concentration gradients exist for any soluble factor that is produced or consumed by the cells, ranging from nutrients to effector molecules [6]. These gradients are captured by the diffusion coefficiens of the diffusible species within the 3D environment.

There are several techniques available to quantify molecular diffusion in a 3D environment. Most notably, fluorescence recovery after photobleaching (FRAP) has been a standard technique for measuring diffusion coefficients of fluorescent tracer proteins for many years now. In FRAP experiments, a high-powered focused laser beam is used to irreversibly photobleach the fluorescent molecules in a small area. This procedure is followed by a recovery of the fluorescence due to diffusion of the surrounding non-bleached fluorescent molecules into the bleached area [36].

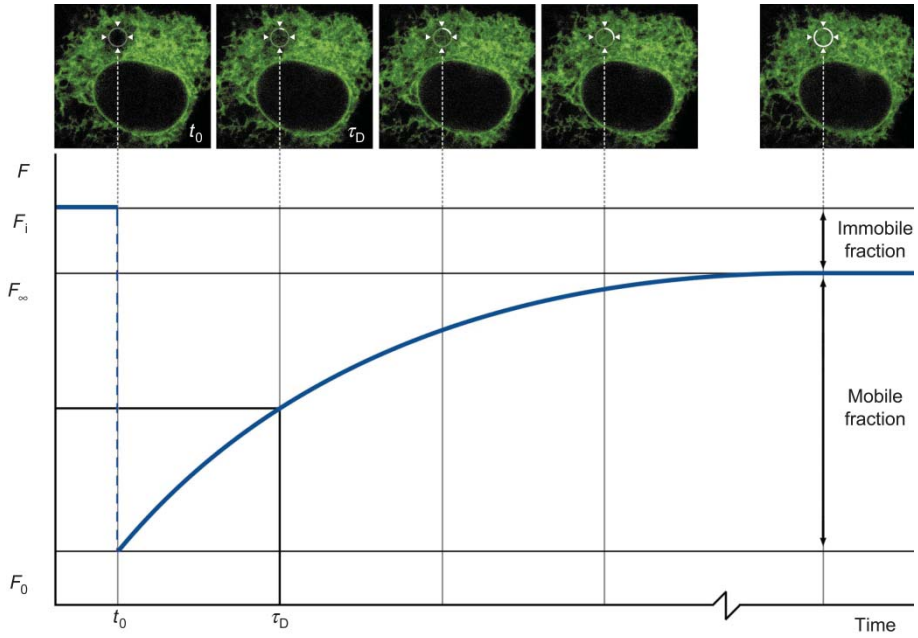

Fig. 1.4. Fluorescence recovery after photobleaching (FRAP). When a region in the fluorescent area is bleached at time t_0 the fluorescence decreases from the initial fluorescence F_i to F_0. The fluorescence recovers over time by diffusion until it has fully recovered (F_∞). The characteristic diffusion time τ_D indicates the time at which half of the fluorescence has recovered. The mobile fraction can be calculated by comparing the fluorescence in the bleached region after full recovery (F_∞) with that before bleaching (F_i) and just after bleaching (F_0). Reproduced from [36].

Quantitatively, FRAP experiments give information about the mobility of a fluorescent molecule in a defined space. There are two main parameters that can be deduced from a FRAP curve. These are the mobile fraction of fluorescent molecules and also the mobility rate, which is directly related to the characteristic diffusion time, τ_D (Fig.1.4). In turn, the diffusion time is related to the diffusion coefficient, which is often the desired way to quantify mobility. Other techniques of measuring diffusion coefficients of fluorescent tracers include fluorescence microscopy, fluorescence correlation spectroscopy (FCS) and confocal microscopy. Of note, the standard diffusion coefficient measuring techniques include the use of a specialized microscope.

1.6.2 Oxygen tension quantification techniques

In terms of oxygen tension, the most notable quantification techniques can be divided into 3 categories: chemical, optical, and nuclear/magnetic [37].

The most notable of the **chemical methods** is the polarographic electrode. This method is based on measuring the electric current that results from an electrochemical reduction of oxygen at the cathode. In order to provide minimum invasiveness, during the past years, miniaturized polarograhic electrodes have been designed. These "microelectrodes" are now available in the range of 5-10μm in diameter (Fig 1.5).

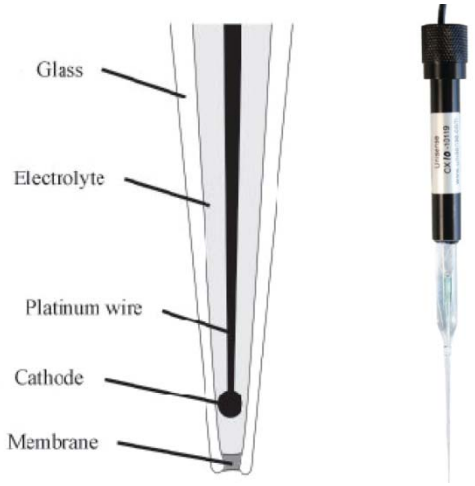

Fig 1.5. Oxygen microsensor including the main components of the tip. Modified from unisense.com

This technique has been considered the "gold standard" for measuring tissue oxygenation, due to its extensive use, especially in tumors and brain tissue.

Other chemical methods include transcutaneous oxygen sensors and immunochemical methods.

In terms of **optical methods** to measure oxygen pressure, fluorescence oxymetry is perhaps the most widely used. It is based on oxygen-dependent changes in the lifetime of fluorescence. OxyLite, a widely used commercially available sensor has used this principle in its construction. The sensor uses ruthenium chloride, a fluorescent dye, connected to the tip of a fiber optic cable. The fluorophores of the dye are excited by the photodiodes, and the fluorescence lifetime is inversely related to the oxygen tension at

the tip. Fluorescence oxymetry does not consume oxygen and has been widely used in oxygen measurements of tumor, liver and brain. Other notable optical methods include phosphorescence oxymetry, pulse oxymetry and near-infrared spectroscopy.

Among the **nuclear and magnetic methods**, Electron Paramagnetic Resonance (EPR) oximetry has been most widely used. Other techniques include Positron emission tomography (PET) imaging and 19F MRI.

1.7 Measurements of geometrical and non-geometrical properties of ECM gels with AFM

Molecular diffusion can be directly related with the ECM gel intrinsic properties such as pore size and viscosity. These properties can be examined using Atomic Force Microscopy (AFM). AFM is a very versatile nanotechnique that belongs to the family of scanning probe microscopies. The principle of operation is based on a micrometer- or nanometer-sized physical probe that is brought to close proximity to the surface of a sample with the aid of a piezoelectric positioner. A map displaying quantitative information of either the topography or a specific physical property of the probe–sample interaction can be obtained. In AFM, the probe is a sharp tip at the end of a flexible cantilever that can readily detect forces from few piconewtons up to hundreds of nanonewtons with very high spatial resolution [38]. Among the uses of AFM, imaging and viscoelasticity measurements are of particular interest.

In terms of viscoelasticity measurements, the complex shear modulus ($G^*(f)$) can be obtained by applying small oscillations to deform the sample and measuring the G' (elastic storage modulus) and G'' (viscous loss modulus).

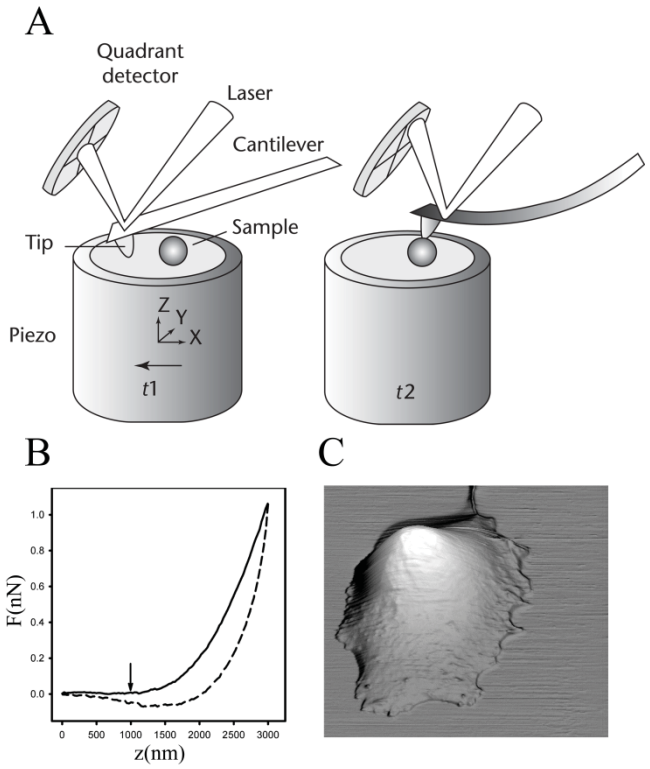

Fig. 1.6.Atomic force microscopy layout and operation. (A)General layout of the AFM setup in a sample scanner configuration. The deflection of a cantilever with a sharp tip at its end is monitored by a focused laser beam that reflects from the cantilever on to a quadrant photodiode. A piezoelectric scanner moves the sample in the three dimensions. In this schematic representation, at time t1 the tip is positioned next to a spherical object, whereas at t2 the object is positioned below the tip, resulting in the deflection of the cantilever that will be detected as a light imbalance between the top and bottom photodiode segments. (B) A typical force-displacement curve obtained by moving the cantilever downward and then upward. The arrow indicates tip cell contact. (C)Topographical image of an epithelial cell obtained with AFM. (A) was adapted from [38], (B) and (C) were adapted from [39] .

2 Aims

Chapter 2 Aims of the thesis

2.1 General aim

The general aim of this thesis was to study the transport properties of the most common three dimensional extracellular matrix cell cultures.

2.2 Specific aims

1. To develop a simple assay for assessing the effective diffusion coefficients of soluble factors diffusing within 3D native ECM scaffolds and to establish the dominant matrix characteristics.

2. To study the transport of oxygen within 3D gels by measuring the oxygen partial pressure, to assess diffusivity, cell oxygen consumption rates and proliferation.

3. To analyze the implications of scaffold characteristics in molecular hindrance and provide insight towards improving 3D cultures in terms of diffusion.

3 Materials and Methods

Chapter 3 Methods

In this chapter, I will describe the methodological techniques that I used to conduct the experimental measurements of this thesis. In addition, I will present the theoretical approaches and models that I have employed. This chapter is divided into two modules: one concerning the diffusion of macromolecules and the other concerning the diffusion and consumption of oxygen.

In terms of macromolecular diffusion, I will first describe the preparation of the ECM gel samples. Second, I will reveal the macroscopic diffusivity assay and the subsequent modeling techniques for quantifying the diffusion coefficients. Third, I will present FRAP, a standard microscopic assay for measuring diffusion coefficients. Fourth, I will describe the AFM technique for assessing gel viscosity and pore size.

In terms of oxygen diffusion and consumption, I will first present the cell culturing technique. Second, I will describe the technique used for measuring oxygen partial pressure. Finally, I will reveal the modeling approaches I have taken to quantify the acquired data.

Isabel Pastor and Francesc Mas have contributed to the modeling approaches of macromolecular diffusion. FRAP measurements have been performed in collaboration with Isabel Pastor. Oxygen tension measurements have been performed in collaboration with Adai Colom.

3.1 Diffusion of macromolecules

3.1.1 Preparation of ECM gels for plate reader experiments

ECM gels were prepared at densities known to elicit physiologic responses [8-10]. rBM solution was used undiluted (12 mg/ml, Cultrex BME, Trevigen). COLI solution was prepared as reported elsewhere [10, 11]. In brief, acid soluble COLI (Cellagen IAC-50, Koken) was neutralized in DMEM to obtain a 4 mg/ml collagen solution, and diluted in serum-free culture medium (SFM) to a final density of either 1 or 3 mg/ml, which were referred to as sparse (1) and dense (3) densities owing to the proteolytic-independent

and dependent cellular invasion observed in these gels, respectively [10]. SFM consisted in HEPES (Sigma) buffered RPMI 1640 (Gibco). Dense fibrin (FIB) solution was prepared as previously described [9]. Briefly, fibrinogen (Sigma) was diluted in SFM to a final density of 3 mg/ml, and mixed with thrombin (50 U/ml, Sigma) 50:1 (vol/vol). For macroscopic diffusivity experiments, each different gel sample and experimental condition were prepared in triplicates in separate Transwell plates (24 Transwell plate with an 8 μm pore size permeable membrane, Corning) that contained two separate units: the top Transwell insert and the bottom lower Transwell compartment where the Transwell insert was loaded. The same day of the diffusivity measurements, 70 μl of either rBM or COLI solution were gently added to the bottom of a 6.5 mm wide Transwell insert, loaded into the lower Transwell compartment, incubated at 37ºC for 30 min to enable gelation, and immediately hydrated by adding 200 μl SFM on top of the gel. For FIB gels, 70 μl of fibrinogen+thrombin solution were added to the Transwell insert, kept at room temperature for 5 min, incubated at 37ºC for 25 min, and hydrated with SFM as in the other gels. Given the specific Transwell geometry, the theoretical gel thickness was 2 mm, which falls within the range commonly used in 3D cultures [40, 41]. For microscopic diffusivity experiments, 70 μl of each ECM solution were polymerized onto an 8-chamber culture slide (BD Falcon).

3.1.2 Macroscopic diffusivity measurements using a fluorescent plate reader

3.1.2.1 Experimental setup

A diffusion assay based on two tools commonly available in cell biology laboratories has been developed: a Microplate Reader and Transwell plates. To this aim, the macroscopic diffusivity of FITC-dextrans at 3 different M_r (4, 40 and 70 kDa, referred to as Dex4, Dex40 and Dex70 thereafter) (Sigma) through gel samples prepared as triplicates in Transwell Plates was examined with a Microplate Reader. Each experimental condition (dextran M_r and gel type) was examined in separate Transwell plates using a three-step protocol. First, the SFM on top of each gel-containing Transwell insert was gently removed and replaced with 200 μl of 1 mg/ml dextran solution. Second, each insert was loaded into a lower Transwell compartment

containing 1000 µl SFM (Fig. 3.1 left.). Thus, the final dextran solution volume was 1270 µl –where we considered 200 µl top SFM + 70 µl gel + 1000 bottom SFM–, thereby eliciting a final maximum dextran concentration of 157 µg/ml. Transwells without gels were used as negative controls.

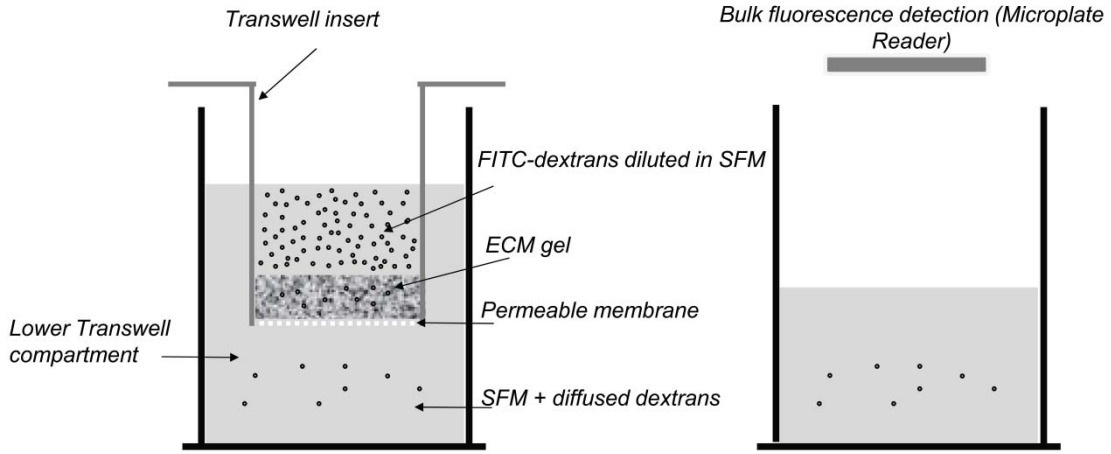

Fig. 3.1 .Scheme of the experimental set-up. Left: Insert containing the FITC-dextran solution inside a lower compartment where particles diffuse. Right: Lower compartment with diffused particles (the insert has been removed during the measurements) and fluorescence detection unit.

Third, the dextrans that had diffused throughout the entire gel thickness to the lower Transwell compartment were monitored as a function of time by measuring the total fluorescence intensity in the lower compartment (F_{PR}) at different time points with a Microplate Reader (Synergy 2 Multi-Mode Microplate Reader, BioTek), using wavelength excitation and emission filters of 485/20 nm and 528/20 nm, respectively (Fig. 3.1 right). For this purpose, inserts were quickly removed and transferred to an empty adjacent well for each Transwell plate before F_{PR} readings, and put back into their original lower compartments immediately after the readings to continue accumulating dextrans. F_{PR} was read at time intervals of 5 min during the first hour, and of 1 h up to 8 h. In these settings, preliminary studies indicated that measuring F_{PR} of each experimental condition required ~30 s, which was short enough with respect to the reading times to not compromise the expected slow monotonic increase of F_{PR} with time, even in the fastest diffusivity conditions. Transwell plates were protected from

light and kept at 37ºC in between F_{PR} readings. For each time point, F_{PR} was averaged for all repeated measurements (n=3).

3.1.2.2 Modeling diffusion: semi-infinite approach

A common approach to model diffusion through hydrogels considers them as a porous medium. In these conditions, the passive transport of particles in a preferred direction is well described by the one-dimensional (1D) Fick's 2nd law .

$$\frac{\partial C}{\partial t} = D\frac{\partial^2 C}{\partial^2 x} \tag{3.1}$$

where $C(x,t)$ is the concentration of diffusing particles as a function of time (t) and depth (x), and and D is the isotropic diffusion coefficient. The simplest strategy to solve Eq. (3.1) to model the diffusion of an extended initial particle distribution C_o assumes that the hydrogel is a semi-infinite slab, which can be expressed as $C(x \geq 0, t = 0) = 0$, $C(x \to \infty, t \geq 0) = 0$, and $C(x = 0, t \geq 0) = C_0$. The well-known solution of Eq. (3.1) that fulfils the latter initial and boundary conditions is [42]

$$C(x,t) = C_0 \cdot erfc\frac{x}{2\sqrt{Dt}} \tag{3.2}$$

where *erfc* is the error function complement. Eq. (3.2) has been applied to model diffusion in hydrogels in a variety of applications including tissue engineering [9, 25] and chemotaxis [43, 44]. Likewise, Eq. (3.2) has been adapted to model the macroscopic measurements in a first approximation as

$$C_l(t) = C_0 \cdot erfc\frac{l}{2\sqrt{Dt}} \tag{3.3}$$

where l is the gel depth, and $C_l(t)$ is the dextran concentration at $x = l$. Eq. (3.3) was fitted to the average F_{PR} data obtained for each M_r and ECM gel by nonlinear least-squares fitting with MATLAB (The Mathworks), being l and the effective diffusivity D fitting parameters. As initial fitting values l = 2 mm and D predicted by the Stokes-Einstein law for water [18] were used. Eq. (3.3) was also used to assess the time to reach 50% of C_0 (t_{50}) by imposing $erfc\frac{l}{2\sqrt{Dt}} = \frac{1}{2}$ using MATLAB, which elicited

$$t_{50} = l^2/0.9D \tag{3.4}$$

The effective viscosity η was assessed from D data using Stokes-Einstein law [18]

$$\eta = k_B T/6\pi D R_H \quad (3.5)$$

,where k_B is the Boltzmann's constant, T is the absolute temperature, and R_H is the hydrodynamic radius. The latter was assessed using a previously reported empirical relation [45], which elicited 1.21 nm for Dex4, 4.12 nm for Dex40 and 5.55 nm for Dex70.

3.1.2.3 Modeling diffusion: finite approach

A more realistic model of the macroscopic diffusion measurements should take into account both the finite gel thickness and flux of dextrans into the lower Transwell compartment where the fluorescence measurements were made. For this purpose, the dextran diffusion through the 3 layers of the macroscopic set-up was considered: a top layer where the initial source of dextran solution is, a middle layer containing the gel, and a bottom layer corresponding to the bottom transwell compartment where the dextrans that exit the gel are accumulated. These 3 layers are reffered to as source, gel and bottom, respectively. For simplicity, the model assumes that all 3 layers are flat and parallel, and the diffusion is largely 1D (Fig. 3.2).

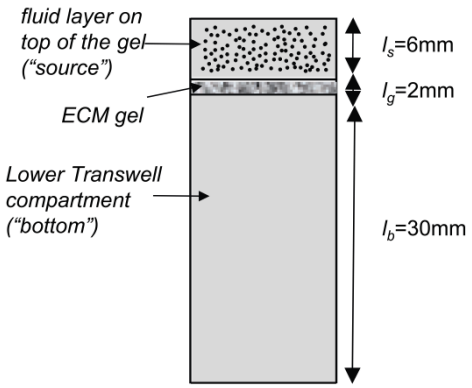

Fig 3.2. Finite gel diffusion model including the 3 layers.

In these conditions, Fick's 2nd law of diffusion that applies to each layer can be expressed as

$$\frac{\partial c_s}{\partial t} = D_0 \frac{\partial^2 c_s}{\partial x^2} \;\; ; \;\; 0 \le x \le l_s \tag{3.6}$$

$$\frac{\partial c_g}{\partial t} = D_g \frac{\partial^2 c_g}{\partial x^2} \;\; ; \;\; l_s \le x \le l_g \tag{3.7}$$

$$\frac{\partial c_b}{\partial t} = D_0 \frac{\partial^2 c_b}{\partial x^2} \;\; ; \;\; l_g \le x \le \infty \tag{3.8}$$

where the subscripts *s*, *g* and *b* refer to the source, gel and bottom layers, respectively, *c* is the dextran concentration, *l* is the vertical length of the layer, D_o is the diffusivity in free solution, and D_g is the diffusivity in the gel. In Eq. (3.8) the approximation that the bottom layer is much thicker than the other two layers has been used.

The fluorescence of the FITC-dextrans in the bottom Transwell compartment (F_{PR}) as a function of time has been measured in this assay, which is proportional to the average dextran concentration in the bottom layer ($c_{avg}(t)$). The latter can be theoretically computed by integrating the flux of dextrans at the gel-bottom layer interphase as

$$c_{avg}(t) = \frac{A}{V_b} \int_0^t \left| D_g \left(\frac{\partial c_g(x,t')}{\partial x} \right)_{x=l_g} \right| dt' \tag{3.9}$$

where *A* is the surface area of each layer (taken equal to area of the bottom of the Transwell insert), and V_b is the volume of the bottom layer. To assess Eq. (3.9), Eq. (3.6-3.8) have been solved using the following 3 initial conditions and 6 boundary conditions:

- initial conditions: (3.10)

(i) $c_s(x, t=0) = c_0$

(ii) $c_g(x, t=0) = 0$

(iii) $c_b(x, t=0)=0$

- boundary conditions: (3.11)

(i) there is no flux exiting neither the top of the top layer nor the bottom of the bottom layer:

$$\left(\frac{\partial c_s}{\partial x}\right)_{x=0}=0 \quad \text{, and} \quad \left(\frac{\partial c_b}{\partial x}\right)_{x\to\infty}=0$$

(ii) concentration must be continuous at both the source-gel and gel-bottom interphases:

$$c_s(x=l_s,t)=c_g(x=l_s,t) \quad \text{, and} \quad c_g(x=l_g,t)=c_b(x=l_g,t)$$

(iii) flux must be continuous at both the source-gel and gel-bottom interphases:

$$D_0\left(\frac{\partial c_s}{\partial x}\right)_{x=l_s}=D_g\left(\frac{\partial c_g}{\partial x}\right)_{x=l_s} \text{, and} \quad D_g\left(\frac{\partial c_g}{\partial x}\right)_{x=l_g}=D_o\left(\frac{\partial c_b}{\partial x}\right)_{x=l_g}$$

Solving Eq. (3.6-3.8) and imposing these initial and boundary conditions required using the Laplace transform which elicited

$$\bar{c}_{avg}(s)=\frac{A}{V_b}\frac{c_0}{s}\sqrt{\frac{D_g}{s}}\frac{2}{(1-D_{g0})}\left\{\frac{\exp\left(+\sqrt{\frac{s}{D_g}}l_g\right)}{\left(RD(s)-1\right)+D_{g0}\coth\left(+\sqrt{\frac{s}{D_0}}l_s\right)\left(1+RD(s)\right)}\right\} \tag{3.12}$$

where s the Laplace variable associated with t, $\bar{c}_{avg}(s)$ is the Laplace transform of $c_{avg}(t)$, and D_{g0} and $RD(s)$ are defined as

$$D_{g0}=\sqrt{\frac{D_g}{D_0}}$$

$$RD(s)=\left(\frac{1+D_{g0}}{1-D_{g0}}\right)\exp\left(+2\sqrt{\frac{s}{D_g}}l_g\right)$$

An analytical expression for the inverse Laplace transform of Eq. (3.12) is not available. Instead, a numerical inverse Laplace transform of Eq. (3.12) was fitted to F_{PR} values

obtained for each experimental condition by nonlinear least-squares fitting with MATLAB, being D_g, l_g and Ac_o/V_b fitting parameters. For this purpose the Levenberg–Marquardt algorithm (LMA) was used, which is a very popular numerical approach used for curve-fitting of nonlinear functions. Using this approach, D_g from data obtained with Dex40 and Dex70 in dense ECM gels (rBM, dense FIB and dense COL) was assessed. To further assess the consistency between both models, the D_g values obtained with the finite model as a function of dextran's molecular weight (M_r) have been plotted, and the plot was completed with D_g values obtained with the semi-infinite model on Dex4. Importantly, a power-law with a single common exponent to all these data ($D_g \sim M_r^{-\alpha}$) was fitted. In contrast, the LMA-based fitting method was numerically unstable for conditions where D_g is close to D_o due to divergences arising in the denominator of Eq. (3.12), which corresponds to either Dex4 diffusing in any of the gels or both Dex40 and Dex70 diffusing within sparse COLI gel.

3.1.3 Microscopic diffusivity measurements by fluorescence recovery after photobleaching (FRAP)

Dex4 solution was added to each ECM gel 3 days before experiments to enable reaching equilibrium or near-equilibrium concentrations [9], and kept at 37ºC. FRAP measurements were conducted with a scanning confocal microscope (TCS SP2 UV, Leica) provided with a heating stage that kept gels at 37ºC. Samples were illuminated with a 10× 0.4 NA objective and a 488 nm excitation line from a 30 mW Ar^+ laser operating at 8% output power. Photobleaching of a 40 μm wide circular region-of-interest (ROI) was achieved with a 488 and 514 nm excitation line from the Ar^+ laser at 100% of relative intensity. The bleaching time was 1.4 s, and the total ROI fluorescence intensity images after photobleaching were collected as a function of time at intervals of 0.28 ms up to 50 s at 512×512 pixel resolution using a 1 AV pinhole (n=6 per gel type). These settings were selected to minimize the fluorescence contribution from the diffusion of FITC-dextrans along the axial direction and to prevent any recovery during bleaching [46-48]. FRAP measurements were modeled assuming that the bleached area had a uniform circular disk profile, as supported by previous studies [45, 49], which enabled analyzing all the fluorescence recovery curves using the equation [50]:

$$F_{ROI}(t) = [F_\infty - F_0]\left[\exp\left(-\frac{2\tau_D}{t}\right)\left[I_0\left(\frac{2\tau_D}{t}\right) + I_1\left(\frac{2\tau_D}{t}\right)\right]\right] + F_0 \quad (3.13)$$

where $F_{ROI}(t)$ is the normalized mean fluorescence intensity in the bleached ROI at t, F_∞ is the recovered fluorescence at large t, F_0 is the bleached fluorescence intensity at $t = 0$, τ_D is a characteristic residence time of the diffusing particle in a volume of characteristic length ω(i.e. the radius of the bleached ROI), and I_0 and I_1 are the modified Bessel Functions. Eq. (3.13) was nonlinear least-squares fitted to FRAP measurements with MATLAB, being τ_D a fitting parameter. The latter was used to assess the effective diffusion coefficient as $D_{FRAP} = \omega^2/4\tau_D$. D_{FRAP} data were averaged for all repeated measurements (n=6).

3.1.4 Gel viscosity assessment by Atomic Force Microscopy (AFM)

For AFM experiments, 100 µl of each ECM solution were added to glass-bottomed culture dishes (MatTek) and polymerized as described in Section 3.1.1. The dynamic viscosity of ECM gels was assessed by measuring the complex shear modulus ($G^*(f)$) over a frequency (f) range of 0.1-25.6 Hz with home-made stand-alone AFM [51] and a V-shaped cantilever provided with a spherical polystyrene tip (4.5 µm diameter, 0.01 nN/nm, Novascan). $G^*(f)$ was measured as previously described [52, 53]. In brief, low amplitude (75 nm) monofrequency oscillations were applied around a gel indentation δ_o = 600 nm. $G^*(f)$ was calculated as

$$G^*(f) = \frac{1-\nu}{4\sqrt{\delta_o R}}\left(\frac{F(f)}{\delta(f)} - i2\pi b(0)f\right) \quad (3.14)$$

where $F(t)$ and $\delta(t)$ are the Fourier Transforms of the force F and indentation δ recorded at each f, respectively, R is the tip radius (taken as 2.25 µm), v is the Poisson´s ratio (taken as 0.5) [54], and $b(0)$ is the cantilever drag factor assessed at the gel surface [55]. Details on the latter expression can be obtained elsewhere [52, 55]. $G^*(f)$ can be expressed as $G^*(f) = G'(f) + iG''(f)$, where G' and G'' are the (elastic) storage modulus and the (viscous) loss modulus, respectively. The effective viscosity at each f was calculated as $\eta_{AFM}(f) = G''(f)/2\pi f$ [56]. To assess the length scale of AFM measurements, the diameter a of the projected contact area between the AFM tip and the gel surface was estimated as $a = 2(R\delta)^{1/2}$ [57], which yielded $a \sim 2.3$ µm, revealing

that AFM measurements assessed the effective microscopic viscosity. Measurements were taken in 9 different regions of each gel (n=2).

3.1.5 Gel pore size assessment by AFM imaging

ECM gels were prepared as in Section 3.1.1. To enhance the lateral spatial resolution, gels were fixed with 1% glutaraldehyde (Sigma) PBS solution for 30 min before imaging to render stiffer gels by increased protein crosslinking [58, 59]. All gels were imaged in PBS at room temperature. AFM imaging was performed with a commercial stand-alone AFM (Bioscope I, Veeco) by raster scanning a V-shaped cantilever (0.01 nN/nm, 20 nm tip radius, MLCT, Veeco) over a scan size of 20-40 μm at low scan rate (≤ 0.2 Hz) in contact mode, using a minimum feedback loading force. Images were obtained in different locations (≥ 5) of each gel (n=2), and flattened with WSxM software [60]. For each image, pore edges were outlined manually and their corresponding areas were assessed with IMAGE J [61]. The pore width (w) for each pore area (A) was calculated as $w = 2\ (A/\pi)^{1/2}$, assuming that pores conformed to a circular geometry.

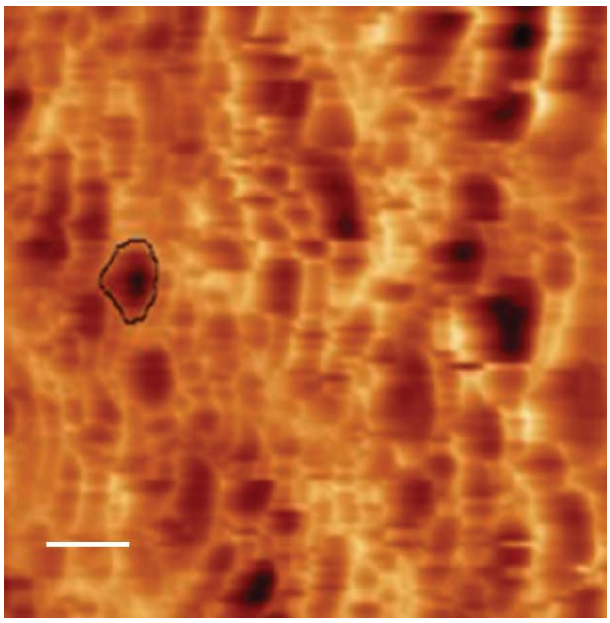

Fig 3.3 Image of a COLI gel taken with the AFM including a manually outlined pore. Scale Bar=5μm

3.2 Oxygen diffusion and consumption

3.2.1 Cell culture in 2D and 3D for oxygen pressure measurements

ECM solutions were prepared as described in Section 3.1.1. The human lung epithelial cell line A549 (ATCC) was propagated in 2D culture flasks as described elsewhere [16]. All 3D culture experiments were conducted in 96 well plates (0.335 cm^2 growth surface/well, TPP) using the same protocol for each ECM type. First, wells were pre-coated with a thin ECM layer to prevent cell migration by adding 35 µl of ECM solution and incubating it at 37ºC for 30 min to enable gelation. Second, A549 cells were trypsinized and resuspended with ECM solution at 0.8×10^6 cells/ml, and 215 µl of this mixture were added to a well, incubated at 37ºC for 30 min, and immediately hydrated with 90 µl of culture medium. To prepare acellular ECM gels, the same protocol was applied without mixing the ECM solution with cells. The theoretical thickness of the liquid and gel layers were 2.67 mm and ~ 7 mm, respectively. For 2D culture measurements, 25.000 cells were seeded on a bare well in culture medium. All samples were prepared as triplicates, and kept in the incubator until use.

3.2.2 Measurement of oxygen partial pressure using the Clark electrode

A high-spatial resolution fast Clark-type oxygen micro-electrode pipette (OX-50, 50 µm tip diameter, Unisense A/S) was used to measure p. The oxygen microsensor was calibrated before each experiment as described elsewhere [30]. Oxygen tension was recorded at the center of each well at different depths by driving the vertical position (x) of the microsensor with a micromanipulator. For 2D cultures, p was recorded in static conditions by holding x inside the culture medium and right above the surface of cultured cells for at least 30 s. For 3D cultures and acellular gels, p was measured in both static and dynamic conditions. Static measurements were carried out by holding x for at least 30 s at the following pre-determined depths: air (p_A^*, right above the air-liquid interface), liquid/culture medium (p_L^*, 2 mm deep from the air-liquid interface), and gel (p_G^*, 1.3 mm deep from the liquid-gel interface) (Fig. 3.4). In the dynamic measurements, p was monitored while lowering the microsensor 2 mm at constant speed between the pre-determined depths. The microsensor signal was sampled at 60 Hz. Oxygen tension was recorded in the same samples at 1 h and 46 h.

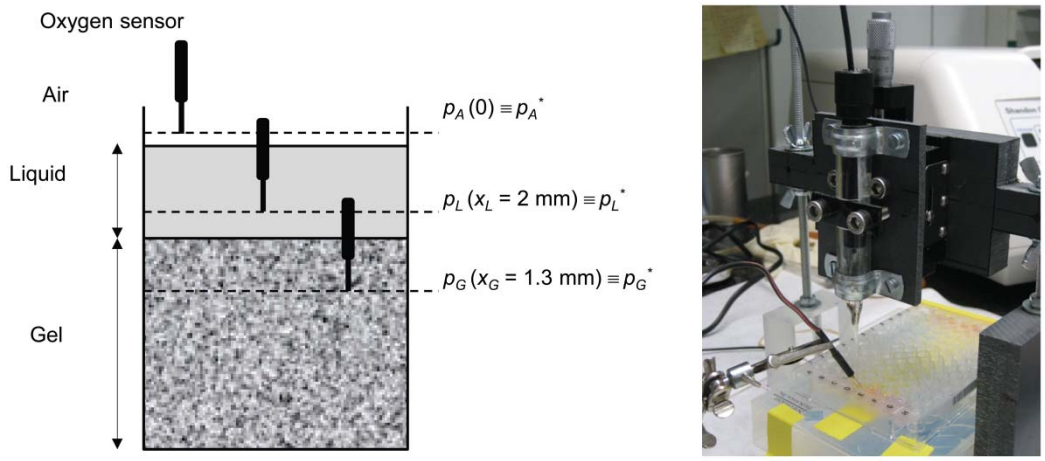

Fig 3.4 Left: Scheme of the experimental setup for measuring the oxygen partial pressure. Measurements of oxygen tension were taken in air, 2mm inside the medium and 1.3mm inside the 3D gel. Right: Actual experimental setup used for the oxygen tension measurements.

3.2.3 Analysis of dynamic oxygen tension measurements in acellular ECM gels

Dynamic measurements in acellular and cellular ECM gels were analyzed separately to assess oxygen diffusion and consumption, respectively. Dynamic p measurements in acellular gels were modeled with the one-dimensional (1D) Fick's law of diffusion by imposing the continuity of oxygen flux at both the air-liquid and liquid-gel interfaces as previously described [34, 62]. The equal oxygen flux condition can be expressed as:

$$-D_L \frac{dc_L}{dx_L} = -D_G \frac{dc_G}{dx_G} \tag{3.15}$$

where D is the oxygen diffusivity, c is the oxygen concentration, x is the depth within the specific layer, and the subindexes L and G refer to the liquid and gel layer, respectively. Solving Eq. (3.15) for D_G and expressing it in terms of p by using Henry's law ($c = k_H p$, where k_H is Henry's solubility constant) [42] yields

$$D_G = D_L \left| \frac{dp_L/dx_L}{dp_G/dx_G} \right| \frac{k_{H,L}}{k_{H,G}} \tag{3.16}$$

where $k_{H,L}$ and $k_{H,G}$ are Henry's constant for oxygen in the liquid and gel layer, respectively. Currently, $k_{H,G}$ of ECM gels have not been reported. However, it is

conceivable that the oxygen solubility in the interstitial fluid of ECM gels hydrated with culture medium is similar to that of plasma. The reported value for $k_{H,plasma}$ is 1.26×10^{-3} mol·m^{-3}·mmHg^{-1} [63], which is only 3% lower than the accepted value for $k_{H,L}$ = 1.3×10^{-3} mol·m^{-3}·mmHg^{-1} [35]. In these conditions, Eq. (3.16) can be approximated by

$$D_G \approx D_L \left|\frac{dp_L/dx_L}{dp_G/dx_G}\right| \tag{3.17}$$

Eq. (3.17) was used to assess D_G by taking the accepted value for D_L from the literature (3×10^{-5} cm^2/s) [35, 64], and calculating the slopes of p in either the liquid and gel layers in the dynamic measurements.

3.2.4 Analysis of dynamic oxygen tension measurements in 3D cultures

The balance between oxygen diffusion and consumption in hydrogels is commonly modeled with the 1D reaction-diffusion equation [34, 35]. Since the time-scale of the dynamic measurements was very small compared to the typical large time-scale of oxygen transport kinetics in hydrogels, the quasi-steady state approximation can be applied [6, 34]. In these conditions, the reaction-diffusion equation can be expressed in terms of p as

$$D_G^* \frac{\partial^2 p_G}{\partial^2 x_G^2} = \frac{R}{k_{H,L}} \tag{3.18}$$

where D_G^* is the diffusivity within the gel layer in the presence of cells, R indicates the oxygen consumption rate (OCR) per unit volume.

To quantify R, the Michaelis-Menten dynamics was used. Eq. (1.9) renders Eq. (3.18) non-linear. A common approximation to linearize Eq. (1.9) and obtain an analytical solution considers that R approaches its maximum value R_{max}, which corresponds to $K_m/k_{H,L} \ll p_G$ [34, 35]. In these conditions Eq. (3.18) becomes

$$D_G^* \frac{\partial^2 p_G}{\partial^2 x_G^2} \approx \frac{R_{max}}{k_{H,L}} \tag{3.19}$$

where $R_{max} = \rho_{cell} V_{max}$. On the other hand, the quasi-steady state approximation in the liquid layer is expressed as [34]

$$D_L \frac{\partial^2 p_L}{\partial^2 x_L^2} = 0 \tag{3.20}$$

To solve analytically Eq. (3.19) and Eq. (3.20), both the geometrical constraints of the experiments and the oxygen tension values measured in static conditions were considered, which elicited the following boundary conditions: (i) $p_L(x_L = 0) = p_A^{(\exp)}$, (ii) $p_L(x_L = 2\text{ mm}) = p_L^{(\exp)}$, (iii) $p_G(x_G = 0) = p_L(x_L = 2.7\text{ mm})$, and (iv) $p_G(x_G = 1.3) = p_G^{(\exp)}$. Applying boundary conditions (i) and (ii) to the analytical solution of Eq. (3.19) elicited

$$p_L(x_L) = 0.5\left(p_L^{(\exp)} - p_A^{(\exp)}\right)x_L + p_A^{(\exp)} \tag{3.21}$$

which is valid for $x_L \leq 2.7$ mm. Applying boundary conditions (iii) and (iv) to the analytical solution of Eq. (3.20) elicited

$$p_G(x_G) = \frac{R_{max}}{2k_{H,L}D_G^*}x_G^2 + \left(\frac{p_G^{(\exp)} - p_G(0)}{1.3} - \frac{0.65R_{max}}{D_G^*}\right)x_G + p_G(0) \tag{3.22}$$

where $p_G(0) = 1.35\left(p_L^{(\exp)} - p_A^{(\exp)}\right) + p_A^{(\exp)}$. Eq. (3.22) predicts a parabolic relationship between *p* and *x* at the gel layer in the 3D cultures. Accordingly, a parabolic function $p_G(x_G) = \mathrm{A}x_G^2 + Bx_G + C$ was least squares fitted to the dynamic $p_G(x_G)$ data recorded in cellularized gels (Mathematica, Wolfram Research, Inc.), and the fitting parameter *A* was used to assess R_{max}/D_G^* as

$$R_{max}/D_G^* = 2k_{H,L}A \tag{3.23}$$

Eq. (3.23) enables assessing R_{max}, provided that D_G^* is known. The diffusion hindrance or tortuosity due to cells (λ_{cell}) has been previously estimated both theoretically and experimentally, yielding an average value of 1.3 [19, 23]. The latter value along with D_G data obtained from Eq. (3.16) were used to assess $D_G^* = D_G/\lambda_{cell}^2$ [19, 23], thereby enabling the assessment of V_{max}.

Assessing the Thiele modulus, ϕ (Eq. 1.10), required a value for K_m for A549 cells, which are currently unreported. However, K_m values for other non-mesenchymal cells

like endothelial and hepatocytes are available elsewhere, and were averaged (K_m = 0.58×10^{-3} mol·m^{-3}, which corresponds to 0.45 mmHg) [34, 65, 66] and used in Eq. (1.10). Of note, among the different parameters in Eq. (1.10), only h and ρ_{cell} can be directly chosen when designing a 3D culture experiment.

3.2.5 Modeling conditions permissive of physiologic oxygen tension values in 3D cultures

A major challenge in 3D cultures is to mimic physiologic oxygen tension values, particularly within either the normoxic or hypoxic ranges. For this purpose, a quantitative estimation of how targeting a specific p value poses constraints in h and ρ_{cell} has been sought out. As a starting point, the latter task was carried out with a simple mathematical model based on recasting the quasi-steady state solution of the reaction-diffusion equation in terms of ϕ^2 and applying two general boundary conditions: (i) $p_G(x_G = 0) = p_G(0)$ and (ii) $|\partial p_G/\partial x_G|_{x_G=h} = 0$ as described elsewhere [6, 35]. In these conditions

$$p_G(x_G) = p_G(0) - \frac{K_m}{k_{H,L}}\phi^2\left[\frac{x_G}{h} - \frac{1}{2}\left(\frac{x_G}{h}\right)^2\right] \tag{3.24}$$

Solving Eq. (3.24) for ϕ, and imposing a specific oxygen tension limit (p_{limit}) yielded

$$\phi \leq \sqrt{\frac{p_G(0) - p_{limit}}{K_m/k_{H,L_G}}\frac{1}{\left[\frac{x_G}{h} - \frac{1}{2}\left(\frac{x_G}{h}\right)^2\right]}} \equiv \phi_{limit} \tag{3.25}$$

where ϕ_{limit} corresponds to the maximum ϕ consistent with either normoxic or hypoxic oxygen tension values –whose limits are defined by 50 or 10 mmHg in most tissues, respectively [29-31, 67] –at a specific gel depth. To assess the impact of ϕ_{limit} on h and ρ_{cell}, it must be born in mind that cell number typically increases in the presence of growth factors. As a first approximation, exponential growth has been assumed [62].

$$\rho_{cell}(t) = \rho_o e^{t/\tau} \tag{3.26}$$

where ρ_o is the initial seeding density and τ is a time constant describing the proliferation rate. Substituting Eq. (3.26) into Eq. (1.10) and expressing it in terms of ϕ_{limit} enabled assessing the maximum h and ρ_o permissive for either the normoxic or hypoxic values defined by ϕ_{limit} at a given time as

$$h_{max} = \sqrt{\frac{\phi_{limit}^2 K_m D_G^*}{\rho_o V_{max}} \mathrm{e}^{-t/\tau}} \tag{3.27}$$

$$\rho_{o,max} = \frac{\phi_{limit}^2 K_m D_G^*}{h^2 V_{max}} \mathrm{e}^{-t/\tau} \tag{3.28}$$

3.2.6 Statistical analysis

Two group comparisons were carried out using either Student's *t*-test or Mann-Whitney test for not normally distributed populations (SigmaPlot, Systat Software). Statistical significance was assumed at $P<0.05$. Unless otherwise stated, data are given as mean ± SE.

4 Results

Chapter 4 Results

In this chapter I will describe the results I have obtained during my Ph.D. thesis. Most of the results presented here are part of two papers. The results are organized into two subchapters, one regarding macromolecular diffusion, the other regarding oxygen diffusion and consumption. In terms of macromolecular diffusion, I first validated the macroscopic diffusivity assay. Second, by using the *D* data of this assay, I present the validity of the Stokes-Einstein relation in gels. Third, I analyze diffusivity in terms of the viscous friction between dextrans and the ECM gels, and in terms of the geometrical aspects of the gels. Forth, I present a theoretical prediction of the convenient time-windows in 3D cultures. In terms of oxygen diffusion and consumption, I first present the quantification of oxygen diffusion coefficients in gels. Second, I illustrate the oxygen tension values that arise in 3d cultures. Third, I present the quantification of several parameters related to oxygen consumption and diffusion. Finally, I describe how the tuning of several 3D culture parameters leads to physiologic oxygen tension values.

4.1 Diffusion of macromolecules

4.1.1 Validation of the macroscopic diffusivity assay

The macroscopic diffusivity of dextrans within a panel of ECM gels prepared in Transwell inserts was assessed with an optical assay based on a Microplate Reader. The maximum dextran equilibrium concentration in a gel containing Transwell plate was ~150 μg/ml, which fell within the linear intensity detection regime of the Microplate Reader as revealed by the measured fluorescence at different Dex4 concentrations shown in (Fig. 4.1A). The average F_{PR} data corresponding to the diffusion of Dex4, Dex40 and Dex70 in all sample conditions (SFM and ECM gels) are shown in (Fig. 4.1B), (Fig. 4.1C) and (Fig. 4.1D) respectively, where F_{PR} were normalized to the maximum fluorescence recorded on SFM. A monotonic increase of normalized F_{PR} with time was observed even in the fastest diffusivity conditions, thereby supporting the feasibility of the experimental approach. F_{PR} data were analyzed with two models with increasing computational complexity: a semi-infinite gel model that has an analytical solution Eq. (3.2), and a finite-gel model Eq. (3.12). The fittings of both models on measurements obtained with Dex4, Dex40 and Dex70 are shown in (Fig. 4.1B), (Fig. 4.1C) and (Fig. 4.1D) respectively. Both models captured the dynamics of the intensity

data in the experimental time-window ($r^2 \geq 0.95$ for semi-infinite model, $r^2 \geq 0.92$ for the finite model), supporting that transport was largely driven by passive diffusion, and confirming that the working dextran concentration was a dilute solution. The LMA-based fitting method was numerically unstable for conditions where *Dg* is close to *Do* due to divergences arising in the denominator of Eq. (3.12), which corresponds to either Dex4 diffusing in any of the gels or both Dex40 and Dex70 diffusing within sparse COLI gel.

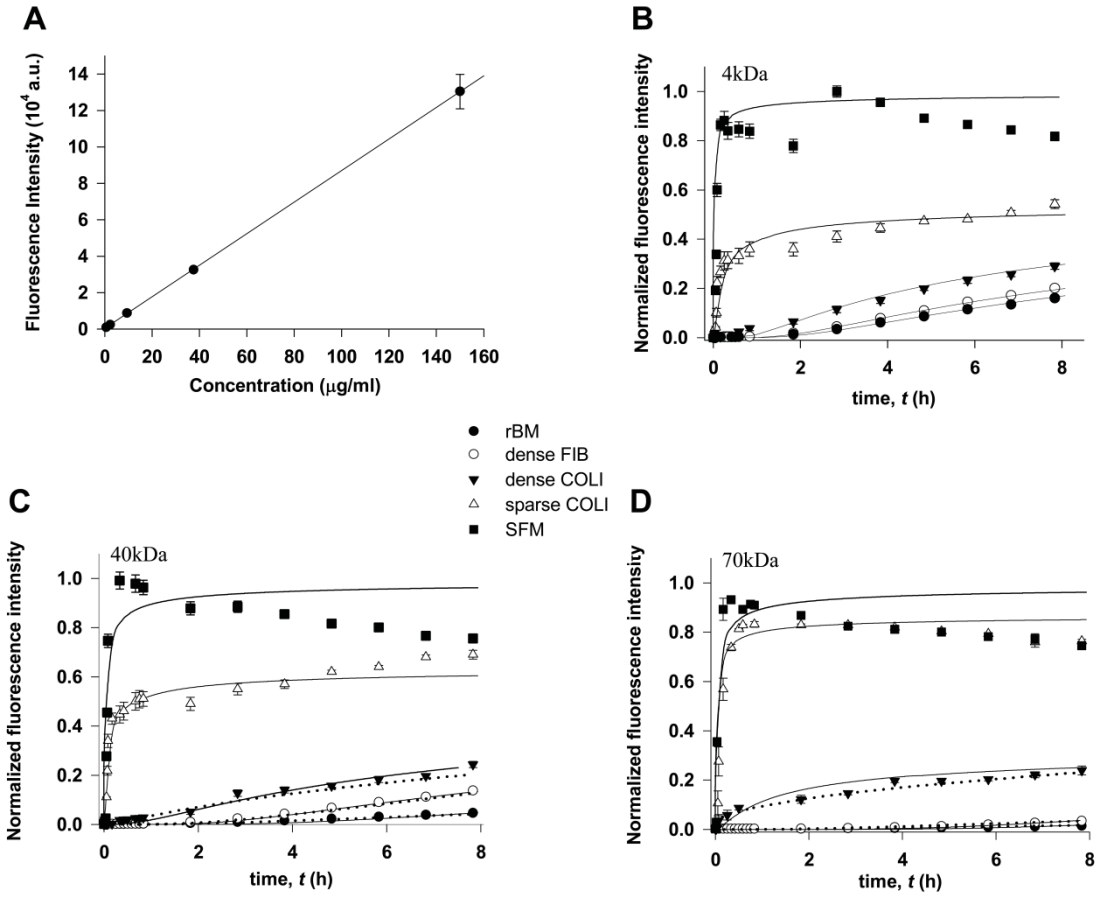

Fig. 4.1. Validation of the macroscopic diffusivity assay. (A) Average fluorescence recorded with the Microplate Reader at different Dex4 concentrations *C*, including the maximum *C* used in this study (n = 2). Continuous line indicates a linear regression fitting (r^2 = 0.99). Fluorescence of (B) Dex4, (C) Dex40, (D) Dex70 in the lower Transwell compartment measured with a Microplate Reader as a function of time in a panel of ECM gels. Fluorescence data were normalized to the maximum fluorescence measured in SFM. Continuous lines correspond to the fittings of the semi-infinite model Eq. (3.2) while dotted lines correspond to the fittings of the finite model Eq. (3.12). The effective *D* was a fitting parameter (n = 3) in both cases. All data shown in (Fig. 4.1) and subsequent figures are mean ± SE unless otherwise indicated.

The *Dg* data obtained using the finite model exhibited very good correlation with the corresponding values obtained with the semi-infinite model (R = 0.85). In addition, these data could be fitted with a linear function with slope close to unity (*Dfinite* = 1.16 *Dsemi-infinite*) (Fig. 4.2A).

Likewise, l values obtained from the fittings of the two models were very close to the theoretical 2 mm in all conditions examined except sparse COLI.

Gel	*Semi-infinite model Thickness(cm)*	*Finite model Thickness(cm)*
	4kDa	
rBM	$(2.0 \pm 0.4)\ 10^{-1}$	$(2.0 \pm 0.1)\ 10^{-1}$
dense FIB	$(2.0 \pm 0.2)\ 10^{-1}$	$(2.0 \pm 0.1)\ 10^{-1}$
dense COLI	$(1.9 \pm 0.3)\ 10^{-1}$	$(1.2 \pm 0.4)\ 10^{-1}$
sparse COLI	$(3.9 \pm 0.3)\ 10^{-2}$	
	40kDa	
rBM	$(1.9 \pm 0.4)\ 10^{-1}$	$(1.8 \pm 0.3)\ 10^{-1}$
dense FIB	$(2.0 \pm 0.1)\ 10^{-1}$	$(1.8 \pm 0.4)\ 10^{-1}$
dense COLI	$(1.9 \pm 0.2)\ 10^{-1}$	$(1.5 \pm 0.1)\ 10^{-1}$
sparse COLI	$(2.0 \pm 0.5)\ 10^{-2}$	
	70kDa	
rBM	$(2.0 \pm 0.4)\ 10^{-1}$	$(1.3 \pm 0.2)\ 10^{-1}$
dense FIB	$(2.0 \pm 0.2)\ 10^{-1}$	$(1.5 \pm 0.3)\ 10^{-1}$
dense COLI	$(2.0 \pm 0.3)\ 10^{-1}$	$(1.0 \pm 0.4)\ 10^{-1}$
sparse COLI	$(1.6 \pm 0.5)\ 10^{-2}$	

Table I: l values obtained from the fittings of the semi-infinite and finite models respectively.

Given the strong agreement between both models, ***D* data obtained with the simpler semi-infinite model has been used in subsequent analyses**. *D* data were first validated by comparing *D* assessed in SFM (D_{SFM}) with the theoretical values computed with the Stokes-Einstein law (D_o). Both D_{SFM} and D_o values exhibited a marked linear relationship (r^2 = 0.99) (Fig. 4.2B). The macroscopic diffusivity assay was further validated by comparing *D* of Dex4 obtained in each ECM gel with the corresponding diffusivity obtained with FRAP (D_{FRAP}) (Fig. 4.2C). Illustrative FRAP measurements in dense FIB and their corresponding curve fittings of Eq. (3.13) are shown in (Fig. 4.2D) Despite the marked differences in sample preparation and measurement technique, a good qualitative and quantitative agreement was observed between macroscopic *D* and microscopic D_{FRAP} data, as revealed by their marked linear relationship ((r^2 = 0.9).

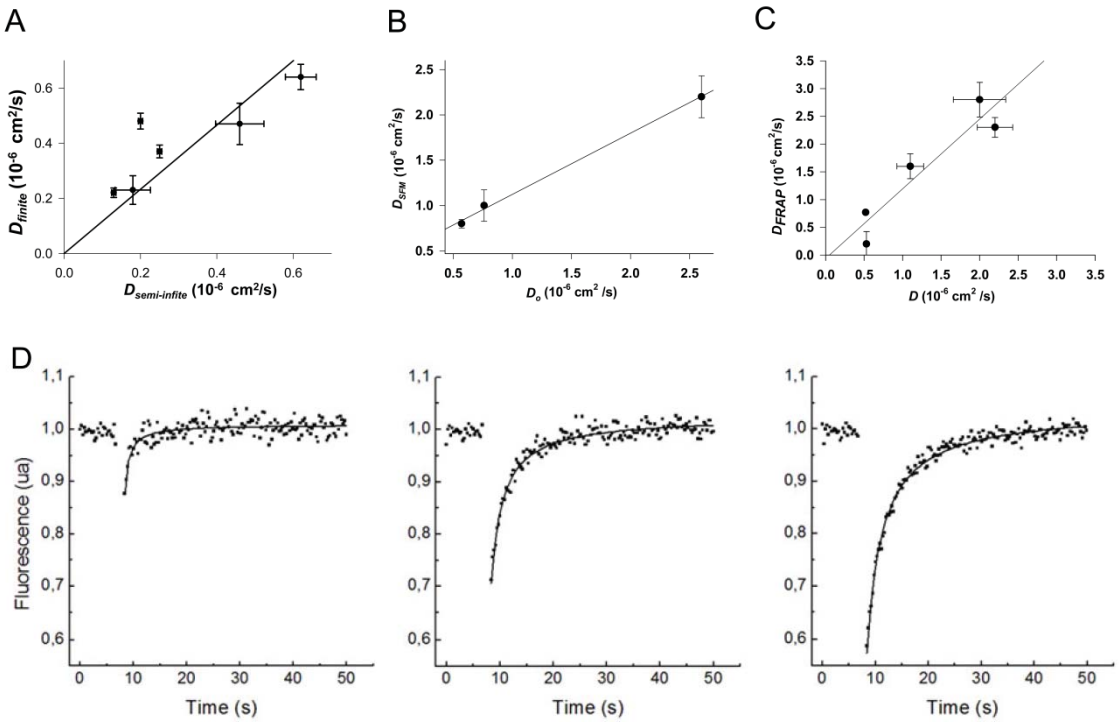

Fig. 4.2. Validation of the macroscopic diffusivity assay (A) Scatter plot showing *D* data obtained with either the semi-infinite or the finite gel models on the measurements shown in Fig. 4.1B,C,D. Continuous line indicates a linear regression fitting (r^2 =0.9). (B) Comparison between the experimental D_{SFM} of all dextrans and the corresponding theoretical prediction *Do* assessed with the Stokes-Einstein law. (C) Diffusivity data for Dex4 assessed in the panel of ECM gels with either the macroscopic assay or FRAP (n = 6). (D) Representative FRAP measurements obtained with Dex4, Dex40 and Dex70 in dense FIB gels. The continuous lines correspond to the fitting of Eq. (3.13).

4.1.2 Diffusion hindrance in ECM gels is consistent with Stokes-Einstein law

D data of all FITC-dextrans examined in the panel of ECM gels are shown in (Fig. 4.3A). In all gels, *D* decreased monotonically with M_r. A decrease of *D* with M_r in free solution has been previously described in terms of power-laws ($D=aM_r^{-\alpha}$) with a weak exponent $\alpha \sim 0.15$-0.5 that depends on the geometry and flexibility of the diffusing particle [19, 68]. A power-law to D_{SFM} data has been curve-fitted and $\alpha = 0.35 \pm 0.01$ ($r^2 = 0.99$) was obtained, in agreement with the 1/3 values predicted by the classical Stokes-Einstein relation for rigid spherical particles diffusing through an ideal

Newtonian fluid [56]. To test whether a similar mathematical description could be applied to D data obtained in gels, a power-law with a common exponent was fitted simultaneously to all gels. The fittings exhibited a very good agreement with the experimental data ($r^2 = 0.99$), and are shown in (Fig. 4.3A) (continuous lines). Fitting parameters were $\alpha = 0.33 \pm 0.02$ (unitless), $D = (0.73 \pm 0.20)\times10^{-5}M_r^{-\alpha}$ for rBM, $D = (0.79 \pm 0.21)\times10^{-5}M_r^{-\alpha}$ for dense FIB, $D = (1.79 \pm 0.43)\times10^{-5}M_r^{-\alpha}$ for dense COLI, and $D = (2.97 \pm 0.70)\times10^{-5}M_r^{-\alpha}$ for sparse COLI, where the units of D and M_r are cm^2/s and Da, respectively. Unexpectedly, the fitted exponent α matched the 1/3 value predicted by the Stokes-Einstein relation in free solution [56]. These findings confirm previous observations that dextrans diffuse as spheres [19, 22, 69] , and suggest that diffusion hindrance is largely due to viscous friction with the extracellular space (ECS) fluid.

Gel tortuosity data, λ_{gel} ,from D data have been assessed taking D_o shown in (Fig. 4.2B) as D_{free}. The results are shown in (Fig. 4.3B), and revealed $\lambda_{gel} \geq 1.4$ for all gel densities $\geq$ 3 mg/ml in all dextrans, whereas λ_{gel} values in sparse COLI (1 mg/ml) were comparable to 1, which is indicative of very weak hindrance (i.e. diffusivity comparable to free solution). Intriguingly, λ_{gel} of dense FIB was more than 1.5-fold larger than that of dense COLI at the same density for all M_r, whereas it was comparable to λ_{gel} of rBM despite the fact that rBM was 3-fold more dense than FIB. These findings reveal that knowing gel density alone is not sufficient to predict diffusion hindrance.

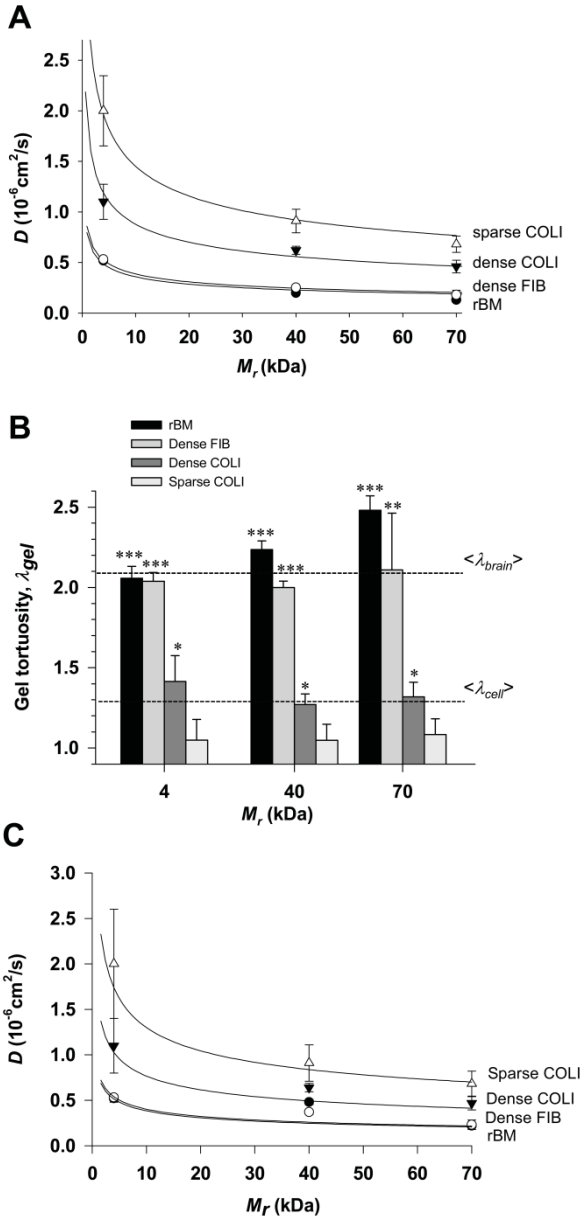

Fig. 4.3. Macroscopic diffusivity measurements assessed for different M_r in a panel of ECM gels. (A) D data as a function of M_r for each ECM gel (n = 3). Continuous lines correspond to the simultaneous fitting of a power-law with a fixed exponent for all gels, being the exponent a fitting parameter. (B) λ_{gel} values calculated from D and D_{SFM} data shown in (A) and (Fig. 4.2B), respectively. Horizontal lines indicate the average λ values reported from cells alone or in the extreme physiologic hindrance conditions of the brain tissue. *P<0.05, **P<0.01 and ***P<0.005 were determined by Student's t-test with respect to sparse COLI. (C) Macroscopic diffusivity measurements assessed for different M_r in a panel of ECM gels (n = 3) obtained with both the finite and the semi-infinite models. D data for Dex40 and Dex70 were obtained with the finite gel model on rBM, dense FIB and dense COLI. All other D data were obtained with the semi-infinite model. Continuous lines correspond to the simultaneous fitting of a power-law with a fixed exponent for all gels ($D_g \sim M_r^{-\alpha}$), being the exponent a fitting parameter.

As a guidance to interpret λ_{gel} data in terms of physiological hindrance, the average λ values attributable to cellular obstacles alone ($<\lambda_{cell}>$=1.3 (1.1-1.5)) [19, 22-25] have been plotted in (Fig. 4.3B) alongside the average λ of dextrans measured in brain tissue elsewhere ($<\lambda_{brain}>$= 2.1 (1.6-2.7)) [19, 26], which is considered among the most geometrically restrictive tissues in terms of diffusion.

This comparison revealed that λ_{gel} values measured in both rBM and dense FIB were at least 1.5-fold larger than $<\lambda_{cell}>$, and fell within the same range as λ_{brain} data.

4.1.3 Diffusivity analysis in terms of viscous friction between dextrans and the ECM gel

A major assumption of the Stokes-Einstein law is that passive transport is regulated by the friction of the diffusing particle with the viscosity of the surrounding media. We used D data to assess the effective macroscopic viscosity η of each ECM gel by averaging η obtained with different dextrans (Fig. 4.4A). The horizontal dashed line is the water viscosity (η_{water}) at 37ºC and was added as a reference. The maximum η values were obtained in rBM and dense FIB, and were ≥ 3.5-fold larger than that of water. Conversely, η of sparse COLI was similar to η_{water}, whereas η of dense COLI was ~2-fold larger than η_{water}. To confirm that η of dense FIB was comparable to rBM rather than dense COLI, the effective viscosity ($\eta_{AFM}(f)$) of these gels was assessed using an independent approach based on microrheology measurements by AFM (Fig. 4.4B). Sparse COLI was too soft for a robust assessment of microrheological properties by AFM. We observed that η_{AFM} were ≥ 2 orders of magnitude larger than η values obtained from D data. Yet, in agreement with η data, η_{AFM} of rBM and dense FIB were comparable and larger than that of dense COLI for all f examined. These results revealed that the viscosity of ECM gels is predictive of the diffusion hindrance of dextrans with physiological M_r values. A linear relationship between the normalized viscosity data (η/η_{water}) obtained in COLI and rBM gels and d was observed (Fig 4.4C).

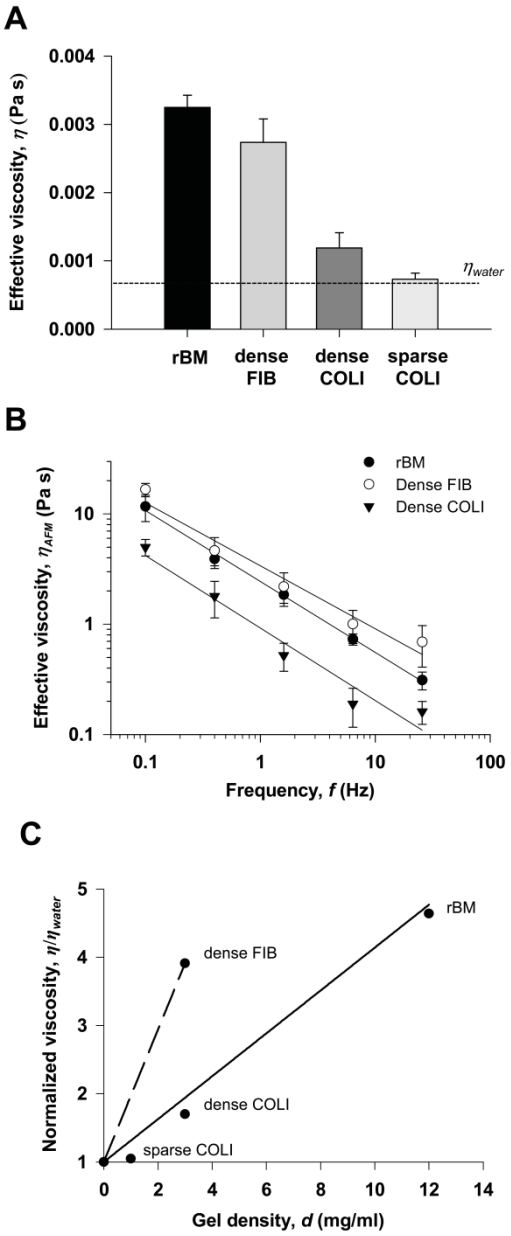

Fig. 4.4. Effective viscosity in a panel of ECM gels. (A) η calculated using the Stokes-Einstein law and D data shown in Fig. 4.3A, and averaged for all M_r for a given gel (n = 3). The dashed horizontal line represents water viscosity at 37ºC. (B) Effective viscosity assessed by AFM oscillatory measurements as a function of f (n = 9, 2 replicates). Note the different vertical scale between (A) and (B). (C) Normalized viscosity of scaffolds with respect to water plot against the gel density highlighting the linear relationship between COLI and rBM.

4.1.4 Diffusivity analysis in terms of geometrical aspects of ECM gels

A critical geometrical parameter of ECM structure in terms of diffusion is its average pore width (w), since ECM-dependent tortuosity is thought to be more relevant as the size of the diffusing molecule increases with respect to w [19, 28]. There is currently no standard method to measure w, although most studies use either direct assessments by image analysis of ECM structure or indirect assessments from permeability measurements [18, 70]. In this work we chose the former approach by using AFM to image the surface topography of ECM gels prepared with a thickness comparable to that used in diffusivity measurements. All gels could be imaged with the exception of sparse COLI, which was too compliant to withstand the tip-sample dragging forces that arise during scanning. A representative image obtained in dense COLI is shown in (Fig. 4.5A). Although ECM filaments were somewhat distorted by the lateral forces developed in the scanning direction (right to left), they remained stable enough to enable identifying pores as surface invaginations, which correspond to the black regions in the image (Fig. 4.5A). Subsequent image analysis revealed a log-normal distribution of pore areas (Fig. 4.5B, 4.5C, 4.5D), which were used to calculate w data shown in (Fig. 4.5E). At least 85 pores were examined in each gel type. Although the manual image analysis could have lead to either under- or over-estimations of the actual pore widths, it is conceivable that such under- and over-estimations were balanced given the large number of pores examined. For completeness' sake, w values of sparse COLI reported elsewhere [70-74] were shown in (Fig. 4.5E). A general reduction of the median w values with gel density has been found. However, unlike diffusivity, the w range for dense FIB was closer to that of dense COLI than to rBM. This data also indicate that the median w were more than 100-fold larger than R_H of dextrans, even at the highest gel density. These results reveal that ECM geometry alone is not sufficient to predict λ_{gel}, and indicate that dextrans spend most of their time in contact with the ECS fluid.

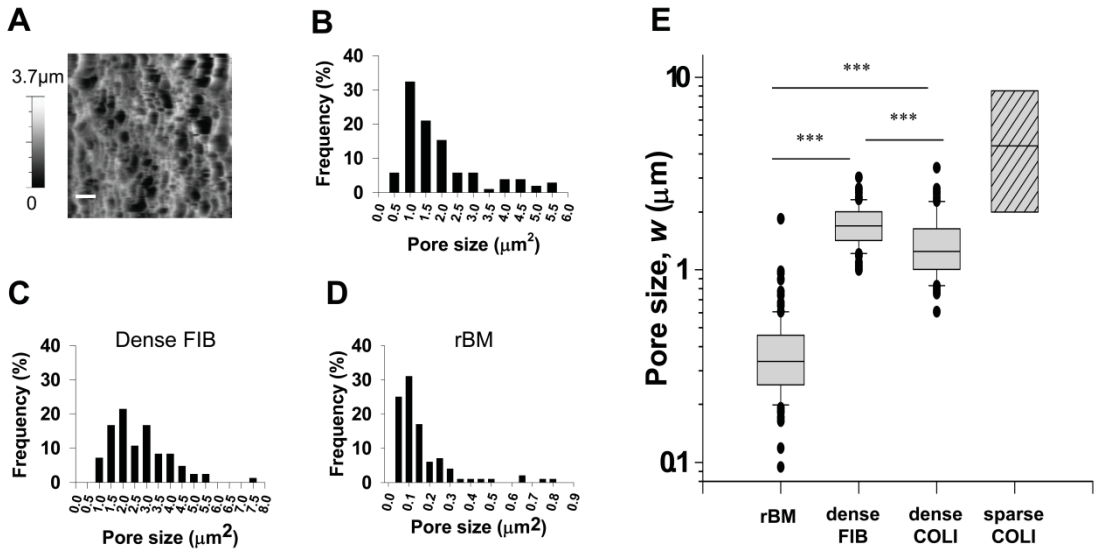

Fig. 4.5. Pore sizes of ECM gels in liquid assessed by AFM imaging in contact mode. (A) Representative topographic AFM image of the surface of a dense COLI gel. Scale bar corresponds to 5 µm (B) COLI, (C)dense FIB, (D) rBM Frequency distribution of pore areas outlined in the AFM images. (E) Log-scale box-plot of pore sizes calculated from AFM images assuming a circular geometry (n ≥ 85). Data of sparse COLI gels were taken from elsewhere [45-49]. ***P<0.005 were determined by Mann-Whitney test.

4.1.5 Convenient time-windows in 3D culture experiments based on diffusivity data

A common application of 3D cultures is examining the cellular response to an exogenous signaling soluble factor. Because of diffusion hindrance, the concentration of any soluble factor will reach equilibrium at a time much longer than in cell cultures in standard two-dimension tissue culture plastic (2D culture). Therefore, diffusion sets a minimum time-window that must be contemplated to guarantee that all cells in a 3D culture are exposed to the same equilibrium concentration of the signaling factor. To assess a convenient time-window, the time to reach half the equilibrium concentration t_{50} due to either λ_{gel} alone (ECM) or to the combined effect of gels and cells as in 3D cultures (ECM+cells) was calculated (Fig. 4.6). The latter tortuosity was assessed as $\lambda_{3D} \approx \lambda_{gel}\lambda_{cell}$ as reported elsewhere [19, 22, 24, 68, 69], where λ_{cell} was taken as 1.3, which elicited $t_{50,ECM+cells}$= 1.69 $t_{50,ECM}$. Plots of t_{50} as a function of gel thickness for all the M_r and gel types examined are shown in (Fig. 4.6A-D). For the ~2 mm thick gels used in

the macroscopic diffusivity assay, t_{50} due to ECM was ~3-4 days for the largest M_r in rBM and dense FIB, whereas it was < 1 day for COLI gels. These values almost doubled when considering the effect of λ_{cell}, indicating that considering λ_{gel} alone underestimates markedly the predicted t_{50} in 3D cultures.

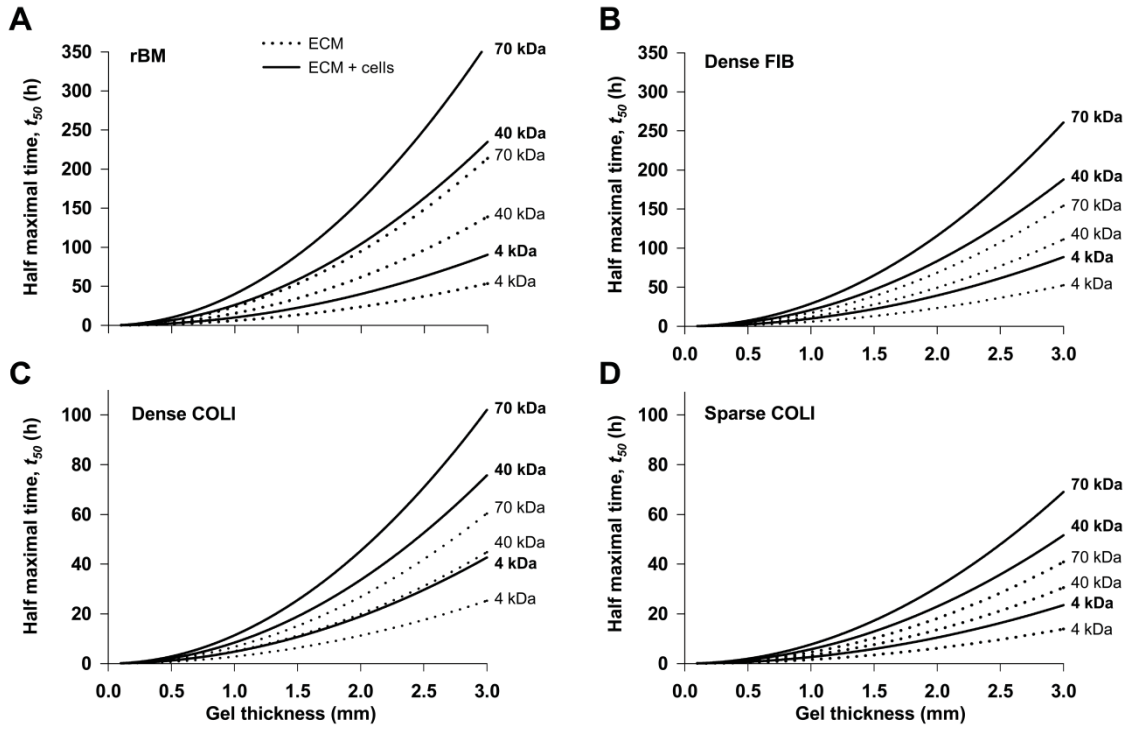

Fig. 4.6. Theoretical minimum experimental time-windows in 3D culture experiments as a function of gel thickness. t_{50} values were assessed as $t_{50} = l^2\lambda^2/(1.69D_o)$ using either λ_{gel} alone (dotted lines) or $\lambda_{3D} \approx \lambda_{gel}\lambda_{cell}$, taking $\lambda_{cell} = 1.3$ (continuous lines) for rBM (A), dense FIB (B), dense COLI (C) and sparse COLI (D). For clarity purposes, a different vertical scale between (A,B) and (C,D) has been used.

Another way of assessing a characteristic diffusion time is by extracting the time from the diffusion distance equation in 2D, $x^2=4Dt$. This estimation is useful, as it gives insight into the time scale of the earlier stages of the diffusion process.

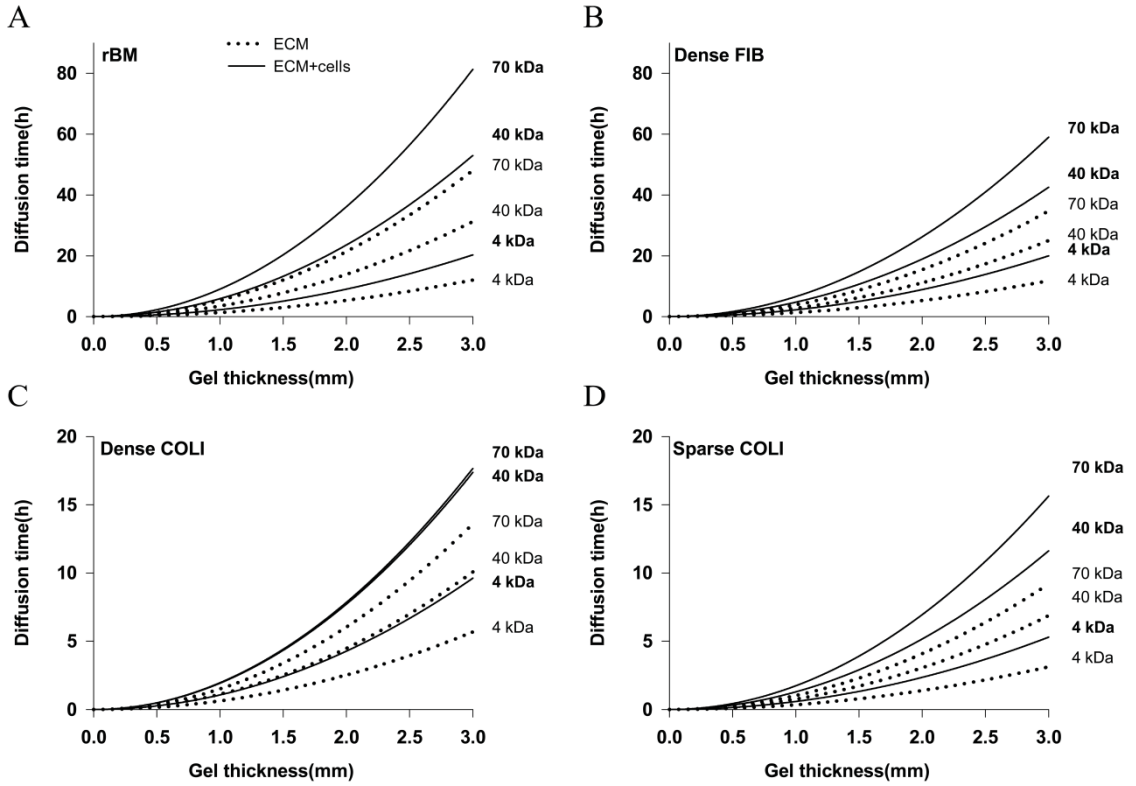

Fig 4.7. Theoretical minimum experimental time-windows in 3D culture experiments as a function of gel thickness. Times were assessed as $t=x^2/4D_0$ using either λ_{gel} alone (dotted lines) or $\lambda_{3D} \approx \lambda_{gel}\lambda_{cell}$, taking $\lambda_{cell} = 1.3$ (continuous lines) for rBM (A), dense FIB (B), dense COLI (C) and sparse COLI (D). For clarity purposes, a different vertical scale between (A,B) and (C,D) has been used.

4.2Oxygen diffusion and consumption in 3D cultures

4.2.1 Hindered oxygen diffusion in acellular ECM gels

An illustrative example of p measurements performed at 1h in an acellular rBM gel is shown in (Fig. 4.8B). Two small but detectable drops in p appeared at the interfaces between air-liquid and liguid-gel layers. Comparable drops were observed in the other acellular ECM gels. The drop in p_L^* with respect to p_A^* was expected, according to the oxygen solubility in the culture medium [35]. The drop in p_G^* indicated that oxygen concentration in the ECM gels was slightly lower than that in the culture medium. Despite these small drops, oxygen tension was much higher than the normoxic limit –indicated by the horizontal dashed line (Fig. 4.8B)– in all acellular gels. To examine

whether the small drop of p in the gel layer could be due to hindered diffusion in the ECM gels, D_G from the dynamic measurements in acellular gels was assessed. D_G was smaller than D_L in all gels, although these reductions attained statistical significance in rBM and dense FIB only (Fig. 4.8C). A possible explanation for the similar reduced diffusivity in rBM and dense FIB could be their comparable viscosities [75]. To test this possibility, the theoretical oxygen diffusivity (D_o) in gels and in water was calculated using the Stokes-Einstein relation $D_o = k_B T/6\pi\eta R_H$, where k_B is the Boltzmann's constant, T is the absolute temperature (310 ºK), R_H is the oxygen hydrodynamic radius, and η is the gel viscosity. R_H was taken as the bond length (0.12 nm) [76], whereas η values were taken from data reported elsewhere [75]. D_G exhibited a marked linear relationship with D_o (Fig. 4.8D), r^2=0.9, thereby supporting that hindered diffusion in ECM gels is mainly due to oxygen viscous friction with the extracellular space (ECS) fluid.

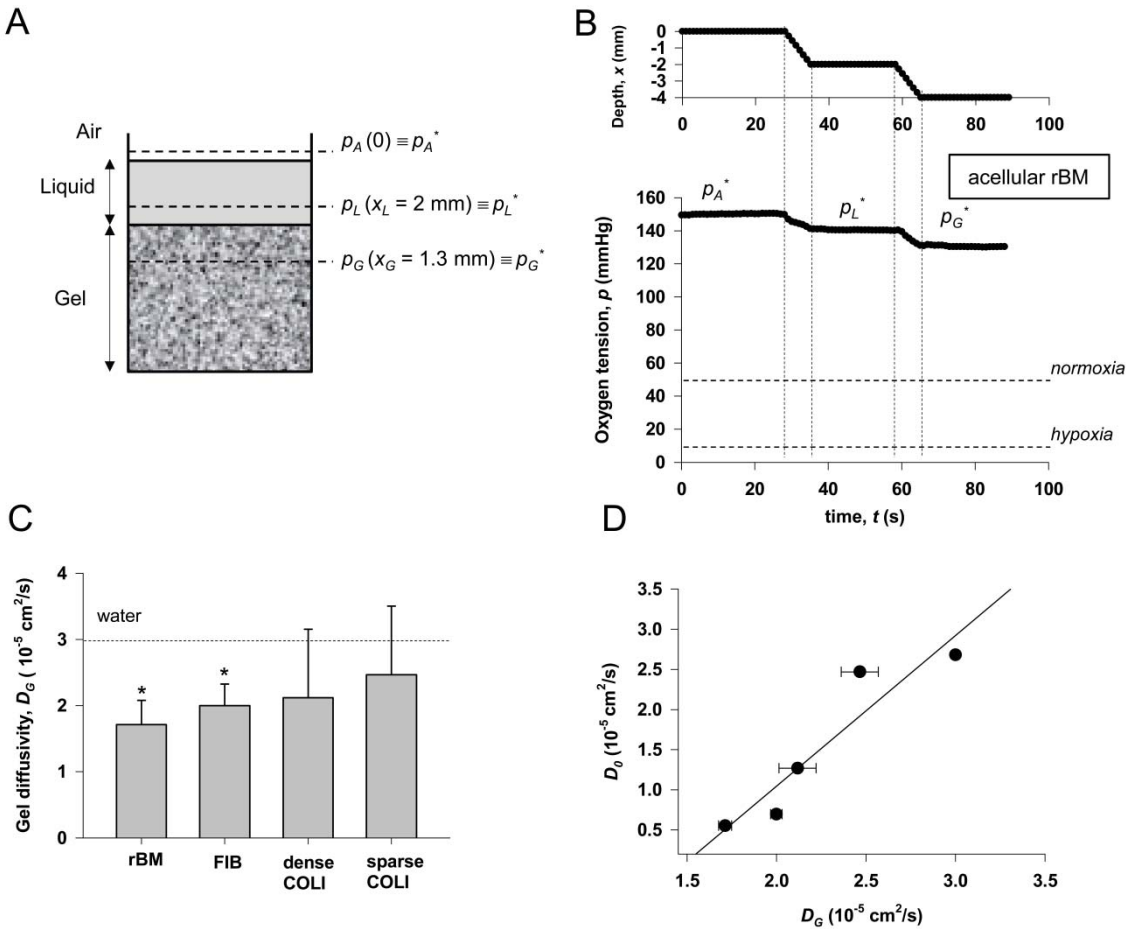

FIG 4.8 (A) Schematic representation of the geometry of p measurements in the 3 material layers found in 3D cultures: air, liquid and ECM gel. (B) Representative example of p measurements in an acellular rBM gel (bottom panel). The corresponding expected positions of the oxygen sensor are shown in the top panel. The average sensor speed in the dynamic measurements was 0.32 ± 0.04 mm/s. (C) Gel diffusivity in acellular ECM gels (n = 3). *P<0.05 with respect to water. (D) Scatter plot of experimental D_G and theoretical D_o gel diffusivities. Theoretical values were assessed with Stokes-Einstein law as described in the text. Continuous line represents a linear regression fitting (r^2 = 0.9).

4.2.2 Physiologic oxygen tension arises in 3D cultures in dense but not sparse ECM gels

Examples of p measurements at 1 h and 46 h recorded in 3D cultures in rBM or in 2D cultures are shown in (Fig. 4.9A) and (Fig. 4.9B), respectively. As expected, the drops in p_G^* with respect to p_L^* observed in (Fig. 4.9A) were larger than those in acellular gels owing to the cell-dependent effects on hindered diffusion and oxygen consumption. The

drop in p_G^* with respect to p_L^* in cellularized rBM was larger at 46 h, and reached the normoxic/hypoxic range (Fig. 4.9A). The average values of p_L^* in cellularized gels recorded a drop from 1h to 46h, but have remained within the hyperoxic range (Fig 4.9C). In contrast, the average p_G^* data at 46 h fell within the physiologic range in all other dense gels (≥ 3 mg/ml), but not in sparse COLI gels, which remained ~ 70 mmHg (Fig. 4.9D). In contrast, p_L^* values in 2D remained well above the normoxic range, even though they dropped with respect to p_A^* (Fig. 4.9B,D). These results indicate that 3D cultures with dense ECM gels were suitable tissue surrogates after 46 h in terms of oxygen tension, whereas both 2D cultures and 3D cultures in sparse COLI were not.

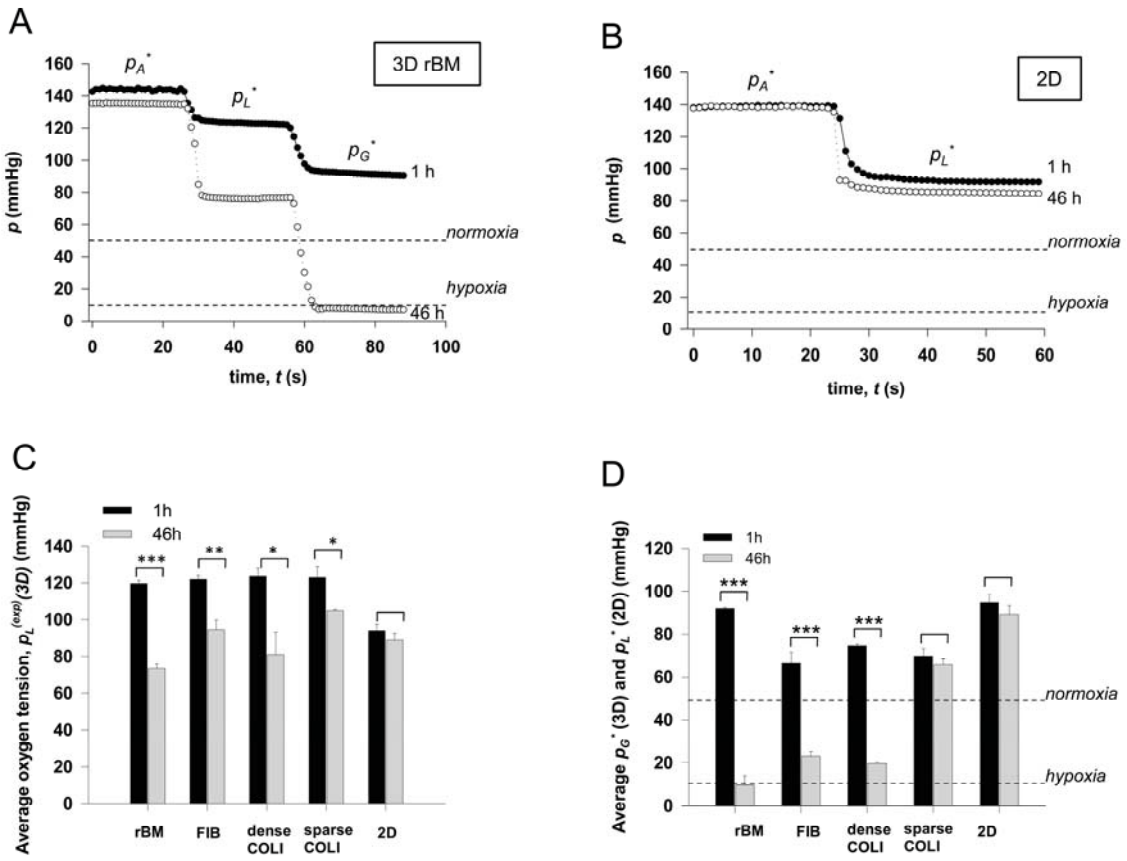

FIG 4.9. Oxygen tension measurements in 3D cultures with A549 cells. Representative measurements in cellularized rBM gels (A) or 2D cultures (B) at 1 h (black dots) and 46 h (white dots). (C)Average p_L^* values recorded in static conditions in 3D cultures(medium above gel), at1h(black bars) and 46h(gray bars)(D) Average p_G^* and p_L^* values recorded in static conditions in 3D and 2D cultures, respectively, at 1h (black bars) and 46h (gray bars). ***P<0.005 with respect to 46h. Horizontal dashed lines correspond to physiologic limits of normoxia and hypoxia.

4.2.3 Oxygen consumption of A549 cells cultured within a panel of ECM gels

To gain quantitative insight into oxygen consumption in 3D cultures, the dynamic p_G measurements were replotted as a function of x_G and fitted to Eq. (3.22). A representative example of $p_G(x_G)$ data obtained with A549 cells cultured in rBM for 46 h and the corresponding fitting are shown in (Fig. 4.10A). As expected, $p_G(x_G)$ data conformed well to a parabolic curve in all samples ($r^2 \geq 0.9$). The latter analysis enabled assessing R_{max} at 1 h and 46 h (Fig. 4.10B), which was indicative of the total oxygen consumption 1.3 mm deep in the gels. The highest R_{max} values were consistently observed in 2D cultures, and were more than two-fold larger than the lowest R_{max} values obtained in rBM and dense FIB, whereas the data range observed in COLI gels was intermediate between the latter gels and 2D. Also, R_{max} increased with time in both 2D and 3D cultures with the exception of sparse COLI, suggesting a COLI density-dependent effect in A549 cells. On the other hand, the estimations of D_G^* yielded 1.01×10^{-5} for rBM, 1.18×10^{-5} for dense FIB, 1.25×10^{-5} for dense COLI, and 1.46×10^{-5} cm^2/s for sparse COLI. Considering these D_G^* values and R_{max} data (Fig. 4.10B) allowed assessing ϕ. These calculations revealed that the oxygen consumption rates were ~10-16-fold larger than diffusion rates in all 3D cultures at 1 h, with a little increase (up to ~14-16-fold) at 46 h in all gels but sparse COLI. Likewise, R_{max} and the initial ρ_{cell} enabled calculating V_{max} at 1 h in 3D (Fig. 4.10C). V_{max} in 2D was assessed considering the molar flow rate of oxygen normalized by the seeding density as described elsewhere [34]. V_{max} in 2D was similar to that in COLI gels, and two-fold larger than in rBM or dense FIB. The latter observation revealed a marked effect of ECM biochemistry over gel density in oxygen consumption, since dense FIB and dense COLI had the same gel density and yet the V_{max} in dense FIB doubled that of dense COLI. Thiele moduli for all gels were calculated using the initial cell density values of 0.8M cells/ml (Fig.4.10D). Values were considered for a very wide gel thickness range.

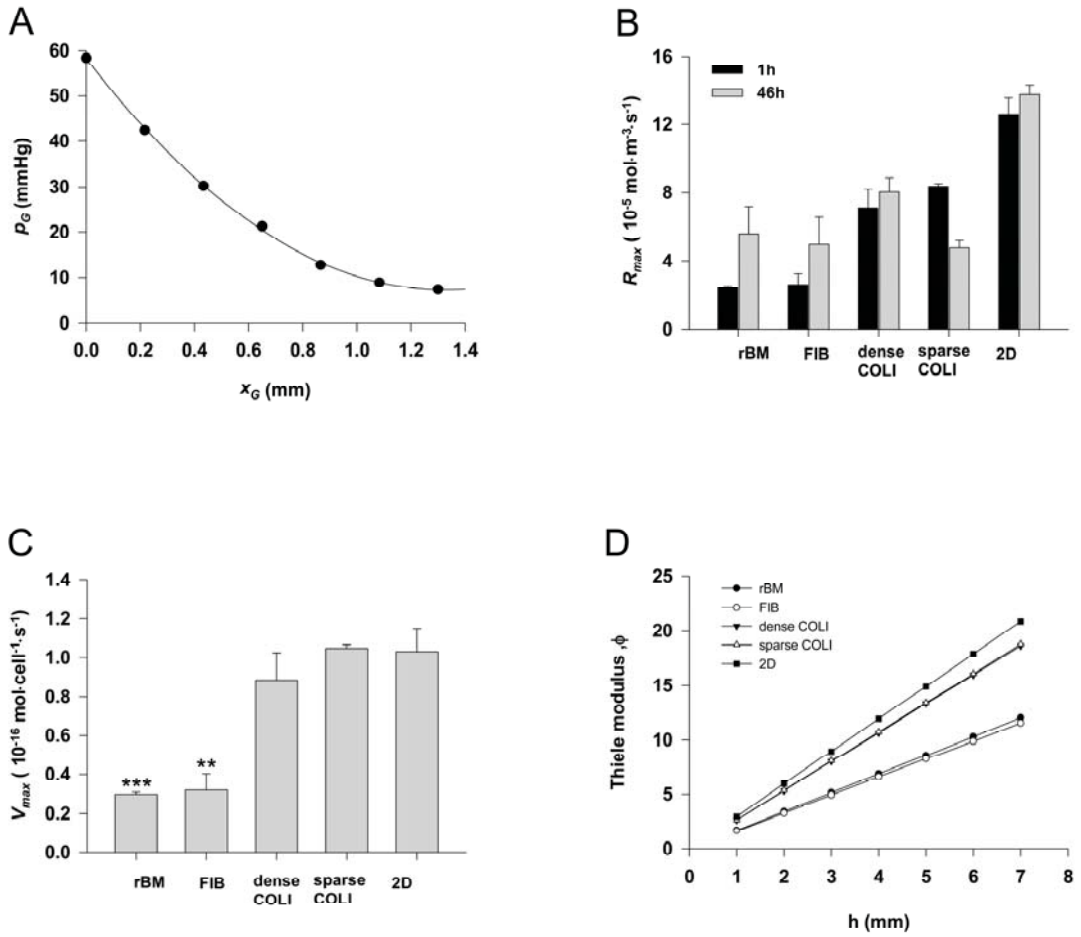

FIG 4.10. (A) Illustrative example of dynamic p measurements at different gel depths in a 3D culture with rBM. Continuous line represents a least squares fitting (r^2 = 0.99). (B) Average maximum OCR measured at 1 h (black bars) and 46 h (gray bars) in 3D and 2D cultures. (C) Corresponding maximum OCR per cell at 1 h. $^{**}P<0.01$ and $^{***}P<0.005$ with respect to 2D. (D) Thiele moduli calculated for all gels at a seeding density of 0.8M cells/ml spanning over a gel thickness range of 7mm.

4.2.4 Modeling p_G, h, and ρ_{cell} permissive of physiologic oxygen tension in 3D cultures with A549 cells

As a first approximation, a simple analytical model described in Equations (3.27-3.28) was used to assess the oxygen pressure in the middle of the gel and predict h_{max} and $\rho_{o,max}$ permissive for either normoxia or hypoxia in 3D cultures with A549 cells. All the input variables of the model could be assessed directly from the experiments but K_m *and* K_H, which were taken from the literature. τ was assessed considering ρ_o and ρ_{cell} at 46 h,

which was estimated holding V_{max}, thereby eliciting 54 h for rBM, 73 h for dense FIB, 360 h for dense COLI and -81h for sparse COLI. Imposing p_{limit} for normoxia (50 mmHg) or hypoxia (10 mmHg) at half the gel thickness (x_G/h = 0.5) elicited ϕ_{limit} ~ 19 and 24 for all gels, respectively. In these conditions, the evolution of pressure at the middle of the gel (2mm or 4mm thick) was assessed during a timespan of one week, for different cell seeding densities (Fig.4.11).

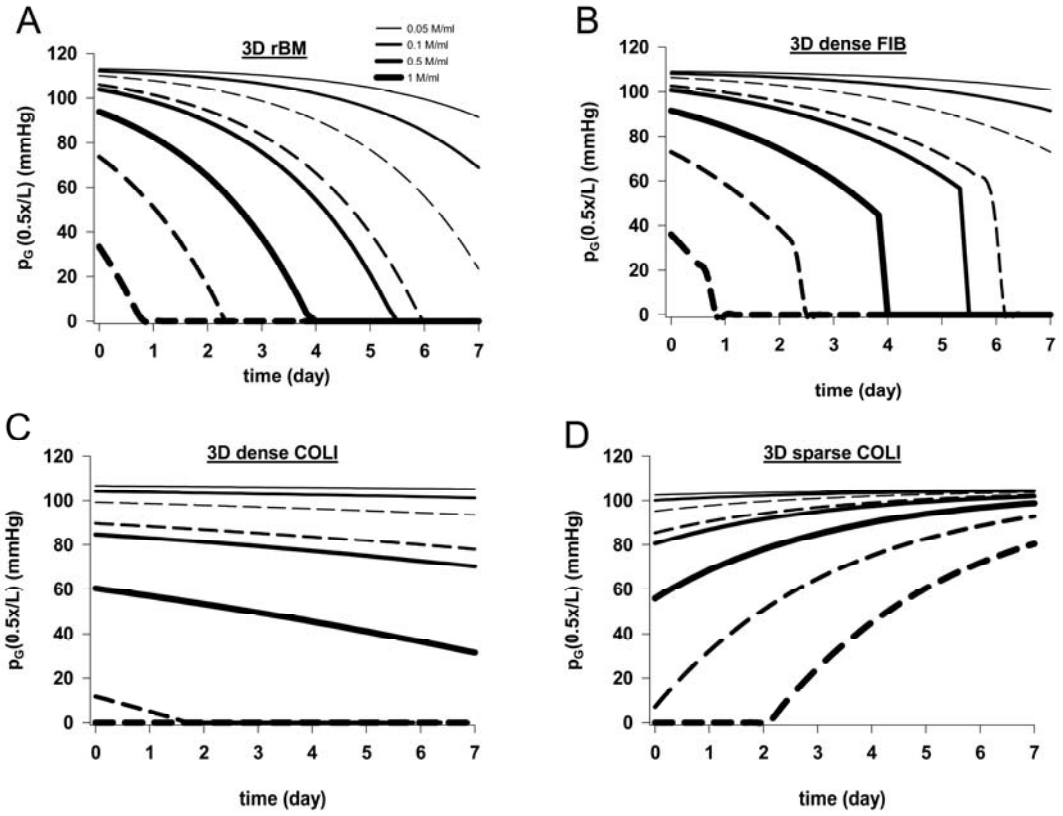

Fig 4.11. Predicted pressure values at the middle of a 2mm (continuous lines) or 4mm (dashed lines) thick gel in 3D cultures of A549 cells in rBM up to a week using the model described in Methods. Increasing line thicknesses corresponded to increasing seeding densities.

Also, the constraint of tuning $\rho_{o,max}$ for h_{max} permissive for either hypoxia (continuous line) or normoxia (dashed line) were assessed up to one week (Fig. 4.12). $\rho_{o,max}$ values from phenomenological recommendations given in the literature were taken (0.05 – 1 Mcell/ml, where M denotes 10^6 cells) [67, 77].

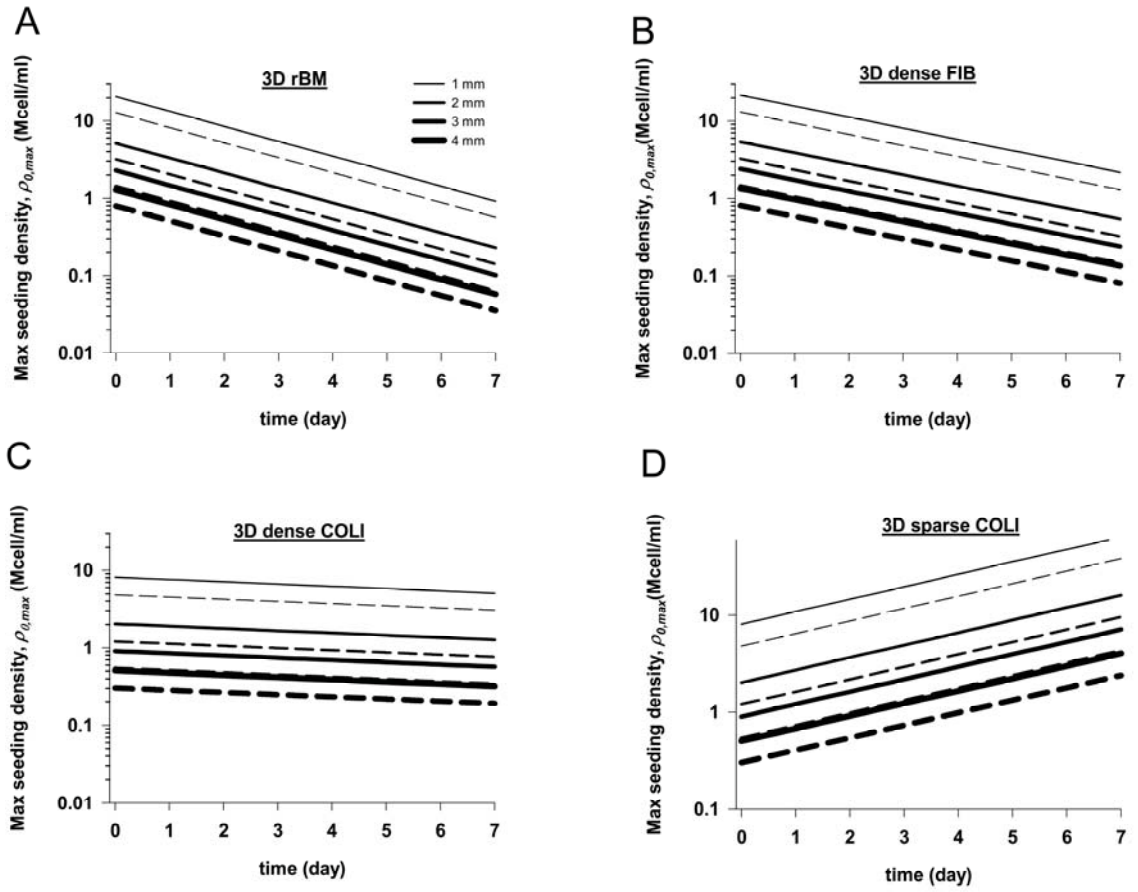

Fig 4.12. Predicted maximum seeding densities permissive for either normoxia (dashed lines) or hypoxia (continuous lines) in 3D cultures of A549 cells in rBM up to a week using the model described in Methods. Increasing line thicknesses corresponded to increasing gel thicknesses.

Likewise, the constraints of tuning h_{max} within 1-4 mm [41] for $\rho_{o,max}$ (Fig. 4.13) were assessed. The results in (Fig. 4.12) and (Fig.4.13) clearly illustrate the inverse relationship between h_{max} and $\rho_{o,max}$, and reveal a strong dependence with the day considered, since both h_{max} and $\rho_{o,max}$ decayed rapidly with time.

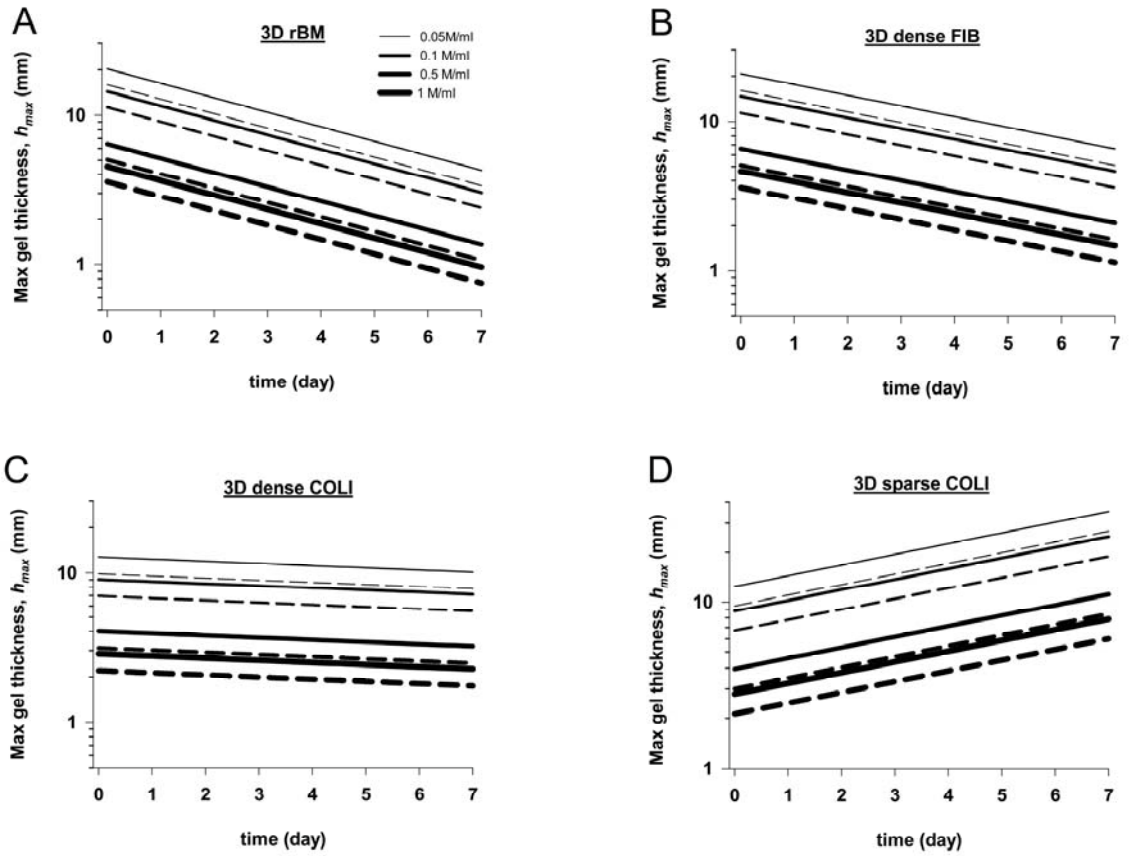

FIG 4.13. Predicted maximum gel thicknesses permissive for either normoxia (dashed lines) or hypoxia (continuous lines) in 3D cultures of A549 cells in rBM up to a week using the model described in Methods. Increasing line thicknesses corresponded to increasing seeding densities.

Therefore, the model used here predicted that normoxia arises in a narrow range of $\rho_{o,max}$ and h_{max} at all time points that decays markedly with time. In addition, it revealed that hypoxia arises in thicker gels, larger seeding densities or longer times. To illustrate how to use the predictions of the model as a starting point in the design of a 3D culture experiment, two common experimental scenarios were considered: ρ_o = 0.5 Mcell/ml or a 2 mm thick gel, and time-window of 1 week. In these conditions, the recommended h_{max} and $\rho_{o,max}$ permissive for hypoxia or normoxia in A549 cells in different gels are shown in Table II.

Table II. Predicted ranges for h_{max} and $\rho_{o,max}$ permissive for hypoxia/normoxia at half the gel thickness in A549 cells cultured in 3D up to 1 week .

ECM	*Max. height h_{max} (mm) (for ρ_o = 0.5 Mcell/ml)*		*Max. seeding density $\rho_{o,max}$ (Mcell/ml) (for h = 2 mm)*	
	Hypoxia	*Normoxia*	*Hypoxia*	*Normoxia*
rBM	≥ 1.35	1.06 – 1.35	≥ 0.22	0.14 – 0.22
dense COLI	≥ 3.2	2.46 – 3.2	≥ 1.27	0.76 – 1.27
dense FIB	≥ 2.08	1.6-2.08	≥ 0.54	0.14-0.54

5 Discussion

Chapter 5 Discussion

5.1Macromolecular Diffusion

5.1.1 Advantages of the experimental approach

Dextrans are flexible polymer chains that have been extensively used in transport studies in hydrogels and tissues and are known to diffuse as spherical particles in free solution according to Stokes-Einstein law [19, 21, 22, 28, 69]. A variety of experimental approaches have been reported to assess the diffusivity of FITC-dextrans and other fluorescently labeled particles in hydrogels and tissues, FRAP being among the most extensively used [19, 22, 45]. FRAP and most other microscopic approaches are based on confocal microscopy setups to assess the diffusivity of fluorescent particles within a micrometer-sized region of the sample. These microscopic approaches require expert personnel and expensive equipment, and often involve hydrogel manipulations that depart from those used in 3D cultures as in microfluidic-based diffusivity measurements [9]. Alternatively, it is conceivable that the fluorescence imaging capabilities of photometric devices available in most cell biology laboratories –such as spectrophotometers and MultiPlate Readers– could provide a cost-effective approach to monitor the slow fluorescent changes that occur during the diffusion of fluorescent particles in ECM gels in bulk. In support of this experimental possibility, few spectrophotometer-based diffusivity assays have been recently reported [78, 79]. In this study a proof-of-principle that Microplate Readers and Transwell plates can be used to assess macroscopic diffusivity in hydrogels has been provided. The macroscopic assay presented here was advantageous in that it did not require expert personnel, it involved minimum sample preparation and setup optimization, and enabled monitoring the diffusion of many samples in a multi-Transwell plate in parallel.

5.1.2 Modeling approaches

The macroscopic diffusion measurements were analyzed in terms of the semi-infinite gel model. This model has been previously shown to capture the critical physical aspects of diffusion problems similar to ours, and is overall advantageous in its computational simplicity. However it is limited in that it does not account for the finite gel thickness and the dextran flux to the lower Transwell compartment where the fluorescence measurements are made. Dealing with these theoretical limitations in full require finite element methods, whose computational complexity was beyond the scope of this work. Alternatively, a finite gel model has been developed that included the 3 layers through which dextrans diffused in the setup (i.e. dextran solution on top of the gel, gel and bottom Transwell compartment). Preliminary diffusivity data obtained with the finite model (D_{finite}) exhibited a strong correlation (R = 0.85) with that assessed with the semi-infinite model (D), and could be described by a linear relationship with a slope close to unity (D_{finite} = 1.16 D). A similar good agreement between semi-infinite and finite gel models has been recently reported in the diffusion of Dex10 through 5 mm thick COLI gels during the first 5 h [44], which is a time-window comparable to ours. These findings support that the diffusing dextran layer is generally smaller than the gel thickness for short times, thereby enabling the application of the semi-infinite model. Moreover, D_{finite} data were consistent with our major observation of a power-law relationship between D and M_r with the exponent predicted by the Stokes-Einstein law (α= 0.32 ± 0.03, r^2=0.99) thereby further supporting the physical interpretation of the results obtained with the semi-infinite model.

5.1.3 Comparison of the difusivity data with previously obtained values

Diffusivity data obtained on dense FIB were in good agreement with values reported elsewhere for Dex40 and Dex70, although they were at least 3-fold lower than those observed with low R_H particles like Dex4 and Dex10 [9, 43]. Likewise, our D data on both sparse and dense COLI were comparable to data reported for low R_H particles, although our values were ~2-fold higher than large R_H particles as Dex40 and Dex70 [22, 44]. Previous diffusivity data for dextrans in rBM gels have not been found. Instead, the diffusivity of gold nanoparticles in rBM was reported to be ~0.1×10^{-6} [80],

which is very close to our D values at the highest R_H (Fig. 4.3A). The discrepancies between our diffusivity data and that of others can be easily explained by the differences in the technical approach, gel preparation, animal source of the native ECM component and the transport properties of the specific tracer used. Despite all the latter sources of variability, it is remarkable the good agreement between our macroscopic D data and previously reported microscopic D values.

5.1.4 ECM viscosity dominates hindrance

Diffusion regulates the transport of molecules through the ECS in both tissues and 3D cultures [19, 68]. In addition to the geometrical obstacles posed by cells and the ECM scaffold, diffusion hindrance may arise from non-geometrical factors, although the relative contribution of geometric and non-geometric ECM characteristics remains ill defined. To address this question, we reduced confounding factors by examining the diffusivity of dextrans in acellular ECM gels. The size of dextrans was smaller than the average ECM pore size as revealed by AFM imaging (Fig. 4.5). The agreement between our w data on gels upon short-term fixation and previous studies on unfixed gels using alternative imaging approaches [70, 72, 73, 81, 82] support the validity of our imaging protocol. In these geometrical conditions, we provided direct evidence for the first time that the relationship between diffusivity and M_r obeyed the Stokes-Einstein law (Fig. 4.3A), thereby revealing that diffusion hindrance in ECM gels is dominated by non-geometrical viscous factors rather than geometrical (steric) properties. This observation was unexpected, since the Stokes-Einstein relation was derived to describe the diffusion of rigid spherical particles in free solution, which is in marked contrast with the complex entangled structure of ECM gels. Indeed, Stokes-Einstein law has been previously used to assess R_H of tracers in liquid [9, 22, 26, 28]. In qualitative agreement with our findings, previous attempts to examine D dependence on M_r reported power-law relationships in both FIB and COLI gels [9, 22], although they could not unambiguously discriminate the one-third power-law exponent from other possibilities. An important consequence of the validity of the Stokes-Einstein law was that it enabled assessing the effective ECS fluid viscosity, which turned out to be larger than that of water, yet within the same order of magnitude (Fig. 4.4A). ECS viscosity values fell within the physiological range, since they were comparable to either blood (for RBM

and dense FIB), lymph (for dense COLI) or plasma (for sparse COLI) according to previous studies [18]. Our theoretical calculations predicted a similar viscosity between rBM and dense FIB, which was confirmed by independently assessing gel viscosity by AFM (Fig. 4.4B). These results indicated that ECM gels can be modeled as a rigid porous material in terms of diffusion. Moreover, they revealed that ECS viscosity is the main physical property of the gel in controlling the tortuosity of spherical molecules that are smaller than the ECM pore size.

5.1.5 Physical basis of the increased viscosity: unattached macromolecules vs. wall-effects

The physical factors affecting diffusion hindrance in hydrogels are not nearly as well understood as those in free solution [83]. However, we can envision at least two potential effects underlying the enhanced ECS viscosity in ECM gels based on classical hydrodynamics: (i) a wall effect due to the surface of the ECM scaffold, and (ii) the effect of unassembled ECM macromolecules. Wall-effects describe the flow reduction in the proximity of a 2D wall, which increases the effective viscosity of the fluid [84]. This wall-effect predicts that diffusivity should correlate with pore size. However, such prediction was not consistent with the similar diffusivities observed in rBM and dense FIB. Likewise, it could not account for the similar tortuosities measured in the latter ECM gels and those reported in the ECS of brain tissue, which has a pore size of ~50 nm [19] that is much smaller than that of ECM gels (Fig 4.5E). The hydrodynamic effect of unassembled ECM macromolecules is grounded on the well known fluid viscosity increase in the presence of soluble macromolecules [85, 86]. For dilute solutions, this effect predicts that η increases linearly with the volume fraction Φ occupied by the large macromolecules. Although, to our knowledge, the fraction of unattached ECM molecules in an ECM gel remains unknown, we may assume that it is proportional to gel density d as a first approximation. In support of the latter prediction, we observed a linear relation between the normalized viscosity data (η/η_{water}) obtained in COLI and rBM gels and d (Fig. 4.4C). The simplest model that relates η/η_{water} and Φ for rod-like macromolecules like ECM filaments [72, 87] is the well-established Kuhn mode [85, 86], which predicts $\eta/\eta_{water} = 1 + (5/2 + x)\Phi$, where x is the axial ratio of the rod (x = length/width). Taking a previously suggested value of $x = 19$ [86] elicited Φ

~0.01 (sparse COLI), ~0.04 (dense COLI) and ~0.15 (rBM), which fell within the theoretical range of Φ data assessed in brain tissue (0.18-0.5) [23]. Likewise, the ratio between η/η_{water} and d elicited $\Phi \sim 0.11$ for dense FIB (Fig. 4.4). The role of unassembled ECM molecules in enhanced viscosity is further supported by previous observations reporting undistinguishable dextran diffusivities obtained in dense COLI solutions before and after gelation [22], or in aligned and nonaligned sparse COLI gels [88]. Based on all these results it is tempting to speculate that the enhanced ECS viscosity with gel density is largely due to the increased presence of unattached ECM macromolecules. Likewise, our data suggest that the similar diffusivities of rBM and dense FIB may be due to their comparable Φ.

5.1.6 Comparison between viscosity assays

The η values obtained from D data and Stokes-Einstein law were consistent qualitatively but not quantitatively with η_{AFM} values obtained by AFM (Fig. 4.4). Stokes-Einstein assumes that η corresponds to a Newtonian fluid, i.e. is f-independent in our experimental settings. In contrast, η_{AFM} values were markedly f-dependent, and were comparable to values obtained elsewhere by bulk rheometry measurements [89, 90]. Technical-dependent effects are likely involved in this discrepancy, since η_{AFM} was assessed by indenting the surface of the ECM gel with a micrometer-sized spherical tip, whereas η was calculated from the passive diffusion of nanometer-sized dextrans. In addition to technical effects, the large η_{AFM} values with respect to η revealed that they probed the mechanical response of different parts of the ECM gel. Thus, AFM measurements probed the dissipative forces developed as the whole gel was deformed by the AFM tip, which included the viscous response of both the insoluble filamentous network and the fluid filling the gel pores. The latter dissipative processes may include inter- and intra-fiber friction due to fiber realignment during AFM indentation. In contrast, the low η values obtained from diffusion measurements revealed that dextrans did not deform the ECM scaffold during diffusion, and that η values probed the friction between dextrans and the surrounding fluid, thereby supporting further that ECM gels can be modeled as rigid porous materials in terms of passive transport. Of note for the interpretation of diffusion hindrance in terms of non-geometric factors, both η_{AFM} and η

data consistently reported that the effective viscosity of dense FIB was closer to rBM than to dense COLI.

5.1.7 Tortuosity and suitable time windows in 3D cultures

Our macroscopic assay enabled estimating the relative contribution of cells and ECM gels in 3D cultures. Comparing our λ_{gel} values with the average $<\lambda_{cell}>$ reported elsewhere revealed a balance role of cell- and gel-dependent hindered diffusion in 3D cultures based on dense COLI gels in agreement with previous results [91], whereas λ_{cell} is expected to be dominant in sparse COLI. In contrast, our findings predicted that λ_{gel} is dominant over λ_{cell} in 3D cultures based in rBM and dense FIB. The dominant role of ECM in hindered diffusion is further supported when considering that λ_{gel} may be even higher for soluble signaling macromolecules, since many ECM components –including those used in this study– contain binding domains for different signaling molecules that may delay their diffusion through specific binding [18, 19]. Moreover, dextrans are known to exhibit increased diffusivity compared to more rigid spherical proteins like albumins or other proteins for the same M_r [28]. Nonetheless, we used λ_{gel} values and $<\lambda_{cell}>$ to assess λ_{3D} in a first approximation, and applied these data to estimate convenient experimental time-windows in 3D culture studies (Fig. 4.6). Our predicted t_{50} values were consistent with experimental time-windows previously reported in selected 3D culture experiments in rBM, FIB and COLI that are summarized in Table III [9, 40, 92, 93].

Gel	*Thickness*	*Signaling factor*	*predicted t_{50}*	*experimental time-window*[II]	*Reference*
rBM	na	Prolactin (22 kDa)	≥ 3 day[I]	3 day (β-casein expression)	[93]
rBM	~2 mm	TGF-α (17 kDa)	≥ 2.5 day[I]	2-3 day (robust branching)	[40]
dense COLI	na	HGF (~80 kDa)	≥ 2 day[I]	1 day (early branching)	[92]
dense FIB	na	na	~ 5 day[I]	7 day (robust branching)	[9]

Table III: Comparison between predicted t_{50} and experimental time-windows for selected 3D culture studies; [I]values based on a 2 mm gel thickness in Fig. 5; [II]t at which physiologic response was detected

On the other hand, comparing our λ_{gel} data with λ values reported in a variety of tissues indicated that rBM and dense FIB alone were able to mimic λ observed in extreme physiologic hindrance such as brain tissue and some tumors, whereas λ of dense COLI reproduced values reported in normal skin or granulation tissue. In contrast, sparse COLI could not reproduce any physiologic λ value even after adding the effect of λ_{cell}, indicating the limitations of this ECM model as a tissue surrogate in terms of diffusion. Collectively, our values support a major role of the ECM in hindered diffusion *in vivo*, particularly at densities > 3 mg/ml, and indicate that dense ECM gels are suitable tissue surrogates in terms of molecular transport.

5.2 Oxygen diffusion and consumption in 3D cultures

5.2.1 Oxygen diffusivity values in acellular ECM gels

A common approximation in oxygen transport studies is to consider that oxygen diffusivity within acellular hydrogels is comparable to that in aqueous medium [34, 35]. Our experimental data partially agreed with this approximation, since all our D_G values fell within the narrow range of ~1.7-2.5×10^{-5} cm^2/s, which was only up to 40% smaller than that of water (Fig. 4.7C) [35, 64]. The latter range was consistent with recent D_G measurements on fibrin gels reported elsewhere [35], thereby supporting our data analysis in acellular gels. The small decrease of D_G with respect to water has been traditionally attributed to the geometrical obstructions posed by the ECM scaffold [32, 64]. However, the small (< 1 nm) R_H of oxygen molecules compared to the large ($\gtrsim$ 1 μm) average pore size of our ECM gels [75] suggests that non-geometrical gel properties may account for the enhanced diffusion hindrance in ECM gels. In agreement with this hypothesis, we observed a marked correlation between our D_G data and that predicted by the Stokes-Einstein law considering the viscosity of the ECS fluid. Likewise, a decrease of oxygen concentration with viscosity was reported in synthetic liquids [94] and in eyes subjected to vitrectomy [95].

5.2.2 Technical approach: modeling assumptions

Previous studies have revealed that the essential aspects of diffusion and consumption in cellularized hydrogels can be estimated by applying reasonable approximations to the reaction-diffusion equation. This strategy (described in the Methods) was applied in this work, relying on three main assumptions. First, we considered quasi steady-state regimes based on the short time-scale of our measurements, which was supported by the plateaus observed in p measured in static conditions. Second, we assumed linearity of the Michaelis-Menten reactive term, which was equivalent to $p_G >> 0.45$ mmHg given our choice of K_m. Since the lowest p_G was ~ 10 mmHg, the linear approximation was well justified. Third, we assessed D_G^* assuming a 60% reduction in oxygen diffusivity with respect to that in acellular gels owing to the geometrical obstacles posed by cells, as reported in previous experimental and theoretical studies [19, 23]. This assumption elicited D_G^* ~1-1.5×10^{-5} cm^2/s, which is in agreement with previous values obtained in natural tissue extracts [64, 96] and some engineered tissues [65, 66], thereby supporting the suitability of this assumption.

5.2.3 Oxygen consumption quantification

Our theoretical approximations enabled assessing the oxygen consumption of A549 cells in 2D and 3D by calculating V_{max}. We found V_{max} values in 2D comparable to those reported in the same cell line elsewhere [97, 98] and, to different extents, lower than those observed in chondrocytes and hepatocytes [66, 99]. These findings illustrate that V_{max} is cell-type dependent, and provide further support to our data analysis in cellularized gels. Moreover, to our knowledge we obtained the first estimations of V_{max} values of A549 cells in 3D cultures. The larger V_{max} found in 3D with sparse COLI and in 2D compared to rBM has been previously attributed to the enhanced metabolic demand required to support the additional synthetic activity in 2D [100, 101]. Likewise, the similar V_{max} observed in 2D and COLI gels could be interpreted as a partial loss of epithelial differentiation in collagenous substrata with respect to rBM, in agreement with a previous study with epithelial cells [102]. On the other hand, our data suggested that sparse COLI induced a decrease in cell density in A549 cells. In support of this interpretation, an increase in cell death has been reported in low density COLI gels in a

variety of epithelial cell lines, and has been associated with the low compliance of these gels [103]. Collectively, our results expand the well-known ECM regulatory role of gene expression in the context of tissue-specific functions [3, 8].

5.2.4 Design considerations of 3D cultures and limitations

A major step in the design of a 3D culture experiment is the selection of ρ_o, the characteristics of the ECM gel (i.e. composition and density), the geometry of the gel container, and the experimental time-window. Currently available 3D culture protocols give recommendations on some of these variables based on phenomenological observations, whereas quantitative criteria are largely absent. Moreover, the selection of other variables remains rather arbitrary [67, 77]. To make a first step towards addressing these limitations, we assessed suitable ranges for four critical variables of 3D cultures in terms of oxygen tension: ECM density, gel thickness, ρ_o, and time-window. Thus, we first examined the effect of ECM density, and found that dense (≥ 3 mg/ml) gels are suitable tissue surrogates in terms of oxygen tension. Next, we adapted a simple mathematical model to set boundaries on h, ρ_o and time-window consistent with either normoxia or hypoxia. The critical parameter of the model was ϕ since, for a given cell type, the selection of the latter 3 variables (h, ρ_o and time) should match that ϕ value required for a specific oxygen tension. Illustrative values permissive for normoxia/hypoxia in common 3D culture experiments with A549 cells were given in Table III, and corresponded to $\phi \sim$ 19-24. Thus, our approach revealed that physiologic oxygen conditions arise in 3D cultures when $\phi > 1$, in contrast with tissue engineering studies that favor $\phi < 1$ to produce clinically valuable thick tissues [29, 35].

To examine the validity of our model, we compared its predictions with phenomenologic recommendations reported elsewhere. Lee and co-workers recommended 0.55 Mcell/ml for 3D cultures with malignant epithelial cells in rBM up to 10 days, and suggested gel volumes corresponding to $h \sim$ 1.2-2.8 mm depending on the gel container [77]. In the same conditions, our model predicted a normoxic range for $h_{max} \sim$ 1.06-1.35 mm, which support the lower range of the recommended h, but not the highest h value of 2.8 mm, since it may elicit hypoxia/anoxia. Chen and co-workers recommended 0.2 Mcell/ml for 3D cultures of endothelial cells in 2.5 mm thick dense FIB gels up to 3 days [67]. Applying values of the Michaelis-Menten parameters (V_{max},

K_m) in our model for endothelial cells [34] elicited h_{max} ~ 5.25-6.78 mm, thereby suggesting that the recommended conditions may be hyperoxic. These comparisons illustrate that our simple model could be extended to identify experimental conditions permissive for normoxia or hypoxia in other cell types, provided that their metabolic characteristics and growth rate can be assessed. For this purpose, a compilation of Michaelis-Menten parameters from different cell types can be found elsewhere [99].

The values recommended by our model should be taken as a starting point rather than as final values, since our model did not consider ECM remodeling, apoptosis or other biological processes that may affect the actual oxygen dynamics. Nonetheless, our model may be useful in short-cutting the time-consuming optimization period of 3D culture studies.

Considering how cell behavior in 3D cultures is regulated by a variety of diffusion related properties of the microenvironment, future work is needed to provide guidelines for optimizing some of these properties in 3D cultures. Accordingly, in the next section I will comment on the possible solutions related to the transport problem in the context of 3D gels used for cell culture.

5.3. Insight towards improving 3D cell cultures

Some of the limitations of native 3D cultures are unrelated to transport, but rather intrinsic to their biological nature. First, native ECM gels are in essence biomaterials derived from animals. Therefore, they tend to have minor percentage of impurities that may have biological activities [104]. In terms of cell culture, this means that experiments are not always 100% controlled and the outcome and reproducibility may depend on these unaccounted factors. In order to overcome this limitation, synthetic or biomimetic scaffolds have been developed, but these scaffolds, in turn have their own limitations such as lack of control over porosity and adhesion sites, and a higher price. Second, once cells are inside a 3D scaffold, the techniques to quantify certain aspects of the cells (ex. cell number), are far less available and straightforward than in the case of a 2D culture. A possible solution to this problem is degrading the matrix and recovering the cells, but such protocols are not standardized and might not work for all scaffold types. Third, 3D cultures are significantly more expensive to make and work with than traditional Petri dishes. Finally, there is certainly a need for standardization of the 3D cultures. Not only would standardization of culture conditions be beneficial for specific

experiments, but the communication of said experiments would be highly facilitated. This limitation could be overcome by quantifying the current unknowns and establishing a database of useful parameters for designing 3D cultures.

In terms of diffusion, the large λ_{gel} observed in ECM gels –particularly in rBM and dense FIB– has important experimental consequences that should be considered in the design and interpretation of 3D culture studies. First, there is a minimum time-window that must be contemplated to guarantee that all cells in a 3D culture are exposed to the same equilibrium concentration of the signaling molecule for a given ECM gel. Second, there is a risk of misinterpretation of 3D culture studies examining the biological effects of two or more exogenous signaling molecules with markedly distinct M_r owing to the D decay with M_r. Moreover, a large λ_{gel} induces sustained concentration gradients of signaling factors that may elicit asynchronous cellular stimulation according to the depth of the cell within the gel. A variety of bioreactors have been described mainly as a solution to controlling oxygen delivery to 3D cultures, most notably membrane based reactors, perfusion reactors and stirred-suspension-culture reactors [6]. A short-coming of these systems is that they are designed for creating large masses of tissue mainly for transplant, often not suitable for 3D cell cultures [3, 6, 8, 32]. Indeed, the optimized use of bioreactors in the field of 3D cultures would be a step forward towards improvement of culture conditions.

Nevertheless, most of the above mentioned unwanted diffusion effects can be overcome using simple experimental modifications. Thus, diffusion effects due to gel thickness can be minimized by using thinner gels according to (Fig. 4.6), and in agreement with previous studies on 0.1 mm thick COLI gels [41]. Thickness effects can be further reduced by preparing 3D cultures in Transwell inserts and adding the signaling factor both on top of the gel and in the bottom Transwell compartment. Alternatively, thickness effects may be completely prevented in many studies by culturing cells on top of the ECM gel instead of embedded [8, 105]. Regarding scaffold concentration, it is not advisable to use low density gels (<3mg/ml) . As seen in (Fig4.3B) and (Fig4.4A), sparse COLI scaffolds tend to not contribute much to the diffusion hindrance and have a viscosity that is close to that of water. On the other hand, misleading interpretations in studies involving two signaling molecules with different M_r can be reduced by adding first the molecule with larger M_r in the 3D culture according to (Fig. 4.6) or,

alternatively, by using the minimum t_{50} corresponding to the molecule with the largest M_r.

In addition to thickness and scaffold density effects, the initial cell seeding density is a very important variable, especially in experimental conditions that seek to quantify oxygen diffusion, consumption and pressure. This problem can be overcome by coupling the desired cell density with appropriate geometrical conditions and time windows in order to obtain the desired oxygen levels.

In addition to oxygen tension and diffusion properties of nutrients there are other factors that may influence the behavior of cells. These factors include, but are not limited to CO_2 concentration, matrix rigidity, the presence of matrix-binding factors in the culture medium. A careful assessment of these factors, coupled with the ones described in this work, may contribute to a better design of 3D cultures.

6 Conclusions

Chapter 6 Conclusions

6. 1 Diffusion of macromolecules

1.In this work a novel and simple macroscopic approach to measure diffusivity has been validated. The macroscopic diffusivity of dextran macromolecules with physiological M_r within a panel of ECM gels widely used in 3D cultures was measured. It has been observed that diffusivity decreased with M_r according to a power-law with the one-third exponent predicted by the Stokes-Einstein law.

2.The Stokes-Einstein relation derived for Newtonian fluids can be extended to the complex entangled structure of ECM gels for spherical particles much smaller than the average ECM pore size.

3.Hindered diffusion/tortuosity in ECM gels is dominated by non-geometrical hydrodynamic factors (i.e. ECS viscosity) rather than the geometrical (steric) properties of the gel.

4. Stokes-Einstein law predicted that rBM and dense FIB should exhibit comparable viscosities, which was confirmed by independent microrheology measurements by AFM. The enhanced ECS viscosity may arise from the hydrodynamic effects of unassembled ECM macromolecules within the ECS.

5. 3D cultures based on dense gels (≥ 3 mg/ml) are suitable tissue surrogates in terms of diffusion, and are even able to reproduce the extreme physiologic tortuosity of brain tissue.

6.These findings support that ECM is a major contributor to tissue tortuosity, particularly at large ECM densities, and the importance of using carriers with low R_H in drug delivery is highlighted.

7. The impact of ECM tortuosity in the design of 3D culture experiments was examined in terms of identifying optimal experimental time-windows and gel thicknesses for a given gel and M_r of the diffusing particle.

6. 2 Oxygen diffusion and consumption

1.New insights in the oxygen diffusion and consumption in 3D cultures with a panel of ECM gels have been provided. The analysis of oxygen diffusion in acellular gels strongly supported that diffusion hindrance is governed by the oxygen friction with the viscous ECS fluid, unlike previously thought.

2. The oxygen tension measurements in 3D cultures revealed that dense (≥ 3 mg/ml) gels are suitable tissue surrogates in terms of oxygen tension.

3.The first measurements of the OCR of A549 cells in 3D cultures have been provided, and a dominant effect of ECM composition over density in the OCR of these cells in dense gels has been revealed.

4. A simple mathematical model based on a single adimensional parameter (ϕ) to predict those values of h, ρ_o and time that may elicit physiological oxygen tension has been adapted. This model may be extended to other cell types provided that their Michaelis-Menten parameters and growth rate characteristics are known. The predictions of the model may be useful as starting points in 3D culture studies, thereby minimizing the initial optimization step.

Appendices

In this section I will detail some of the protocols and methodological approaches that served for carrying out the experiments (Appendix A) and models (Appendix B). Also, I am including a list of my publications and conference communications (Appendix C). The Matlab source code for finite modeling has been provided by Isabel Pastor and Francesc Mas.

Apendix A Gel preparation protocols

A.1 Collagen I gel preparation protocol

NOTE: Steps 1b, 4 and 5 only apply to experiments involving cells.

1a. Get ice. Store all tubes and reagents on ice.

1b. Warm up trypsin and media to be used for your cells (if it applies).

2. Neutralize COL I. Do all these steps on ice:

2a. Add 800 ul of COL I (stock) to the bottom of 50 ml tube. Collect ~810 ul to account for the COL I solution that will stick on the tip walls. Add 100 ul of DMEM 1X. Shake vigorously by hand. Wait a few seconds.

2b. Add 100 ul of 0.1M NaOH. Shake vigorously by hand. Wait few seconds. The solution must now look pinkish.

2c. Check that pH falls within physiologic range. Adjust pH if needed (not recommended).

3. Prepare target COL I concentration by diluting the neutralized COL I solution with the same culture media you use for your cells without serum!

4. Pre-coat the bottom of the culture vessel (well, dish, plate) by covering its surface with a thin layer of the COL I solution (prepared in step #3) by gently and slowly 'painting' the COL I solution on the surface with your tip. Incubate at 37C for 30 min.

5. Trypsinize the cells. Count your cell density. Collect the volume of cell suspension that contains the desired amount of cells for your experiments and transfer to a new tube. Centrifuge. Aspirate the media (be careful of not aspirating the cell pellet), and resuspend with the desired amount of COL I by pipetting up and down with a blue tip very slowly and gently to avoid introducing air bubbles. Keep tube on ice.

6. Add the desired amount of gel(+cells) solution to your pre-coated culture dish/well. Incubate at 37C for 30 min.

7. Add cell culture media to your gels. Use at least 2X the gel volume to calculate the amount of culture media.
8. When changing culture media, do not use vacuum to aspirate the media since you will detach the gel. Use a pipette tip instead!

GENERAL REMARKS

- Common sources of collagen I (COL I) are rat tail and bovine dermis. High quality COL I networks are more readily obtained from bovine dermis sources, so these are preferred to rat tail.
- COL I gellation is very sensitive to pH and to temperature, therefore these conditions must be controlled accurately and reproduced.
- Same protocol applies to matrigel, but without the neutralization step. Matrigel is the common option for endothelial and epithelial cells. Collagen I gel is the common option for mesenchymal cells or developmental experiments. Fibrin is another ECM that self/assembles forming stable gels and it is also used by many groups.
- Most other ECM components are not used on their own for 3D culture because they do not polymerize, but they can be mixed to either matrigel or COL I or fibrin while in solution.
- COL I must be prepared fresh for every experiment. Once prepared, it must be used within the next 2-3 h.
- Perform all steps on ice
- With each new lot of COLI, the right concentration of NaOH necessary to obtain a physiologic pH upon must be optimized.
- Consider treating your cells before plating with ascorbic acid, since it is required to deposit collagen by cells.
- Add ~30-40% extra COL volume to the volume needed for your experiment, since there is always some shrinking and COL I volume loss due to it stickiness to the tip walls.
- It may be useful to grow cells on 2D on the same experiment to compare the different morphologies and growth rates.

- Avoid serum in your preparation, since COL I has binding sites for many factors present in the serum that makes it difficult to wash out.
- Consider that COL I concentration below than 2 mg/ml implies a pore size bigger than the typical size of mammalian cells.
- Typical cell density is 0.5-1 10^6cells/ml of ECM solution, depending on your experiment and growing rates.
- Most mammalians cells are ok on ice for several minutes.
- Keep in mind that air concentration within the gel depends on its thickness. Therefore it is desirable to keep the thickness of your gel constant for all your experimental conditions.

A.2 Fibrin gel preparation protocol

NOTE: Thrombin is very delicate, it should be manipulated with little light and as fast as possible, Thrombin should be returned to the freezer immediately after its use.

1.Prepare the Fibrinogen+RPMI solution:

a.Determine the needed concentration. Weight the Fibrinogen, considering the clottable and protein fractions.

b.Dilute the Fibrinogen in the RPMI medium. In order to facilitate dilution, the solution may be placed at 37ºC for 5 minutes.

c.Filter the solution in a sterile chamber using a 0,2 micrometer pore filter.

2.Prepare the Thrombin solution:

Use Thrombin at 50U/ml, in a 1:50 proportion (Ex. You need 10µl Trombin for every 500µl of FGN solution).

If the thrombin concentration is 100U/ml it needs to be diluted to 50U/ml. Trombin and HEPES+RPMI may be mixed with the vortex.

3. Put the Thrombin, (Ex. 2.94µl for a 150 µl final volume) on the surface and on top of the Thrombin. Add the FGN+Medium solution (147µl for a 150 µl final volume). Blend the two very fast.

4.One everything is mixed spread it on the full surface.

5.Allow the mixture to stand for 5 minutes at room temperature.

6.Place inside the incubator for 25 minutes at 37ºC.

7.After the gelation, add cell culture media to your gels. Use at least 2X the gel volume.

GENERAL REMARKS :

- When you spread the solution on a Petri dish (or other substrate), it's important that you spread homogenously in the surface and you have to watch there aren't bubbles.
- The gels are stored inside the incubator and hydrated.

Appendix B Source codes

B.1 Matlab code for finite model fitting

```
%Diffusion Modelo Global

function y=DIFF(x,D0,Dg,l);

alpha=0.;

tol=1e-9;

y=invlap('difflap',x,alpha,tol,D0,Dg,l);

% INVLAP  numerical inverse Laplace transform

% f = invlap(F, t, alpha, tol, P1,P2,P3,P4,P5,P6,P7,P8,P9);

% F laplace-space function (string refering to an m-file), must have form F(s, P1,..,P9) ,
% where s is the Laplace parameter, and return column vector as result

% t       column vector of times for which real-space function values are sought

% alpha   largest pole of F (default zero)

% tol     numerical tolerance of approaching pole (default 1e-9)

% P1-P9   optional parameters to be passed on to F

% f       vector of real-space values f(t)

% example: identity function in Laplace space:

%   function F = identity(s);                  % save these two lines

%            F = 1./(s.^2);                    % ...  as "identity.m"

%   invlap('identity', [1;2;3])                % gives [1;2;3]

% algorithm: de Hoog et al's quotient difference method with accelerated

%   convergence for the continued fraction expansion

%   [de Hoog, F. R., Knight, J. H., and Stokes, A. N. (1982). An improved

%    method for numerical inversion of Laplace transforms. S.I.A.M. J. Sci.

%    and Stat. Comput., 3, 357-366.]
```

```
% Modification: The time vector is split in segments of equal magnitude
%   which are inverted individually. This gives a better overall accuracy.
%  details: de Hoog et al's algorithm f4 with modifications (T->2*T and
%    introduction of tol). Corrected error in formulation of z.
%  Copyright: Karl Hollenbeck
%            Department of Hydrodynamics and Water Resources
%            Technical University of Denmark, DK-2800 Lyngby
%            email: karl@isv16.isva.dtu.dk
%  22 Nov 1996, MATLAB 5 version 27 Jun 1997 updated 1 Oct 1998
%  IF YOU PUBLISH WORK BENEFITING FROM THIS M-FILE, PLEASE CITE
% IT AS:  Hollenbeck, K. J. (1998) INVLAP.M: A matlab function for numerical
%    inversion of Laplace transforms by the de Hoog algorithm,
%    http://www.isva.dtu.dk/staff/karl/invlap.htm
function f = invlap(F, t, alpha, tol, P1,P2,P3,P4,P5,P6,P7,P8,P9);
if nargin <= 2,
  alpha = 0;
elseif isempty(alpha),
  alpha = 0;
end
if nargin <= 3,
  tol = 1e-9;
elseif isempty(tol),
  tol = 1e-9;
end
f = [];
% split up t vector in pieces of same order of magnitude, invert one piece
%   at a time. simultaneous inversion for times covering several orders of
```

```
%   magnitudes gives inaccurate results for the small times.
allt = t;                           % save full times vector
logallt = log10(allt);
iminlogallt = floor(min(logallt));
imaxlogallt = ceil(max(logallt));
for ilogt = iminlogallt:imaxlogallt,    % loop through all pieces
   t = allt(find((logallt>=ilogt) & (logallt<(ilogt+1))));
 if ~isempty(t),                    % maybe no elements in that magnitude
   T = max(t)*2;
   gamma = alpha-log(tol)/(2*T);
   % NOTE: The correction alpha -> alpha-log(tol)/(2*T) is not in de Hoog's
   %   paper, but in Mathematica's Mathsource (NLapInv.m) implementation of
   %   inverse transforms
   nt = length(t);
   M = 20;
   run = [0:1:2*M]';    % so there are 2M+1 terms in Fourier series expansion
   % find F argument, call F with it, get 'a' coefficients in power series
   s = gamma + i*pi*run/T;
   command = ['a = ' F '(s'];
   if nargin > 4,                   % pass on parameters
     for iarg = 1:nargin-4,
           command = [command ',P' int2str(iarg)];
     end
   end
   command = [command ');'];
   eval(command);
   a(1) = a(1)/2;                   % zero term is halved
```

```
% build up e and q tables. superscript is now row index, subscript column
%   CAREFUL: paper uses null index, so all indeces are shifted by 1 here
e = zeros(2*M+1, M+1);
q = zeros(2*M  , M+1);              % column 0 (here: 1) does not exist
e(:,1) = zeros(2*M+1,1);
q(:,2) = a(2:2*M+1,1)./a(1:2*M,1);
for r = 2:M+1,                      % step through columns (called r...)
  e(1:2*(M-r+1)+1,r) = ...
        q(2:2*(M-r+1)+2,r) - q(1:2*(M-r+1)+1,r) + e(2:2*(M-r+1)+2,r-1);
  if r<M+1,                         % one column fewer for q
       rq = r+1;
       q(1:2*(M-rq+1)+2,rq) = ...
        q(2:2*(M-rq+1)+3,rq-1).*e(2:2*(M-rq+1)+3,rq-1)./e(1:2*(M-rq+1)+2,rq-1);
  end
end
% build up d vector (index shift: 1)
d = zeros(2*M+1,1);
d(1,1) = a(1,1);
d(2:2:2*M,1) = -q(1,2:M+1).'; % these 2 lines changed after niclas
d(3:2:2*M+1,1) = -e(1,2:M+1).'; % ...
% build up A and B vectors (index shift: 2)
%   - now make into matrices, one row for each time
A = zeros(2*M+2,nt);
B = zeros(2*M+2,nt);
A(2,:) = d(1,1)*ones(1,nt);
B(1:2,:) = ones(2,nt);
z = exp(i*pi*t'/T);             % row vector
```

```
   % after niclas back to the paper (not: z = exp(-i*pi*t/T)) !!!
   for n = 3:2*M+2,
     A(n,:) = A(n-1,:) + d(n-1,1)*ones(1,nt).*z.*A(n-2,:);  % different index
     B(n,:) = B(n-1,:) + d(n-1,1)*ones(1,nt).*z.*B(n-2,:);  %  shift for d!
   end
   % double acceleration
   h2M = .5 * ( ones(1,nt) + ( d(2*M,1)-d(2*M+1,1) )*ones(1,nt).*z );
   R2Mz = -h2M.*(ones(1,nt) - ...
          (ones(1,nt)+d(2*M+1,1)*ones(1,nt).*z/(h2M).^2).^.5);
   A(2*M+2,:) = A(2*M+1,:) + R2Mz .* A(2*M,:);
   B(2*M+2,:) = B(2*M+1,:) + R2Mz .* B(2*M,:);
   % inversion, vectorized for times, make result a column vector
   fpiece = ( 1/T * exp(gamma*t') .* real(A(2*M+2,:)./B(2*M+2,:)) )';
   f = [f; fpiece];                          % put pieces together
  end % if not empty time piece
  end % loop through time vector pieces
      % laplace diffusion
function F=difflap(s,D0,Dg,l);
q0=sqrt(s./D0);
qg=sqrt(s./Dg);
Dg0=sqrt(Dg./D0);
RD=((1+RD)./(1-RD)).*exp(2.*qg.*l);
F=(1./(qg.*s)).*(2.*exp(qg.*l))./((1-Dg0).*((RD-1)+(Dg0.*coth((0.6).*q0).*(1+RD))));
```

B.2 Mathematica code for simultaneous power law fitting

```
Clear[a1,a2,a3,a4,a5,a6,b,x,nlm];
Model1=a1*x^b;
Model2=a2*x^b;
Model3=a3*x^b;
Model4=a4*x^b;
Model5=a5*x^b;
Model6=a6*x^b;
 Data1(*Stokes*)={{4000,2.6*10^-10},{40000,7.6*10^-11},{70000,5.7*10^-11}};
Data2(*control*)={{4000,2.2*10^-10},{40000,1*10^-10},{70000,8*10^-11}};
Data3(*coll1mg*)={{4000,2*10^-10},{40000,9.1*10^-11},{70000,6.8*10^-11}};
Data4(*coll3mg*)={{4000,1.1*10^-10},{40000,6.2*10^-11},{70000,4.6*10^-11}};
Data5(*fibrin*)={{4000,5.3*10^-11},{40000,2.5*10^-11},{70000,1.8*10^-11}};
Data6(*matrigel*)={{4000,5.2*10^-11},{40000,2*10^-11},{70000,1.3*10^-11}};

CombinedModel:=Which[(*MDL==1,Evaluate@Model1,MDL==2,Evaluate@Model2,
*)MDL==3,Evaluate@Model3,MDL==4,Evaluate@Model4,MDL==5,Evaluate@Mod
el5,MDL==6,Evaluate@Model6,True,0];

CombiledData=Join[(*Insert[#,1,2]&/@Data1,Insert[#,2,2]&/@Data2,*)Insert[#,3,2]&/
@Data3,Insert[#,4,2]&/@Data4,Insert[#,5,2]&/@Data5,Insert[#,6,2]&/@Data6];
nlm=regreport=NonlinearModelFit[CombiledData,CombinedModel,{b,(*a1,a2,*)a3,a4,
a5,a6},{x,MDL}];
 normal=Normal[nlm];
 regreport[{"ParameterTable","RSquared"}];
 pointsplot=ListPlot[{Data3,Data4,Data5,Data6}];
 fit3=Plot[normal[[2]],{x,0,70000}];
fit4=Plot[normal[[4]],{x,0,70000}];
fit5=Plot[normal[[6]],{x,0,70000}];
fit6=Plot[normal[[8]],{x,0,70000}];
 Show[pointsplot,fit3,fit4,fit5,fit6];
```

B.3 Mathematica code for diffusion coefficient estimation

```
Manipulate[Show[Plot[n*C0*Erfc[x/(2*Sqrt[d*t2])],{t2,0,30000},Axes-
>{True,True},PlotRange->{{0,30000},{0,0.11}}],ListPlot[newdatapoints3,PlotStyle-
>PointSize[0.02]],ListPlot[newdatapoints4,PlotStyle-
>{PointSize[0.02],Red}],ListPlot[newdatapoints33,PlotStyle-
>{PointSize[0.02],Yellow}],ListPlot[newdatapoints5,PlotStyle-
>{PointSize[0.02],Black}],ListPlot[newdatapoints6,PlotStyle-
>{PointSize[0.02],Pink}],ImageSize->700],{x,0.002,0.002},{d,10^-12,10^-
8},{C0,0.1,1},{n,0.1,0.1}];
```

Appendix C Publications and conference communications

C.1 Publications

Roland Galgoczy, Isabel Pastor, Adai Colom, Raimon Sunyer, Alicia Giménez, Francesc Mas, Jordi Alcaraz, Diffusion hindrance in extracellular matrix gels used in 3D cultures is dominated by viscous effects according to Stokes-Einstein law ,Acta Biomaterialia (2nd revision, Impact factor: 5.093, Q1)

Adai Colom*, **Roland Galgoczy***, Isaac Almendros, Antonio Xaubet, Ramon Farre, Jordi Alcaraz, Oxygen diffusion and consumption in extracellular matrix gels: implications for designing 3D cultures, Journal of Biomedical Materials Research: Part A (Accepted for publication, Impact factor: 2.834, Q1) (* both authors contributed equally to this work)

Roland Galgoczy; Pere Roca-Cusachs; and Jordi Alcaraz (2013). Atomic Force Microscopy. In: eLS. John Wiley & Sons, Ltd: Chichester. DOI: 10.1002/9780470015902.a0002641.pub3. Chapter contribution to an online Encyclopedia.

Jordi Alcaraz, Hidetoshi Mori, Cyrus M. Ghajar, Doug Brownfield, **Roland Galgoczy** and Mina J. Bissell, Collective epithelial cell invasion overcomes mechanical barriers of collagenous extracellular matrix by a narrow tube-like geometry and MMP14-dependent local softening, : Integr. Biol., 2011,3, 1153–1166, DOI: 10.1039/c1ib00073j (Impact factor: 4.321, Q2).

C.2 Conference Communications

1. **Roland Galgoczy** , Isabel Pastor , Adai Colom , Alícia Giménez, Francesc Mas and Jordi Alcaraz. The XII Congress of SBE (Spanish Biophysical Society-Sociedad de Biofísica de España), Diffusion of particles with physiological molecular weights within extracellular matrix gels used in 3D cultures, Barcelona, Spain, 2012.

2. **Roland Galgoczy**, Adai Colom, Isaac Almendros, Alicia Gimenez, Daniel Navajas, Ramon Farre, Jordi ALcaraz. Extracellular matrix based 3D cultures as tissue surrogates in terms of O2 transport, 4th IBEC symposium on Bioengineering&Nanomedicine, Barcelona, Spain, October 2011.

3. Alicia Gimenez, Marta Puig, **Roland Galgcozy**, Antoni Xaubet, Noemi Reguart, Jordi Alcaraz. Role of anormal extracellular hardening in collagen turnover in lung fibrosis. Congreso de la Sociedad Espanola de Bioquimica Molecular, Barcelona, Spain, 2011.

4. **Roland Galgoczy**, Marta Puig, Roberto Lugo, Alicia Gimenez, Marta Gabasa, Antoni Xaubet, Daniel Navajas, Noemi Reguart, Jordi Alcaraz. Epithelial contribution to the myofibroblastic phenotype in non small lung cancer via epithelial to mesenchymal transformation. Conference of the International Association for the Study of Lung Cancer(IASLC), Amsterdam, July 2011.

5. Marta Puig, Alicia Gimenez, Abel Gomez-Caro, Roberto Lugo**, Roland Galgoczy**, Pere Gascon, Jordi Alcaraz, Noemi Reguart. Caveolin-1-independent fibroblast activation in squamous cell lung cancer(SCC). Conference of the International Association for the Study of Lung Cancer(IASLC), Amsterdam, July 2011.

List of abbreviations

3D	Three-dimensional
ECM	Extracellular matrix
GAG	Glycoaminoglycan
GF	Growth factor
rBM	Reconstituted basement membrane
EHS	Engelbreth-Holm-Swarm
S-E	Stokes-Einstein
OCR	Oxygen consumption rate
FRAP	Fluorescence recovery after photobleaching
FCS	Fluorescence correlation spectroscopy
EPR	Electron paramagnetic resonance
PET	Positron emission tomography
AFM	Atomic force microscopy
SFM	Serum free medium
COLI	Collagen type I
FIB	Fibrin
Dex4,40,70	Dextran at 4,40,70 kDa
ECS	Extracellular space

References

1. Harford, J.B., *Current Protocols in Cell Biology.* John Wiley & Sons, Inc., 2003.
2. Hynes, R.O., *Extracellular matrix: not just pretty fibrils.* Science, 2009. **326**(5957): p. 1216-19.
3. Frantz, C., Stewart KM, Weaver VM. , *The extracellular matrix at a glance.* Journal of Cell Science, 2010. **123**(4): p. 4195-4200.
4. Järveläinen, H., Sainio A, Koulu M, Wight TN, Penttinen R., *Extracellular matrix molecules: potential targets in pharmacotherapy.* Pharmacol Rev., 2009. **61**(2): p. 198-223.
5. Alberts, B., Johnson A., Lewis J., Raff M., Roberts K., and Walter P., *Molecular Biology of the Cell, 4th edition.* New York: Garland Science, 2002.
6. Griffith, L.G., Swartz MA. , *Capturing complex 3D tissue physiology in vitro.* Nat Rev Mol Cell Biol., 2006. **7**(3): p. 211-24.
7. Badylak, S., Freytes DO, Gilbert TW., *Extracellular matrix as a biological scaffold material: Structure and function.* Acta Biomater, 2009. **5**(1).
8. Alcaraz, J., Xu R, Mori H, Nelson CM, Mroue R, Spencer VA, Brownfield D, Radisky DC, Bustamante C, Bissell MJ. , *Laminin and biomimetic extracellular elasticity enhance functional differentiation in mammary epithelia. .* EMBO J 2008. **27**(21): p. 2829-38.
9. Ghajar, C.M., Chen X, Harris JW, Suresh V, Hughes CC, Jeon NL, Putnam AJ, George SC., *The effect of matrix density on the regulation of 3-D capillary morphogenesis.* Biophys J 2008. **94**(5): p. 1930-41.
10. Mori, H., Lo AT, Inman JL, Alcaraz J, Ghajar CM, Mott JD, Nelson CM, Chen CS, Zhang H, Bascom JL and others. , *Transmembrane/cytoplasmic, rather than catalytic, domains of Mmp14 signal to MAPK activation and mammary branching morphogenesis via binding to integrin beta 1.* Development, 2013. **140**(2): p. 343-352.
11. Alcaraz, J., Mori H, Ghajar CM, Brownfield D, Galgoczy R, Bissell MJ. , *Collective epithelial cell invasion overcomes mechanical barriers of collagenous extracellular matrix by a narrow tube-like geometry and MMP14-dependent local softening.* Integr Biol (Camb) 2011. **3**(12): p. 1153-66.
12. Friedl, P., Gilmour D., *Collective cell migration in morphogenesis, regeneration and cancer. .* Nat Rev Mol Cell Biol 2009. **10**(7): p. 445-57.
13. Helm, C.L., Fleury ME, Zisch AH, Boschetti F, Swartz MA., *Synergy between interstitial flow and VEGF directs capillary morphogenesis in vitro through a gradient amplification mechanism.* Proc Natl Acad Sci U S A., 2005. **102**(44): p. 15779-84.
14. Levental, K.R., Yu, H., Kass, L., Lakins, J. N., Egeblad, M., Erler, J. T., Fong, S. F., Csiszar, K., Giaccia, A., Weninger, W. et al., *Matrix crosslinking forces tumor progression by enhancing integrin signaling.* Cell, 2009. **139**(5): p. 891-906.
15. Provenzano, P.P., Eliceiri, K. W. and Keely, P. J. , *Shining new light on 3D cell motility and the metastatic process.* Trends Cell. Biol. , 2009. **19**(11): p. 638-648.

16. Acerbi, I., Luque T, Gimenez A, Puig M, Reguart N, Farre R, Navajas D, Alcaraz J. , *Integrin-specific mechanoresponses to compression and extension probed by cylindrical flat-ended AFM tips in lung cells.* . PLoS One 2012. **7**(2).
17. Nelson, C.M., Bissell MJ., *Of extracellular matrix, scaffolds, and signaling: tissue architecture regulates development, homeostasis, and cancer.* . Annu Rev Cell Dev Biol 2006. **22**: p. 287-309.
18. Swartz, M.A., Fleury ME. , *Interstitial flow and its effects in soft tissues.* . Annual Review of Biomedical Engineering, 2007. **9**.
19. Sykova, E., Nicholson C. , *Diffusion in brain extracellular space.* Physiological Reviews 2008. **88**(4): p. 1277-1340.
20. Zhou, S.H., Lo WC, Suhalim JL, Digman MA, Gratton E, Nie Q, Lander AD. Free *Extracellular Diffusion Creates the Dpp Morphogen Gradient of the Drosophila Wing Disc.* Curr. Biol. , 2012. **22**(8).
21. Netti, P.A., Berk DA, Swartz MA, Grodzinsky AJ, Jain RK. , *Role of extracellular matrix assembly in interstitial transport in solid tumors.* Cancer Res., 2000. **60**(9).
22. Ramanujan, S., Pluen A, McKee TD, Brown EB, Boucher Y, Jain RK., *Diffusion and convection in collagen gels: Implications for transport in the tumor interstitium.* . Biophys. J. , 2002. **83**(3).
23. Rusakov, D.A., Kullmann DM. , *Geometric and viscous components of the tortuosity of the extracellular space in the brain.* Proc Natl Acad Sci U S A. , 1998. **95**(15): p. 8975-8980.
24. Chauhan, V., Lanning RM, Diop-Frimpong B, Mok W, Brown EB, Padera TP, Boucher Y, Jain RK., *Multiscale Measurements Distinguish Cellular and Interstitial Hindrances to Diffusion In Vivo.* Biophys. J. , 2009. **97**(1).
25. Shkilnyy, A., Proulx P, Sharp J, Lepage M, Vermette P. , *Diffusion of rhodamine B and bovine serum albumin in fibrin gels seeded with primary endothelial cells.* . Colloid Surf. B-Biointerfaces, 2012. **93**.
26. Thorne, R.G., Hrabetova S, Nicholson C., *Diffusion of epidermal growth factor in rat brain extracellular space measured by integrative optical imaging.* Journal of Neurophysiology 2004. **92**(6).
27. Musnicki, W.J., Lloyd NW, Phillips RJ, Dungan SR. , *Diffusion of sodium dodecyl sulfate micelles in agarose gels.* J. Colloid Interface Sci. , 2011. **356**(1): p. 165.
28. Pluen, A., Netti PA, Jain RK, Berk DA. , *Diffusion of macromolecules in agarose gels: Comparison of linear and globular configurations.* Biophys. J. , 1999. **77**(1).
29. Bland, E., Dréau D, Burg KJL. , *Tissue oxygen monitoring in rodent models of shock* American Journal of Physiology-Heart and Circulatory Physiology, 2007. **293**(1): p. H526-H533.
30. Almendros, I., Farre R, Planas AM, Torres M, Bonsignore MR, Navajas D, Montserrat JM. , *Tissue Oxygenation in Brain, Muscle, and Fat in a Rat Model of Sleep Apnea: Differential Effect of Obstructive Apneas and Intermittent Hypoxia.* Sleep 2011. **34**(8): p. 1127-1133.
31. Dyson, A., Stidwill R, Taylor V, Singer M., *Tissue oxygen monitoring in rodent models of shock.* Am J Physiol, 2007. **293**: p. H526–H533.
32. Martin, Y., Vermette P. , *Bioreactors for tissue mass culture: Design, characterization, and recent advances.* Biomaterials 2005. **26**(35): p. 7481-7503.
33. Fischer Weiss, T., *Cellular Biophysics Transport.* The MIT Press, 1996.

34. Abaci, H.E., Truitt R, Tan S, Gerecht S. , *Unforeseen decreases in dissolved oxygen levels affect tube formation kinetics in collagen gels.* American Journal of Physiology-Cell Physiology 2011. **301**(2): p. C431-C440.
35. Ehsan, S.M., George SC. , *Nonsteady State Oxygen Transport in Engineered Tissue: Implications for Design.* Tissue Engineering Part A 2013. **19**(11-12): p. 1433-1442.
36. Reits, E.A.J., Neefjes J.J., *From fixed to FRAP: measuring protein mobility and activity in living cells.* NATURE CELL BIOLOGY, 2001. **3**.
37. Ahmad, R., Kuppusamy P., *Theory, instrumentation, and applications of electron paramagnetic resonance oximetry.* Chem Rev, 2010. **110**(5): p. 3212-36.
38. Galgoczy, R., Roca-Cusachs, P.,Alcaraz, J., *Atomic Force Microscopy.* eLS. John Wiley & Sons, Ltd: Chichester, 2013.
39. Rico, F., Alcaraz J., Fredberg J.J., Navajas D., *Nanomechanics of lung epithelial cells.* Int. J. Nanotechnology, 2005. **2**.
40. Fata, J., Mori H, Ewald AJ, Zhang H, Yao E, Werb Z, Bissell MJ. , *The MAPK(ERK-1,2) pathway integrates distinct and antagonistic signals from TGFalpha and FGF7 in morphogenesis of mouse mammary epithelium.* . Dev Biol 2007. **306**(1).
41. Raghavan, S., Shen CJ, Desai RA, Sniadecki NJ, Nelson CM, Chen CS. , *Decoupling diffusional from dimensional control of signaling in 3D culture reveals a role for myosin in tubulogenesis.* Journal of Cell Science 2010. **123**(17): p. 2877-2883.
42. Crank, J., *The mathematics of diffusion.* Oxford: Oxford University Press, 1975.
43. Moghe, P.V., Nelson RD, Tranquillo RT. , *Cytokine-stimulated chemotaxis of human neutrophils in a 3-d conjoined fibrin gel assay.* J. Immunol. Methods 1995. **180**(2).
44. Vasaturo, A., Caserta S, Russo I, Preziosi V, Ciacci C, Guido S., *A Novel Chemotaxis Assay in 3-D Collagen Gels by Time-Lapse Microscopy.* PLoS One 2012. **7**(12).
45. Braeckmans, K., Peeters L, Sanders NN, De Smedt SC, Demeester J. , *Three-dimensional fluorescence recovery after photobleaching with the confocal scanning laser microscope.* Biophys. J., 2003. **85**(4).
46. Blonk, J., Don A, Van Aalst H, Birmingham JJ. , *Fluorescence photobleaching recovery in the confocal scanning light-microscope.* J. Microsc.-Oxf. , 1993. **169**.
47. Meyvis, T., De Smedt SC, Van Oostveldt P, Demeester J., *Fluorescence recovery after photobleaching: A versatile tool for mobility and interaction measurements in pharmaceutical research.* Pharm. Res. , 1999. **16**(8).
48. Sprague, B.L., Pego RL, Stavreva DA, McNally JG., *Analysis of binding reactions by fluorescence recovery after photobleaching.* Biophys. J. , 2004. **86**(6).
49. Mazza, D., Braeckmans K, Cella F, Testa I, Vercauteren D, Demeester J, De Smedt SS, Diaspro A, *A new FRAP/FRAPa method for three-dimensional diffusion measurements based on multiphoton excitation microscopy.* Biophys. J. , 2008. **95**(7).
50. Pastor, I., Vilaseca E, Madurga S, Garces JL, Cascante M, Mas F., *Diffusion of alpha-Chymotrypsin in Solution-Crowded Media. A Fluorescence Recovery after Photobleaching Study.* J. Phys. Chem. B 2010. **114**(11).

51. Rico, F., Roca-Cusachs P, Sunyer R, Farre R, Navajas D. , *Cell dynamic adhesion and elastic properties probed with cylindrical atomic force microscopy cantilever tips.* J Mol Recognit., 2007. **20**(6).
52. Alcaraz, J., Buscemi L, Grabulosa M, Trepat X, Fabry B, Farre R, Navajas D. , *Microrheology of human lung epithelial cells measured by atomic force microscopy.* . Biophys J., 2003. **84**(3).
53. Sunyer, R., Trepat X, Fredberg JJ, Farre R, Navajas D. , *The temperature dependence of cell mechanics measured by atomic force microscopy.* Phys Biol., 2009. **6**(2).
54. Gehler, S., Baldassarre M, Lad Y, Leight JL, Wozniak MA, Riching KM, Eliceiri KW, Weaver VM, Calderwood DA, Keely PJ., *Gehler S, Baldassarre M, Lad Y, Leight JL, Wozniak MA, Riching KM, Eliceiri KW, Weaver VM, Calderwood DA, Keely PJ.* Mol Biol Cell., 2009. **20**(14).
55. Alcaraz, J., Buscemi L, Puig-de-Morales M, Colchero J, Baró A, Navajas D. , *Correction of microrheological measurements of soft samples with atomic force microscopy for the hydrodynamic drag on the cantilever.* Langmuir, 2002. **18**(3).
56. Waigh, T.A., *Microrheology of complex fluids.* . Rep. Prog. Phys., 2005. **68**(3).
57. Sneddon, I.N., *The relaxation between load and penetration in the axisymmetric Boussinesq problem for a punch of arbitrary profile.* Acta Biomater. , 1965. **5**(1).
58. Kiernan, J.A., *Formaldehyde, formalin, paraformaldehyde and glutaraldehyde: What they are and what they do.* . Microscopy Today 2000. **1**(5).
59. Sheu, M.T., Huang JC, Yeh GC, Ho HO. , *Characterization of collagen gel solutions and collagen matrices for cell culture.* Biomaterials, 2001. **22**(13).
60. Horcas, I., Fernández R, Gómez-Rodríguez JM, Colchero J, Gómez-Herrero J, Baro AM, *WSXM: A software for scanning probe microscopy and a tool for nanotechnology.* . Review of Scientific Instruments 2007. **78**(8).
61. Abramoff, M., Magelhaes PJ, Ram SJ., *Image processing with ImageJ.* Biophotonics Int 2004. **11**(36).
62. Zhao, F., Pathi P, Grayson W, Xing Q, Locke BR, Ma T. , *Effects of oxygen transport on 3-D human mesenchymal stem cell metabolic activity in perfusion and static cultures: Experiments and mathematical model.* Biotechnology Progress 2005. **21**(4): p. 1269-1280.
63. Christoforides, C., Laasberg LH, Hedley wh.J., *Effect of temperature on solubility of O2 in human plasma.* J Appl Physiol, 1969. **26**: p. 56-60.
64. Demol, J., Lambrechts D, Geris L, Schrooten J, Van Oosterwyck H, *Towards a quantitative understanding of oxygen tension and cell density evolution in fibrin hydrogels.* . Biomaterials 2011. **32**(1): p. 107-118.
65. Glicklis, R., Merchuk JC, Cohen S. , *Modeling mass transfer in hepatocyte spheroids via cell viability, spheroid size, and hepatocellular functions.* Biotechnology and Bioengineering 2004. **86**(6): p. 672-680.
66. Patzer, J.F., *Oxygen consumption in a hollow fiber bioartificial liver-revisited.* . Artificial Organs 2004. **28**(1): p. 83-98.
67. Chen, Z.J., Htay A, Dos Santos W, Gillies GT, Fillmore HL, Sholley MM, Broaddus WC. , *In vitro angiogenesis by human umbilical vein endothelial cells (HUVEC) induced by three-dimensional co-culture with glioblastoma cells.* Journal of Neuro-Oncology 2009. **92**(2): p. 121-128.

68. Thorne, R.G., Lakkaraju A, Rodriguez-Boulan E, Nicholson C. , *In vivo diffusion of lactoferrin in brain extracellular space is regulated by interactions with heparan sulfate.* Proc Natl Acad Sci U S A., 2008. **105**(24).
69. Pluen, A., Boucher Y, Ramanujan S, McKee TD, Gohongi T, di Tomaso E, Brown EB, Izumi Y, Campbell RB, Berk DA, Jain RK., *Role of tumor-host interactions in interstitial diffusion of macromolecules: Cranial vs. subcutaneous tumors.* . Proc Natl Acad Sci U S A., 2001. **98**(8).
70. Mickel, W., Munster S, Jawerth LM, Vader DA, Weitz DA, Sheppard AP, Mecke K, Fabry B, Schroder-Turk GE, *Robust pore size analysis of filamentous networks from three-dimensional confocal microscopy.* Biophys J, 2008. **95**(12).
71. Miroshnikova, Y.A., Jorgens DM, Spirio L, Auer M, Sarang-Sieminski AL, Weaver VM. , *Engineering strategies to recapitulate epithelial morphogenesis within synthetic three-dimensional extracellular matrix with tunable mechanical properties.* . Phys Biol. , 2011. **8**(2).
72. Raeber, G.P., Lutolf MP, Hubbell JA. , *Molecularly engineered PEG hydrogels: a novel model system for proteolytically mediated cell migration.* Biophys J., 2005. **89**(2).
73. Yang, Y.L., Leone LM, Kaufman LJ., *Elastic moduli of collagen gels can be predicted from two-dimensional confocal microscopy.* Biophys J., 2009. **97**(7).
74. Yang, Y.L., Motte S, Kaufman LJ., *Pore size variable type I collagen gels and their interaction with glioma cells.* Biomaterials, 2010. **31**(21).
75. Galgoczy, R., Pastor I, Colom A, Sunyer R, Giménez A, Mas F, Alcaraz J. , *Diffusion hindrance in extracellular matrix gels used in 3D cultures is dominated by viscous effects according to Stokes-Einstein law.* Acta Biomater (in revision), 2013.
76. Kowalczk, I., Read J, Salomon M, *Li-air batteries: A classic example of limitations owing to solubilities.* Pure and Applied Chemistry 2007. **79**(5): p. 851-860.
77. Lee, G.Y., Kenny PA, Lee EH, Bissell MJ. , *Three-dimensional culture models of normal and malignant breast epithelial cells.* . Nat Methods 2007. **4**(4): p. 359-65.
78. Srikantha, N., Mourad F, Suhling K, Elsaid N, Levitt J, Chung PH, Somavarapu S, Jackson TL., *Influence of molecular shape, conformability, net surface charge, and tissue interaction on transscleral macromolecular diffusion.* . Exp Eye Res., 2012. **102**.
79. Wang, S., Tarbell JM. , *Effect of fluid flow on smooth muscle cells in a 3-dimensional collagen gel model.* Arterioscler Thromb Vasc Biol., 2000. **20**(10).
80. Kim, B., Han G, Toley BJ, Kim CK, Rotello VM, Forbes NS. , *Tuning payload delivery in tumour cylindroids using gold nanoparticles.* Nat Nanotechnol., 2010. **5**(6).
81. Pedersen, J.A., Swartz MA. , *Mechanobiology in the third dimension.* . Ann Biomed Eng., 2005. **33**(11).
82. Zaman, M.H., Trapani LM, Siemeski A, Mackellar D, Gong H, Kamm RD, Wells A, Lauffenburger DA, Matsudaira P., *Migration of tumor cells in 3D matrices is governed by matrix stiffness along with cell-matrix adhesion and proteolysis.* Proc Natl Acad Sci U S A. , 2006. **103**(29).
83. Buck, K., Dungan SR, Phillips RJ., *The effect of solute concentration on hindered gradient diffusion in polymeric gels.* Journal of Fluid Mechanics 1999. **396**.

84. Happel, J., Brenner H., *Low Reynolds number hydrodynamics: with special applications to particulate media.* Dordretch, The Netherlands, 1991. **1**.
85. Huggins, M.L., *The viscosity of dilute solutions of long-chain molecules.* . J. Phys. Chem. B, 1938. **42**(7).
86. Matheson, R.R., *Viscosity of solutions of rigid rodlike macromolecules.* Macromolecules, 1980. **13**(3).
87. Zhao, H.G., Ma L, Zhou J, Mao ZW, Gao CY, Shen JC. , *Fabrication and physical and biological properties of fibrin gel derived from human plasma.* . Biomed Mater., 2008. **3**(1).
88. Erikson, A., Andersen HN, Naess SN, Sikorski P, Davies CD. , *Physical and chemical modifications of collagen gels: Impact on diffusion.* Biopolymers, 2008. **89**(2).
89. Forgacs, G., Newman SA, Hinner B, Maier CW, Sackmann E., *Assembly of collagen matrices as a phase transition revealed by structural and rheologic studies.* . Biophys J., 2003. **84**(2).
90. Gobeaux, F., Belamie E, Mosser G, Davidson P, Asnacios S. , *Power law rheology and strain-induced yielding in acidic solutions of type I-collagen.* . Soft Matter, 2010. **6**.
91. Magzoub, M., Jin S, Verkman AS. , *Enhanced macromolecule diffusion deep in tumors after enzymatic digestion of extracellular matrix collagen and its associated proteoglycan decorin.* FASEB J., 2008. **22**(1).
92. Nelson, C.M., Vanduijn MM, Inman JL, Fletcher DA, Bissell MJ., *Tissue geometry determines sites of mammary branching morphogenesis in organotypic cultures.* Science, 2006. **314**(5797).
93. Roskelley, C.D., Desprez PY, Bissell MJ. , *Extracellular matrix-dependent tissue-specific gene expression in mammary epithelial cells requires both physical and biochemical signal transduction.* Proc Natl Acad Sci U S A., 1994. **91**(26).
94. Gabriel, J.L., Miller TF, Wolfson MR, Shaffer TH. , *Quantitative structure-activity relationships of perfluorinated hetero-hydrocarbons as potential respiratory media - Application to oxygen solubility, partition coefficient, viscosity, vapor pressure, and density.* ASAIO Journal 1996. **42**(6): p. 968-973.
95. Stefansson, E., Loftsson T. , *The Stokes-Einstein equation and the physiological effects of vitreous surgery.* Acta Ophthalmologica Scandinavica 2006. **84**(6): p. 718-719.
96. Cheema, U., Rong Z, Kirresh O, MacRobert AJ, Vadgama P, Brown RA., *Oxygen diffusion through collagen scaffolds at defined densities: implications for cell survival in tissue models.* Journal of Tissue Engineering and Regenerative Medicine 2012. **6**(1): p. 77-84.
97. Molter, T.W., McQuaide SC, Suchorolski MT, Strovas TJ, Burgess LW, Meldrum DR, Lidstrom ME., *A microwell array device capable of measuring single-cell oxygen consumption rates.* Sensors and Actuators B-Chemical 2009. **135**(2): p. 678-686.
98. Wu, M., Neilson A, Swift AL, Moran R, Tamagnine J, Parslow D, Armistead S, Lemire K, Orrell J, Teich J and others, *Multiparameter metabolic analysis reveals a close link between attenuated mitochondrial bioenergetic function and enhanced glycolysis dependency in human tumor cells.* American Journal of Physiology-Cell Physiology 2007. **292**(1): p. C125-C136.
99. Croll, T.I., Gentz S, Mueller K, Davidson M, O'Connor AJ, Stevens GW, Cooper-White JJ. , *Modelling oxygen diffusion and cell growth in a porous,*

vascularising scaffold for soft tissue engineering applications. Chemical Engineering Science 2005. **60**(17): p. 4924-4934.
100. Guaccio, A., Borselli C, Oliviero O, Netti PA. , *Oxygen consumption of chondrocytes in agarose and collagen gels: A comparative analysis* Biomaterials 2008. **29**(10): p. 1484-1493.
101. Le Beyec, J., Xu R, Lee SY, Nelson CM, Rizki A, Alcaraz J, Bissell MJ. , *Cell shape regulates global histone acetylation in human mammary epithelial cells.* Exp Cell Res 2007. **313**(4): p. 3066-75.
102. Gudjonsson, T., Ronnov-Jessen L, Villadsen R, Rank F, Bissell MJ, Petersen OW. , *Normal and tumor-derived myoepithelial cells differ in their ability to interact with luminal breast epithelial cells for polarity and basement membrane deposition.* J Cell Sci 2002. **115**(Pt 1): p. 39-50.
103. Wang, Y.H., Chiu WT, Wang YK, Wu CC, Chen TL, Teng CF, Chang WT, Chang HC, Tang MJ., *Deregulation of AP-1 proteins in collagen gel-induced epithelial cell apoptosis mediated by low substratum rigidity.* Journal of Biological Chemistry 2007. **282**(1): p. 752-763.
104. Zhang, S., *Beyond the Petri dish.* NATURE BIOTECHNOLOGY, 2004. **22**(2): p. 151-152.
105. Streuli, C.H., Schmidhauser C, Bailey N, Yurchenco P, Skubitz AP, Roskelley C, Bissell MJ., *Laminin mediates tissue-specific gene expression in mammary epithelia.* J Cell Biol. , 1995. **129**(3).